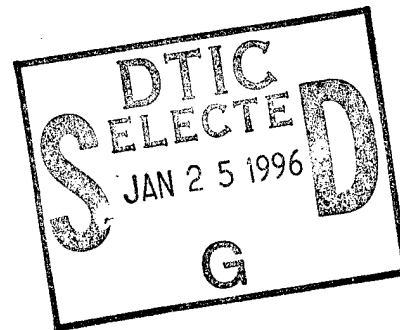


NAVAL POSTGRADUATE SCHOOL MONTEREY, CALIFORNIA



THESIS



GLOBAL EVALUATION OF
SPECIAL SENSOR MICROWAVE/IMAGER
OCEAN SURFACE WIND SPEED RETRIEVAL
ALGORITHMS FOR THE PERIOD
SEPTEMBER 1991-APRIL 1992

by

William A. Hesser
June, 1995

Thesis Advisor:
Co-Advisor:

R.C.Olsen
M.C. Colton

19960118019

Approved for public release; distribution is unlimited.

DTIC QUALITY INSPECTED 3

REPORT DOCUMENTATION PAGE

Form Approved OMB No. 0704-0188

Public reporting burden for this collection of information is estimated to average 1 hour per response, including the time for reviewing instruction, searching existing data sources, gathering and maintaining the data needed, and completing and reviewing the collection of information. Send comments regarding this burden estimate or any other aspect of this collection of information, including suggestions for reducing this burden, to Washington Headquarters Services, Directorate for Information Operations and Reports, 1215 Jefferson Davis Highway, Suite 1204, Arlington, VA 22202-4302, and to the Office of Management and Budget, Paperwork Reduction Project (0704-0188) Washington DC 20503.

1. AGENCY USE ONLY <i>(Leave blank)</i>	2. REPORT DATE	3. REPORT TYPE AND DATES COVERED	
	June 1995	Master's Thesis	
4. TITLE AND SUBTITLE GLOBAL EVALUATION OF SPECIAL SENSOR MICROWAVE/IMAGER OCEAN SURFACE WIND SPEED RETRIEVAL ALGORITHMS FOR THE PERIOD SEPTMEBER 1991-APRIL1992		5. FUNDING NUMBERS	
6. AUTHOR William A. Hesser			
7. PERFORMING ORGANIZATION NAME(S) AND ADDRESS(ES) Naval Postgraduate School Monterey CA 93943-5000		8. PERFORMING ORGANIZATION REPORT NUMBER	
9. SPONSORING/MONITORING AGENCY NAME(S) AND ADDRESS(ES)		10. SPONSORING/MONITORING AGENCY REPORT NUMBER	
11. SUPPLEMENTARY NOTES The views expressed in this thesis are those of the author and do not reflect the official policy or position of the Department of Defense or the U.S. Government.			
12a. DISTRIBUTION/AVAILABILITY STATEMENT Approved for public release; distribution is unlimited.		12b. DISTRIBUTION CODE	
13. ABSTRACT <i>(maximum 200 words)</i>			
<p>The Fleet Numerical Meteorology and Oceanography Center (FNMOC) has the charter to provide Special Sensor Microwave/Imager (SSMI) data to the DOD and the NOAA. This has led FNMOC to examine new methods for processing SSM/I data to generate SSM/I products. Of particular interest is the ability to use the SSM/I to remotely sense ocean surface winds.</p> <p>For this study four candidate wind retrieval algorithms initially proposed at the SSM/I Algorithm Symposium held in June, 1993 are examined for potential implementation at FNMOC. Previous calibration/validation studies of the efficacy of wind speed algorithms focused on regional (mid-latitude or tropical) data sets prompting the requirement to develop a more encompassing, global data set on which to evaluate the proposed algorithms.</p> <p>Comparisons of SSM/I wind retrieval methods reveal that the current FNMOC operational algorithm overestimates wind speeds when atmospheric water vapor content exceeds 50 kg/m². Adjustments made to this algorithm effectively mitigate the high wind speed bias, but at the cost of eliminating a significant amount of data. Neural network algorithms display high wind speed bias for winds above 11 m/s and low wind speed bias for winds below 4 m/s. The performance of neural network algorithms is largely independent of atmospheric moisture content. A new, global training data set is necessary to enable neural network algorithms to perform properly over the full range of global wind speeds. The use of brightness temperature-based rain flags are recommended for use in all wind speed retrieval methods.</p>			
14. SUBJECT TERMS SSMI Remote Sensing of Ocean Surface Winds		15. NUMBER OF PAGES 110	
		16. PRICE CODE	
17. SECURITY CLASSIFICATION OF REPORT Unclassified	18. SECURITY CLASSIFICATION OF THIS PAGE Unclassified	19. SECURITY CLASSIFICATION OF ABSTRACT Unclassified	20. LIMITATION OF ABSTRACT UL

NSN 7540-01-280-5500

Standard Form 298 (Rev. 2-89)
Prescribed by ANSI Std. Z39-18 298-102

Approved for public release; distribution is unlimited.

**GLOBAL EVALUATION OF SPECIAL SENSOR MICROWAVE/IMAGER
OCEAN SURFACE WIND SPEED RETRIEVAL ALGORITHMS FOR
THE PERIOD SEPTEMBER 1991-APRIL 1992**

William A. Hesser
Lieutenant, United States Navy
B.S., Texas A&M University, 1987

Submitted in partial fulfillment
of the requirements for the degree of

MASTER OF SCIENCE IN APPLIED PHYSICS

from the

NAVAL POSTGRADUATE SCHOOL

June 1995

Author:

William A. Hesser

William A. Hesser

Approved by:

Richard Christopher Olsen

R.C. Olsen, Thesis Advisor

Marie C. Colton

M.C. Colton, Co-Advisor

W. B. Colson

W.B. Colson, Chairman
Department of Physics

Accesion For	
NTIS	CRA&I
DTIC	TAB
Unannounced	
Justification	
By _____	
Distribution / _____	
Availability Codes	
Dist	Avail and / or Special
A-1	

ABSTRACT

The Fleet Numerical Meteorology and Oceanography Center (FNMOC) has the charter to provide Special Sensor Microwave/Imager (SSMI) data to the DOD and the NOAA. This has led FNMOC to examine new methods for processing SSM/I data to generate SSM/I products. Of particular interest is the ability to use the SSM/I to remotely sense ocean surface winds.

For this study four candidate wind retrieval algorithms initially proposed at the SSM/I Algorithm Symposium held in June, 1993 are examined for potential implementation at FNMOC. Previous calibration/validation studies of the efficacy of wind speed algorithms focused on regional (mid-latitude or tropical) data sets prompting the requirement to develop a more encompassing, global data set on which to evaluate the proposed algorithms.

Comparisons of SSM/I wind retrieval methods reveal that the current FNMOC operational algorithm overestimates wind speeds when atmospheric water vapor content exceeds 50 kg/m^2 . Adjustments made to this algorithm effectively mitigate the high wind speed bias, but at the cost of eliminating a significant amount of data. Neural network algorithms display high wind speed bias for winds above 11 m/s and low wind speed bias for winds below 4 m/s. The performance of neural network algorithms is largely independent of atmospheric moisture content. A new, global training data set is necessary to enable neural network algorithms to perform

properly over the full range of global wind speeds. The use of brightness temperature-based rain flags are recommended for use in all wind speed retrieval methods.

TABLE OF CONTENTS

I. INTRODUCTION	1
II. BACKGROUND	5
A. THEORY	5
1. Sources of Thermal Radiation	5
2. Ocean Surface Microwave Emission	7
3. Atmospheric Transmission	10
a. Precipitation Effects	10
b. Water Vapor	12
B. OCEAN BUOYS	12
1. National Data Buoy Center (NDBC)	12
2. Tropical Ocean-Global Atmosphere (TOGA)	14
C. SPECIAL SENSOR MICROWAVE/IMAGER (SSM/I)	16
1. Instrument Description	16
2. Radiometer Calibration	17
D. MULTIPLE REGRESSION WIND SPEED RETRIEVAL ALGORITHMS ..	18
1. D-Matrix Algorithm	18
2. Calibration/Validation (CV) Algorithm	20
3. Improved Goodberlet, Swift and Wilkerson (GSW) Algorithm	22
E. ARTIFICIAL NEURAL NETWORK WIND RETRIEVAL METHODS ..	23
1. The Stogryn, Butler, Bartolac (SBB) Neural Network	25
2. The Krasnopolksy, Breaker, Gemmill (NMC) Neural Network	26
III. STUDY PROCEDURES	29
A. BUOY DATA SET	29
B. SSM/I - BUOY MATCHUP CRITERIA	30
C. WIND SPEED DISTRIBUTION	31
IV. OBSERVATIONS	33
A. SSM/I WIND SPEED VS IN-SITU BUOY WIND SPEED	33
1. All SSM/I-Buoy Matchups	33
2. Nearest Neighbor, Average or Weighted Average SSM/I Data	34
B. BRIGHTNESS TEMPERATURE-BASED DATA PARTITIONING	37

C. PHYSICAL PARAMETER-BASED DATA PARTITIONING	38
V. ANALYSIS	41
A. CV ALGORITHM	41
B. GSW ALGORITHM	41
C. SBB AND NMC NEURAL NETWORKS	42
VI. CONCLUSIONS AND RECOMMENDATIONS	43
APPENDIX A: FIGURES	45
APPENDIX B: TABLES	93
LIST OF REFERENCES	99
INITIAL DISTRIBUTION LIST	101

I. INTRODUCTION

Microwaves, a generic term that includes centimeter, millimeter, and submillimeter wavelength regions of the electromagnetic spectrum, play an important role in the remote sensing of the Earth's atmosphere. Microwaves penetrate clouds, for example, and are therefore able to provide an all-weather measurement capability. Additionally, microwaves provide a direct means for the determination of cloud water content. Early aircraft and satellite flights showed that passive microwave radiometers could be used to detect microwave energy emitted by the Earth's oceans, and that these emissions could, in turn, be used to develop algorithms to retrieve ocean surface wind speeds.

Microwave radiometry of Earth from satellites began with the 1968 launch of Cosmos-243 and the 1970 launch of Cosmos-384. These Soviet satellites contained a nadir-viewing instrument having four channels with frequencies between 3.5 and 37 GHz, and provided determinations of water vapor and cloud liquid water over the oceans in addition to surface parameters. The first U.S. microwave imagers to evaluate the dynamics of the ocean surface from space were the electrically scanning microwave radiometer (ESMR) systems aboard NIMBUS-5 (1972) and NIMBUS-6 (1975) satellites (Janssen, 1993).

In 1978, the first scanning multichannel microwave radiometers (SMMR) were carried aboard the SEASAT-A and NIMBUS-7 satellites. The SMMR contained five channels with dual polarization at frequencies from 6.6 to 37 GHz, and provided the first multi wavelength observations in the atmospheric "window" regions of the microwave spectrum. Sea-surface temperatures and wind speed were obtained from the 6.6 and 10.7 GHz measurements. Despite some limitations, the SMMR clearly demonstrated the capability to remotely sense near-surface ocean wind speeds (Janssen, 1993).

Following the SMMR, a Special Sensor Microwave/Imager (SSM/I) was built by Hughes Aircraft Company (HAC) under the direction of the Naval Space Systems Activity (NSSA) and the Air Force Space Division as part of the Defense Meteorological Satellite Program (DMSP). The SSM/I represents a joint Navy/Air Force operational program to

obtain synoptic maps of critical atmospheric, oceanographic, and selected land parameters on a global scale, including the measurement of local and large scale variability of ocean surface wind speeds for ridge, front, and storm weather systems (Hollinger et al., 1987). The SSM/I has a higher frequency range for microwave energy detection than the SMMR and twice the swath width. The first SSM/I was launched in June of 1987 aboard DMSP spacecraft F8. Identical SSM/I instruments have subsequently been launched aboard DMSP spacecrafcts F10 (1990), F11 (1992), F12 (1994) and F13 (1995).

The earliest SSM/I wind speed retrieval algorithm was developed by Environmental Research and Technology, Inc (ERT) for Hughes and is termed the D-matrix algorithm. This multi-channel linear regression algorithm employs nine distinct climate codes segmented according to season and latitude band. Because microwave radiation at SSM/I frequencies is susceptible to attenuation by rain, which masks the wind speed signature generated by waves and foam on the ocean surface, ERT suggested the use of a "rain flag" for the purpose of identifying conditions under which less accurate wind speed retrievals are produced (Lo, 1983 and Hollinger et al., 1987).

Not long after the launch of the first spacecraft with an SSM/I instrument aboard, DMSP undertook to calibrate and validate the SSM/I wind speed retrieval algorithm developed by ERT. Validation of the D-matrix algorithm was done using the anemometer measured winds of open ocean buoys maintained by the National Oceanic and Atmospheric Administration (NOAA). The results of the D-matrix algorithm validation indicated that it possessed a high wind speed bias and exhibited significant discontinuity across climate code boundaries (Hollinger et al., 1991). To correct these problems, new coefficients for the D-matrix algorithm were developed, in 1989, by Goodberlet et al., to bring the wind speed retrieval accuracy to within the DOD specified requirement of ± 2 m/s under rain free conditions. The Goodberlet algorithm is the algorithm currently employed at the Fleet Numerical Meteorological and Oceanography Center (FNMOC). Subsequent modifications to the Goodberlet algorithm were completed by Goodberlet, Swift and Wilkerson in 1992.

In addition to traditional regression-based algorithms, attempts have been made to

retrieve wind speeds from SSM/I data using artificial intelligence - specifically, neural networks. The use of neural networks to perform wind speed retrieval was first demonstrated by Dawson and Fung (1993). The first neural network developed specifically for use with SSM/I data was constructed by Stogryn et al. (1994) and showed a 30% increase in wind speed retrieval accuracy in non-precipitating conditions. More recently, a single "all-weather" neural network was developed by Krasnopolksy et al. (1994), that achieved similar accuracies.

The regression algorithms and neural networks used to retrieve ocean wind speeds from SSM/I data have all been developed and tested using the same SSM/I - NOAA buoy pair data base used to validate the original D-matrix algorithm. These data consist of brightness temperatures from spacecraft F8 during the period 10 July 1987 through 31 March 1988, and in-situ measurements from NOAA buoys that lie predominately in the mid-latitude ocean region. The lack of algorithm validation against buoys in equatorial regions, where lower wind speeds and higher atmospheric moisture dominate, was recognized at the SSM/I Algorithm Symposium held in June 1993, as was the need for an expanded data set that would encompass regions varied enough for the SSM/I - NOAA buoy pair data set to be considered truly global.

To address the need for validation of wind speed retrieval algorithms in the lower wind speed, high moisture regions, Sayward (1994) examined data from equatorial TOGA buoys for the three month period Sep-Dec 1991. This initial work revealed problems at low wind speeds, indicating a need for further study. The goals of this study, then, are to:

- a) compile an expanded data set of SSM/I - NOAA buoy pairs in mid-latitude regions.
- b) compile an expanded data set of SSM/I - NOAA buoy pairs in equatorial regions.
- c) combine the individual mid-latitudinal and equatorial SSM/I- NOAA buoy pair data sets into a single global data set.
- d) evaluate the performance of the following wind retrieval methods over a global data set:
 - Calibration Validation algorithm (CV)

- Goodberlet, Swift, Wilkerson improved algorithm (GSW)
- Stogryn, Butler, Bartolac Neural Network (SBB)
- Krasnopolksy, Breaker, Gemmill Neural Network (NMC)

The following chapter gives an overview of the physics of microwave radiometry, provides background information on the NOAA buoys used in this study, introduces the reader to neural networks, describes in detail the four competing wind retrieval methods algorithms, and provides a detailed description of the SSM/I instrument. Chapter III describes the method used to obtain SSM/I - NOAA buoy pairs for study, and the methods used to compare the different wind retrieval methods. Chapter IV discusses the results of the wind speed retrieval comparisons. Chapter V analyzes the results. Finally, Chapter VI presents conclusions and recommendations. Figures and tables illustrating the comparison results are contained in Appendix A and B respectively.

II. BACKGROUND

A. THEORY

1. Sources of Thermal Radiation

All objects in the physical universe which are not at absolute zero temperature radiate energy in the form of electromagnetic waves. Some of that energy is transported as energy in the microwave region (4-100 GHz). To understand how and why passive microwave radiometers are used to remotely sense the ocean surface, it is necessary to first understand radiative transfer theory. Radiative transfer theory describes the intensity of radiation propagating in a general class of media, of which the ocean is a constituent, that absorb, emit, and scatter radiation. In the theory, the intensity or "brightness", which is a flow of energy across a unit area, per unit frequency for a blackbody medium, follows from Planck's law, which describes the wavelength and temperature dependence of radiation emitted from a blackbody (Janssen, 1993):

$$(1) \quad B_v(T) = \frac{2hv^3}{c^2} \frac{1}{e^{hv/kT} - 1} .$$

B = radiance

k = Boltzmann's Constant

v = frequency

h = Planck's constant

c = speed of light

T = temperature

In the case of microwaves, however, $hv \ll kT$. This is known as the *Rayleigh-Jeans limit* and allows equation (1) to be approximated as:

$$(2) \quad B_v(T) \approx \frac{2v^2kT}{c^2} .$$

The significant feature of the Rayleigh-Jeans limit is the linear relationship of the Planck

function with physical temperature. In the case of the ocean, which is an only moderately reflective surface, its thermal emission is reduced by its emissivity ϵ_s , which is a function of incidence angle, sea surface temperature, and salinity. For an isothermal surface viewed at an angle θ , the emitted radiation, T_e , depends only on the product of the temperature T_s and the emissivity ϵ_s of the surface:

$$(3) \quad T_e = \epsilon_s T_s$$

Inserting equation (3) into equation (2) gives the ocean radiance, L :

$$(4) \quad L_v(T) \approx \frac{2v^2k}{c^2} [\epsilon_s T_s] .$$

L = ocean radiance

k = Boltzman's Constant

v = frequency

c = speed of light

ϵ_s = ocean surface emissivity

T_s = surface temperature

The thermal radiation spectrum received by a passive microwave radiometer is comprised of three primary components: 1) surface emitted and reflected radiation, 2) upwelling atmospheric radiation, 3) reflected downwelling atmospheric radiation (Figure 1). If θ is the local zenith angle on Earth viewed by the satellite instrument and the Z-direction is normal to the Earth's surface, then the equivalent blackbody temperature of this radiation may be expressed (Grody, 1993):

$$(5) \quad T_B(v, \theta) = T_u(v, \theta) + T_e(v, \theta)e^{-\tau_{\text{geo}}\theta} + T_r(v, \theta)e^{-\tau_{\text{geo}}\theta}$$

where:

T_B = total brightness temperature

T_u = upwelling atmospheric radiation

T_e = surface emitted and reflected radiation

T_r = reflected downwelling radiation

$e^{-\tau}$ = transmittance function.

The quantity (τ) is the atmospheric opacity or the relative capacity of atmospheric constituents (oxygen, water vapor, clouds, or rain) to obstruct the transmission of radiant energy. At microwave frequencies away from absorption maxima, and under most atmospheric conditions except moderate to heavy rainfall, the opacity is small. The reflected and emitted radiation from the surface are difficult to treat analytically because of multiple scattering due to surface roughness and inhomogeneities within the material.

2. Ocean Surface Microwave Emission

For inferring wind speed at the ocean surface, the surface emissivity, ϵ , is the single most important parameter. Winds act on the ocean surface to generate surface waves which increase in amplitude with increasing wind speed. As the waves grow, roughness elements associated with these waves also increase. Eventually, the waves begin to break forming whitecaps and foam which tend to scatter the emitted surface radiation. Foam, which is a combination of air and water, has a lower reflectivity than pure water and, therefore, a higher emissivity. (Krasnopolksy et al., 1994)

To determine the amount of microwave emission from the ocean surface, relationships may be developed based upon the knowledge that microwaves seldom exceed penetration skin depths of greater than 1 cm. For this reason, the ocean may be assumed to be semi-infinite, homogeneous, and isothermal. Since all transmitted energy is eventually absorbed in a semi-infinite, homogeneous conducting medium, absorption can be defined as:

$$(6) \quad A = 1 - R$$

A = absorption of microwave energy

R = reflectivity of ocean surface

If one further assumes the ocean surface is at thermal equilibrium, then the rate of emission from the surface is equal to the rate of absorption at the surface and equation (6) may be written:

$$(7) \quad R = 1 - \epsilon$$

where ϵ is the emissivity from the ocean surface.

For a calm sea surface, microwave emissions as a function of incidence angle are highly polarized. At the SSM/I viewing angle of 53 degrees, for example, the emissivity for vertical polarization is nearly twice that of horizontal polarization (Figure 2). This large polarization difference is exploited to distinguish ocean surfaces from other surfaces or atmospheric particles where scattering of the microwaves reduce polarization differences. Over smooth water surfaces the reflectivity is calculated from the Fresnel coefficients for a plane dielectric interface:

$$(8a) \quad r_v = \left[\left| \frac{\epsilon_w \cos \theta - \sqrt{\epsilon_w - \sin^2 \theta}}{\epsilon_w \cos \theta + \sqrt{\epsilon_w - \sin^2 \theta}} \right| \right]^2$$

$$(8b) \quad r_h = \left[\left| \frac{\epsilon_w \cos \theta - \sqrt{\epsilon_w - \sin^2 \theta}}{\epsilon_w \cos \theta + \sqrt{\epsilon_w - \sin^2 \theta}} \right| \right]^2$$

where:

r_v = vertical polarization

r_h = horizontal polarization

ϵ_w = complex relative dielectric constant.

A commonly used linear approximation to ocean surface reflectivity is

$$(9) \quad r_\beta = 0.638 - 0.00272v$$

where v is frequency in GHz. Owing to the difficulties of characterizing the shape of wind roughened surfaces and the complexity of electromagnetic interactions with any reasonably realistic representation of the wave shape, models that rely on empirical corrections based on experimentally derived relationships between brightness temperature and wind speed have been developed.

Three mechanisms affect emissivity from a rough ocean surface. The first of these

results from surface waves having long wavelengths compared to microwaves. These surface waves change the local incident angle and mix the horizontal and vertical polarization states (Wentz, 1992). A second roughness mechanism is the diffraction of microwaves by surface waves that are small compared to radiation wavelength, called Bragg diffraction. The third mechanism is due to foam from breaking waves.

The individual contributions of these three mechanisms to total brightness temperature varies with incidence angle of the radiometer and the ocean's physical condition at the surface. At low incidence angles (<20 deg), specular reflections from long ocean waves of comparable slope dominate. From 20-60 deg Bragg roughness effects dominate ocean surface emissions. As foam forms on the ocean higher brightness temperatures are generated. Because foam consists of a mixture of air and water, the average dielectric constant of foam is much less than the value of water. Since the dielectric is lower the reflectivity is also lower, therefore, the brightness temperature is higher (Swift, 1990). If there is no foam on the surface only the brightness temperature of the water is measured - normally around 110 K; but if the ocean surface is 100% foam covered, then the true water temperature is measured - at temperatures around 290 K. Thus, there is a substantial swing in brightness temperatures. Since the percent foam coverage increases with surface wind speed, this difference in brightness temperature may be used to determine ocean wind speed.

Ocean foam, which is normally present for wind speeds ω (measured at 20 m above the ocean surface) greater than ~ 7 m/s, is modeled as a perfect blackbody ($\epsilon = 1$), and with a frequency-dependent effective fractional surface coverage, f_s (Gasiewski, 1993):

$$(10) \quad f_s = \begin{cases} 0.006 (1 - e^{-v/v_0}) (\omega - 7); & \omega \geq 7 \text{ m/s} \\ 0 & \omega < 7 \text{ m/s} \end{cases}$$

where $v_0 = 7.5$ GHz. Due to the impact of wind-induced foam and surface roughness, the emissivity of the ocean increases from 0.50 to 0.55 for winds ranging from calm to 20 m/s. A similar increase in emissivity results from a decrease in sea-surface temperature, so that

the total emissivity variation is ± 0.05 about an average value of 0.55 (Grody, 1993).

Horizontally polarized brightness temperatures for rough and foam covered ocean surface display an increase over smooth surface values, regardless of radiometer viewing angle (Hollinger, 1971). Vertically polarized brightness temperatures do not vary monotonically with angle. For rough ocean surfaces viewed at angles less than 50 deg, vertical polarization temperature increases with roughness. At viewing angles greater than 50 deg vertical polarization temperature values decrease for rough ocean surfaces. It is because of this phenomenon that space radiometers view the ocean surface at approximately 50 deg. This viewing angle serves to minimize surface roughness effects and increase sensitivity in brightness temperature to foam generation. No fewer than four oceanographic studies confirm that the percentage of foam increases with increased wind speed, and hence there is a relationship between wind speed over the ocean and the brightness temperature received by a passive radiometer (Figure 3).

3. Atmospheric Transmission

Energy that is radiated and reflected by the ocean through the atmosphere, is subjected to attenuation and absorption by atmospheric constituents. Indeed, absorption of microwaves by atmospheric constituents provides the physical connection into the atmosphere that is exploited for remotely sensing its properties. In attempting to measure brightness temperatures for use in wind-speed retrieval algorithms, water vapor and liquid water, both in the form of cloud water and rain, play important roles. High levels of atmospheric moisture tend to affect the accuracy of brightness temperature levels received at the radiometer resulting in inaccurate wind speeds. The magnitude of these processes depends upon wavelength, drop size distribution and precipitation layer thickness.

a. Precipitation Effects

Rain, when present, is the primary source of atmospheric attenuation when viewing the ocean surface from space at frequencies less than 50 GHz (Grody, 1993). The attenuation results from both absorption and scattering by hydrometeors (Hollinger, 1987). Hydrometeors can be classified into a few distinct categories (Gasiewski, 1993):

1. Small liquid droplets of radius less than $\sim 50 \mu\text{m}$, typical of nonprecipitating cumulus and stratus clouds, fog, and haze.
2. Oblately shaped, liquid precipitation, of radius between $50 \mu\text{m}$ and $\sim 5 \text{ mm}$.
3. Frozen particles of radius less than $\sim 1 \text{ mm}$.
4. Frozen particles of radius between 1mm and $\sim 10 \text{ mm}$.

Liquid hydrometeors of radius less than $\sim 50 \mu\text{m}$ absorb microwave radiation appreciably but scatter very little. Under this condition, the attenuation is independent of droplet size as long as the total mass of water droplets in a given volume remains the same. The radiative transfer of microwave energy through small cloud droplets can, therefore, be analyzed in the same manner as through a hydrometeor-free atmosphere where only absorption and emission occur.

For larger liquid hydrometeors (e.g. rain) or most frozen hydrometeors (e.g. snow, hail, and cirrus ice), the droplets are large enough so that microwave scattering can be significant, particularly at high frequencies (Gasiewski, 1993). Over oceans, the variations in emissivity due to wind-generated roughness and foam are small compared to the changes in transmittance due to water vapor and liquid water. Therefore, the liquid water content of clouds and rain can be obtained from dual frequency measurements, where a second channel must be used to account for the water vapor contribution.

Contrasts between rain and its surroundings allow for discrimination between rain and nonraining clouds simply from increases in brightness temperature. Warmer, more emissive precipitating regions over sea surfaces possess brightness temperatures that are 50 K greater than clear areas. Absorption due to oxygen is relatively small so that absorption depends primarily on vertically integrated liquid water Q due to rain and cloud droplets, and integrated water vapor V . The opacity through the atmosphere can be approximated as:

$$(11) \quad \tau \approx - (V/V_v + Q/Q_v)$$

where the coefficients V_v and Q_v depend on the frequency and can be determined using atmospheric models. The liquid water parameter also depends on cloud temperature and

drop size.

b. Water Vapor

The complex vibrational-rotational absorption spectrum of water vapor, together with relatively large concentrations of water vapor in the lower atmosphere, account for the dominance of this gas in the spectrum extending from the near infrared spectral region beyond the far infrared into the microwave region. The water vapor molecule has an electric dipole moment which causes resonance absorption peaks in the microwave region at 22.235 GHz and 183 GHz. The amount of absorption depends on the number of molecules present (the humidity). An increase in water vapor can result in an increase of up to 100 °K in brightness temperature at 22 GHz on humid days (Swift, 1990).

B. OCEAN BUOYS

1. National Data Buoy Center (NDBC)

During the 1960's, about 50 individual buoy programs were conducted by a variety of ocean-oriented agencies. In March 1966, the Ocean Engineering Panel of the Interagency Committee on Oceanography recommended that the United States Coast Guard (USCG) investigate the feasibility of a consolidated national data buoy system. As a result of that investigation, the National Council for Marine Research Resources and Engineering Development endorsed the formation of the National Data Buoy Development Program (NDBDP) in 1967. The NDBDP was created and was placed under the control of the USCG.

In 1970, the National Oceanic and Atmospheric Administration (NOAA) was formed and the NOAA Data Buoy Office (NDBO) was created. In 1982, the NDBO was renamed the National Data Buoy Center (NDBC) and was placed under the NOAA's National Weather Service (NWS).

The first buoys deployed by NDBC were large 12-meter discus hulls constructed of steel. These were generally deployed in deep water off of the U.S. East Coast and in the Gulf of Mexico. The measurements taken by sensors aboard these buoys include barometric pressure, temperature, and wind speed and direction. By 1979, sixteen stations were

deployed in the Pacific, seven in the Atlantic, and three in the Gulf of Mexico. Eight more stations were deployed in the Great Lakes after 1979. In addition to 12-meter buoys, 3 and 10 meter buoys have also been designed (Figure 4). As of February, 1995, 70 NDBC moored buoys were in operation.

Moored buoys are deployed in the coastal waters from the western Atlantic to the Pacific Ocean around Hawaii, and from the Bering Sea to the South Pacific. NDBC's moored buoys measure and transmit barometric pressure; wind direction, speed, and gust; air and sea temperature; and wave energy spectra from which significant wave height, dominant wave period, and average wave period are derived.

Meteorological sensors aboard moored buoys are normally located at the ten meter level for the 10 meter and 12 meter buoys. However, barometers are located inside the hull at the water level. Sea surface temperature sensors are located at a depth of one meter. To conserve power, sensors installed on moored buoys generally do not continuously measure and record data. Rather, for most NDBC buoys, an eight minute period is used for data collection by on-board sensors. Prior to 1993, the observation time was simply the nearest hour. Beginning in August, 1993, the official observation time was moved to coincide with end-of-data-acquisition time. Sensors are calibrated prior to deployment and are replaced with recently calibrated instruments after two years of operation.

The payload carried aboard NDBC varies. The term "payload" refers to the electronic system used to acquire the data, format it into a message, and then transmit the message to the satellite. The payloads are as follows: GSBP -- General Service Buoy Payload; DACT -- Data Acquisition Control and Telemetry; VEEP -- Value Engineered Environmental Payload; MARS -- Multi-functional Acquisition and Reporting System.

Two averaging methods are used to calculate wind speed. The first technique applies to those measurements reported by all DACT and VEEP payloads. In this method, the average wind speed is the simple scalar average of the wind speed observations. The second method, used by the majority of NDBC buoys employed in this study (those outfitted with the GSBP payload), is a true vector average. In this procedure, the magnitude of the vector

is represented by the wind speed observation and the direction observations are used for orientation. The vectors are then broken down into their u and v components. All u and v components are then averaged separately. The resulting average speed and direction are calculated from the Pythagorean theorem and "arctan(v/u)", respectively. (Gilhousen, D.B., 1987)

The electronic payloads installed on moored buoys generally transmit data to one of the NOAA's Geostationary Operational Environmental Satellites (GOES) each hour. The GOES relays the data message to the NESDIS Data Acquisition Processing System (DAPS) at Wallops Island, VA. Next, DAPS sends the data to the National Weather Service Telecommunications Gateway (NWSTG) where gross data quality control is performed before the data are distributed in meteorological codes in real time (less than 30 minutes).

NWSTG also sends the raw satellite and the NWSTG quality controlled data to NDBC where the data are recomputed from the satellite message, and are put through a series of automated and manual checks. The result is that data processed and archived at NDBC are of a higher quality than the real time data disseminated by NWSTG (Figure 5). Archived NDBC data is available on CD-ROM.

NDBC moored buoys are each assigned a World Meteorological Organization (WMO) station identifier composed of five numeric characters. For moored buoys these identifications are location specific. WMO identifiers are in the form of "&&###" where "&&" represents a WMO oceanic or continental region and ### denotes a specific location (e.g., 46042, 41003). With respect to regions, 32 denotes stations in the Pacific off the coast of South America, 41 -- the Atlantic off of the southeast U.S. coast, 44 -- the Atlantic Ocean north of North Carolina, 42 -- the Gulf of Mexico, 45 -- the Great Lakes, 46 the U.S. coastal Pacific Ocean, 51-- the Hawaiian Islands, 52 -- Guam.

2. Tropical Ocean-Global Atmosphere (TOGA)

The widespread and systematic influence of the El-Nino-Southern Oscillation meteorologic phenomenon, which is characterized by a weakening of the trade winds and warming of the surface layers in the equatorial Pacific Ocean every 4-7 years, led to the

initiation of the Tropical Ocean-Global Atmosphere (TOGA) Program. The TOGA program was designed as a ten-year study (1985-1994) of climate variability on seasonal to interannual time scales, whose success relied upon the accurate measurement of ocean surface winds, sea surface temperature, upper ocean heat content, near-surface currents, and sea level in the tropical Pacific ocean.

Plans for TOGA in the early 1980's called for an ocean observing system that would rely on an increased utilization of satellite products, in particular for surface winds, SST and sea level, and on the development of a "thin monitoring" array of in situ measurements based on an enhancement of existing capabilities. The in situ array would specifically include a volunteer observing ship (VAS), expendable bathythermograph (XBT) program, a tide gauge network, a drifting buoy program, and, most importantly, about 15 moorings located principally in the eastern Pacific (Figure 6) (U.S. TOGA Project Office, 1988).

The need for improved in situ observational capabilities in TOGA motivated Dr. Stanley P. Hayes of the NOAA's Pacific Marine Environmental Laboratory (NOAA/PMEL) to develop a wind and thermistor-chain mooring capable of telemetering its data to shore in real-time. He also conceived and directed the implementation of a basin-scale network of these moorings, which he called the TOGA Tropical Atmosphere Ocean (TAO) array (Hayes et al., 1991). TOGA-TAO far exceeded in scope what had been originally anticipated as a moored array component to the TOGA observing system. By December, 1994 TAO consisted of 70 moorings supported by a multi-national base. Beginning in 1989, relative humidity sensors were added for studies of atmospheric boundary layer dynamics and air-sea exchange processes. Expansion of the array was achieved during the second half of TOGA (1990-1994).

TOGA was intended to examine long-term oceanographic phenomena. Therefore, the standard output was a daily averaged wind speed. However, some buoys were equipped with onboard storage that allowed retrospective instantaneous (6 minute) measurements of wind speed suitable for this study.

TAO data are made available to the research community directly from PMEL via

Internet file transfer protocol (ftp) procedures, and via a dial-up phone line data base. In addition, PMEL retransmits a subset of the real time TAO data stream on the Global Telecommunications System (GTS) by Service Argos, so that the meteorological measurements are available for assimilation into atmospheric numerical weather prediction at places like the FLENUMMETOCEN (Figure 7).

C. SPECIAL SENSOR MICROWAVE/IMAGER

1. Instrument Description

The first SSM/I instrument was flown aboard DMSP spacecraft F8 in 1987 (Figure 8). Today, identical SSM/I instruments are in orbit aboard spacecrafts F10, F11, F12 (failed) and F13. This study used SSM/I data obtained from spacecrafts F8, F10 and F11.

DMSP satellites are in sun-synchronous, near-polar orbits at an altitude of approximately 833 km (Figure 9). The spacecraft has an orbital angle of inclination relative to the equatorial plane of 98.8° and an orbit period of 102 minutes, producing 14.1 full orbit revolutions per day. The radiometer scans conically at an angle of 45 degrees from the spacecraft resulting in an observation angle of incidence of approximately 53.1° . The SSM/I rotates continuously at 31.6 rpm about an axis parallel to the local vertical and measures surface brightness temperature over an angular sector of 102.4° about the sub satellite track. The scan direction is from left to right when looking in the aft direction of the spacecraft with an active scene measurement lying $\pm 51.2^\circ$ about the aft direction. This results in a swath width of 1400 km. The SSM/I moves along the sub-satellite track in the negative 'Y' direction at 6.58 km/sec which results in a separation between successive scans of 12.5 km along the satellite track direction and is nearly equal to the resolution of the 85 GHz beams. During each scan 128 uniformly spaced samples of the 85.5 GHz channels are taken over the scan region. Radiometer data at the remaining frequencies are sampled every other scan with 64 uniformly spaced samples being taken. Scan A denotes scans in which all channels are sampled while Scan B denotes scans in which only the 85.5 GHz data are taken.

Figure 10 shows the satellite subtrack coverage over successive days. There are

small unmeasured circular sectors of 2.4° at the north and south poles (Hollinger 1991). One spacecraft will not cover the entire surface every day, but horizontal coverage is dense enough for deriving wind speeds over most of the oceanic areas up to two times per day, (Schluessel et al., 1991).

The SSM/I is a seven-channel, four frequency, linearly polarized passive microwave radiometer. The instrument receives vertically polarized radiation at 22.2 GHz and both vertically and horizontally polarized radiation at 19.3, 37.0 and 85.5 GHz. The 19.3 GHz channel exploits the atmospheric window that exists at that frequency to sense ocean surface brightness temperatures. The 22.2 GHz channel corresponds to the water vapor line at that frequency and is used to obtain column water abundance and humidity profiles. The 37.0 GHz channels exploit the atmospheric window that exists at that frequency prior to the onset of the oxygen absorption band. The 85.0 GHz channel is designed to permit higher spatial resolution, but is not used in this study.

The antenna system consists of an offset parabolic reflector focusing the Earth's radiation into a broadband, seven port feedhorn. This assembly, including parabolic reflector, feedhorn and receiver, spins about an axis parallel to the spacecraft vertical at a period of 1.9 s. Attached to the spin axis but not rotating are a cold sky reflector and warm reference load. With this arrangement the feedhorn assembly will sense the fixed cold reflector and warm load once each scan. This allows in flight calibration observations to be taken every scan and represents a significant improvement over previous passive microwave radiometers.

2. Radiometer Calibration

To ensure optimum performance of the SSM/I, the antenna temperature is carefully calibrated. The antenna temperature is not the physical temperature of the antenna. Rather, it is the power received per frequency bandwidth, divided by Boltzman's constant:

$$(12) \quad T_A(v) = \frac{P(v)}{k\Delta v}$$

T_A is the weighted average of the scene temperature viewed by the antenna, where the weighting is determined by the gain of the antenna. The more closely the gain approaches a delta function the better the measurement of the true brightness temperature. If the gain does not approximate a delta function, then other sources of radiation, particularly those radiating into the sidelobes, contribute to the signal. Brightness temperature (T_B), antenna temperature (T_A) and gain (G) are related by:

$$(13) \quad T_A(v) = \frac{1}{4\pi} \int_{\Omega} T_B(v) G(v) d\Omega .$$

The accuracy of the measured antenna temperature depends on the accuracy of the calibration sources. The typical flight radiometer, like the SSM/I, uses a two-point temperature calibration where an on board warm target and the cold space background are used to obtain the calibration. In this case, the antenna field of view is enclosed with a temperature controlled microwave absorber (or *load*) at each of two temperatures, T_{hot} and T_{cold} . If the radiometer is linear, then the antenna temperature T_a for a target at an unknown temperature becomes:

$$(14) \quad T_a = c(V - V_0)$$

where V_0 is the voltage offset due to the receiver temperature and the radiometer calibration constant c is determined as

$$(15) \quad c = \frac{T_{\text{hot}} - T_{\text{cold}}}{V_{\text{hot}} - V_{\text{cold}}}$$

where the voltages V_{hot} and V_{cold} are the measured output voltages for the respective T_{hot} and T_{cold} loads (Janssen, 1993).

In the case of the SSM/I, the calibration error of the hot load is measured first prior to launch, during the thermal vacuum calibration. Thermal vacuum radiometer calibration

is accomplished using two precision microwave reference targets, each instrumented with eight precision platinum temperature sensors, as well as the spacecraft hot load to simulate an operational configuration. A liquid nitrogen cooled precision target is substituted for the cold sky reflector, and a variable precision target is positioned over the feedhorn to simulate active scan data. Calibration error is measured by comparing the variable reference target temperature when equal to that of the hot load.

During flight, the spacecraft hot target is used as the calibration hot reference. The spacecraft hot reference is instrumented with three flight platinum temperature sensors.

The temperature of the variable target serves as a primary standard calibration reference for the in-orbit hot-load and cold targets used in thermal vacuum calibration.

For its cold reference the SSM/I possesses a calibration reflector that reflects the cold cosmic background into a calibration feedhorn designed to minimize the possible reception of extraneous energy from the spacecraft or from the earth. The radiometric temperature of the comic background is consistent with a blackbody radiator at 3 °K. (Hollinger et al., 1987)

D. MULTIPLE REGRESSION WIND SPEED RETRIEVAL ALGORITHMS

1. D - Matrix Algorithm

The first attempt at retrieving surface ocean wind speeds from SSM/I data was the linear regression, "D-matrix" algorithm developed by Environmental Research and Technology, Inc. (ERT) for Hughes Aircraft (Lo, 1983):

$$(16) \quad SW = C_{0j} + C_{1j} \cdot T_B(19H) + C_{2j} \cdot T_B(22V) \\ + C_{3j} \cdot T_B(37V) + C_{4j} \cdot T_B(37H) .$$

Equation (16) is valid only over open ocean, where the wind speed, SW, is in m/s and is referenced to a height of 19.5 m above the surface. The term T_{Bx} represents the brightness temperature of frequency/polarization combination "x". C_{ij} represents D-matrix coefficients where "j", the climate code index, is a number from 1-11 that represents of one of eleven (9

distinct) climate codes established by ERT according to a particular season and latitude band. As discussed earlier, microwave radiation at the SSM/I frequencies is heavily attenuated by rain. This phenomenon results in the obfuscation of wind speed signatures generated by waves and foam on the ocean surface. The amount of microwave radiation detected by the SSM/I under rainy conditions is, therefore, unreliable. Understanding this, ERT sought to "rain flag" conditions that might lead to unreliable measurements. The original D-matrix rain flag logic was (Hollinger, 1991):

IF: $T_B(19H) > 190\text{ K}$
OR: $[T_B(37V) - T_B(37H)] < 25\text{ K}$
Then possible rain flag exists and rain flag = 1

IF: $[T_B(37V) - T_B(37H)] < 10\text{ K}$
Then heavy rain exists and rain flag = 2

Otherwise rain flag = 0.

The accuracy specification for wind retrievals under rain flag = 0 (clear) conditions was $\pm 2\text{ m/s}$ over the range 3 to 25 m/s. Accuracy was not specified for winds retrieved under rain-flag 1 conditions, and retrieval was not even attempted under rain-flag 2.

2. Calibration/Validation (CV) Algorithm

Once the SSM/I aboard spacecraft F8 was launched and operating, the Naval Research Laboratory undertook to evaluate the effectiveness of the D-matrix algorithm in retrieving ocean surface winds. This process was accomplished by comparing SSM/I wind retrievals with coincident surface wind speed measurements taken from open ocean buoys maintained by NOAA. As the TOGA array had not yet been deployed, the buoys used were NDBC buoys located mostly in the mid-latitudes and set further than 100 km from land to avoid mixed land/ocean pixels.

Results of the validation showed that roughly 15% of the total data were rain flagged. Scatter plots that displayed the performance of the D-matrix algorithm against the buoy measured wind speeds revealed that the algorithm did not meet the specified accuracy requirement of $\pm 2\text{ m/s}$ in rain-flag 0 conditions (Figure 11). The D-matrix algorithm performed well near the global average wind speed of 7 m/s and performed poorly (both in

terms of standard deviation and bias) in high wind speed regions (> 15 m/s).

Armed with these findings, the NRL validation team sought to adjust the D-matrix algorithm so that it would meet the accuracy requirements. Using linear regression on paired buoy wind speeds and SSM/I brightness temperatures, a set of new coefficients for the algorithm were developed (Hollinger, 1991). The accuracy specifications were subsequently met (Figure 12), but the revised climate coded algorithm still underestimated high wind speeds and produced discontinuities across climate code boundaries (Goodberlet et al., 1989).

In 1989, Goodberlet et al. published a new, global algorithm which utilized a single set of coefficients valid in all latitudes and seasons. Coefficients for the global algorithm were generated using a weighted linear regression of the buoy wind speeds on the coincident SSM/I brightness temperatures. The weights used in the regression were set equal to 1 over the square root of the wind speed density function evaluated at the particular buoy wind speed. This type of weighting has the effect of making all wind speed ranges equally important, whereas the original unweighted D-matrix regression tended to emphasize those wind speed ranges where few data were collected. The improved D-matrix or Calibration/Validation (CV) algorithm is as follows (Goodberlet, et. al., 1989):

$$(17) \quad SW = 147.9 + 1.0969 \cdot T_B(19V) - 0.4555 \cdot T_B(22V) \\ - 1.7600 \cdot T_B(37V) + .7860 \cdot T_B(37H) .$$

In addition to revising the linear regression coefficients, new rain flag thresholds were determined. The new rain flag cutoffs were determined from plots of the D-matrix residual versus the D-matrix rain flag, by locating the values of the rain flag parameters for which either the standard deviation or bias curve crossed some predetermined accuracy level (normally 2 m/s). In this manner four new rain flags, separate and independent of the rain flags developed by ERT were defined (Goodberlet, et. al., 1989):

Rain Flag	Criteria	Accuracy
0	$T_B(37V) - T_B(37H) > 50$ AND $T_B(19H) < 165$	< 2 m/s
1	$T_B(37V) - T_B(37H) < 50$ OR $T_B(19H) > 165$	2-5 m/s
2	$T_B(37V) - T_B(37H) < 37$	5-10 m/s
3	$T_B(37V) - T_B(37H) < 30$	> 10 m/s

Once constructed, performance of the CV algorithm was tested against the same data used to examine the performance of the D-matrix algorithm. Use of the CV algorithm removed much of the high-wind speed bias and zonal discontinuity associated with the original algorithm. However, CV retrieval accuracies in rain flagged regions continued to exceed ± 2 m/s.

3. Improved Goodberlet, Swift, Wilkerson (GSW) Algorithm

In 1992, Goodberlet, Swift and Wilkerson modified the CV algorithm in an effort to improve wind speed retrieval accuracy, particularly in high moisture regimes. Improvement in retrieval accuracy under rain flagged conditions was partially achieved in the medium to high wind speed range (6-20 m/s). This improved performance was achieved in large part by abandoning a strictly linear algorithm and introducing a non-linear relationship between wind speed and brightness temperature with respect to the two polarized brightness temperatures at 37 GHz. Goodberlet et. al. empirically described the weather bias exhibited by the CV algorithm as:

$$(18) \quad W_G - W_T \approx \frac{B_1 - W_T}{(\Delta_{37}/B_2)^N}$$

where W_G is a wind speed retrieval from the CV algorithm and W_T is the corresponding true surface wind speed, and B_1 , B_2 , and N are 18.56, 30.7 and 4 respectively. The GSW wind speed retrieval algorithm was formed by solving for W_T in equation (18). The GSW

algorithm is as follows:

$$(19a) \quad W_{GSW} = \frac{W_G - 18.56 \cdot \alpha}{1.0 - \alpha} ,$$

where W_G is equation (18) and,

$$(19b) \quad \alpha = \left(\frac{30.7}{\Delta_{37}} \right)^4 .$$

In each case, $\Delta_{37} = T_B(37V) - T_B(37H)$. The GSW algorithm can be reliably used under conditions when the Δ_{37} differential is greater than 40 K and, with care, when Δ_{37} is greater than 35 K. The GSW algorithm should be used with caution for Δ_{37} less than 35 K and should not under any circumstances be used when Δ_{37} is less than 31 K (Goodberlet et al., 1992). It is clear from equation (19b) that when Δ_{37} approaches 30.7 K, equation (19a) has a singularity and the expression becomes meaningless. Unfortunately, Δ_{37} measurements less than 31 K often correspond to higher moisture regimes which may be of interest.

Because the modifications to the CV algorithm that resulted in the GSW algorithm were made based only on F-8 SSM/I brightness temperature data, Goodberlet et al. further state that the GSW algorithm can be reliably applied only to data from SSM/I F-8. This study, however, will demonstrate, among other things, how the GSW algorithm performs on data from other SSM/I instruments.

E. ARTIFICIAL NEURAL NETWORK WIND SPEED RETRIEVAL METHODS

An alternative method for retrieving wind speeds from SSM/I data is through a method of artificial intelligence known as the neural network. The simplest definition of a neural network, is provided by the inventor of one of the first neurocomputers, Dr. Robert Hecht-Nielsen. He defines a neural network as (Caudill, 1989):

"... a computing system made up of a number of simple, highly interconnected processing elements, which process information by their dynamic state response to external inputs."

Neural networks are processing devices that are loosely modeled after the neuronal structure of the mammalian cerebral cortex. Artificial neural networks cannot yet approach the complexity of those found in nature, yet they may have hundreds of thousands of processor units.

Neural networks are typically organized in layers. Layers are made up of a number of interconnected "nodes" which contain an "activation function". Patterns are presented to the network via the "input layer", which communicates to one or more "hidden layers" where the actual processing is done via a system of weighted "connections". The hidden layers then link to an "output layer" where the answer is output (Figure 13).

Most neural networks contain some form of "learning rule" that modifies the weights of the connections according to the input patterns that it is presented with. Like the mammals they are designed to emulate, neural networks "learn" by example.

One of the most common learning rules used by neural networks is the delta rule. The delta rule is often utilized by the most common class of neural networks - called backpropagational neural networks (BPNN's). Backpropagation is an abbreviation for the backwards propagation of error.

With the delta rule, as with other types of Backpropagation, "learning" is a supervised process that occurs with each cycle through a forward activation flow of outputs, and the backwards error propagation of weight adjustments. In short, when a neural network is initially presented with a pattern it makes a random guess as to what it might be. It then sees how far its answer was from the actual one and makes an appropriate adjustment to its connection weights.

Once a neural network is "trained" to a satisfactory level it may be used as an analytical tool on other data. To do this, the user no longer specifies any training runs and instead allows the network to work in forward propagation mode only. New inputs are presented to the input pattern where they filter into and are processed by the middle layers as though training were taking place, however, at this point the output is retained and no backpropagation occurs. The output of a forward propagation run is the predicted model for

the data which can then be used for further analysis and interpretation.

Whereas conventional computing systems are deterministic, sequential and logical, neural networks are not. There are no complex central processors, rather there are many simple ones which do little more than take the weighted sum of their inputs from other processors. Neural networks do not execute programmed instructions, rather they respond in parallel to the pattern of inputs presented to it. Because a neural network can easily model non-linear phenomena which otherwise may be difficult to explain, they are useful in modeling meteorological phenomena like global ocean winds.

1. The Stogryn, Butler, Bartolac (SBB) Neural Network

The first neural network trained on a set of SSM/I brightness temperatures matched with buoy winds was developed by Stogryn, Butler and Bartolac (1994). Stogryn et al. employed a type of backpropagation neural network referred to as a feed forward fully connected neural network (Figure 14). In this design, the neurons of the input layer do no processing but provide copies of an input vector to the first processing layer. In the case of wind retrieval, the input vector is the brightness temperature. The neurons in subsequent layers form linear combinations of the outputs of neurons in the preceding layer, add an offset, and transform the result into an output signal. For layer N , the wind speed estimate \hat{s} is calculated as (Stogryn et al., 1992):

$$(20) \quad \hat{s} = \psi x^N + \beta ,$$

where ψ is a scale factor and β is an offset.

Stogryn et al. partitioned the same F8 SSM/I data set used by Goodberlet et al. for the calibration/validation of the D-matrix into two sets, one for training the neural network and the other for testing it. The SBB neural networks were trained and tested using primarily the 19V, 22V, 37V, and 37H SSM/I channels as input data. The 19H channel was used to help discriminate clear from cloudy or rain conditions and in determining which network to use. The training/test sets were further divided into three subsets. The first contained all SSM/I buoy matchups in designated "clear" conditions:

$$T_B(37V) - T_B(37H) > 50 \text{ K} .$$

The second subset included SSM/I buoy matchups that occurred under "cloudy" conditions:

$$T_B(37V) - T_B(37H) \leq 50 \text{ K}$$

$$T_B(19V) < T_B(37V)$$

$$T_B(19H) \leq 185 \text{ K}$$

$$T_B(37H) \leq 210 \text{ K} .$$

The third subset comprised those matchups exceeding the cloudy condition criteria and represents conditions where attenuation effects render the retrieval of wind speeds unwise.

Using two separate feed forward fully connected neural networks, Stogryn et al. achieved dramatic improvements in performance on the partitioned data set. The SBB neural networks claimed a 30 % improvement in wind retrieval accuracy for clear conditions over earlier linear regression wind retrieval methods, and a 250% improvement under cloudy conditions. Attempts to further improve performance of the SBB neural networks by increasing the number of neurons per layer and/or the number of layers, met without significant success. These advances notwithstanding, application of the SBB neural network remains limited as it was trained on a relatively restricted data set comprised solely of data provided by the SSM/I aboard spacecraft F8. Most importantly, this data set does not include clear day wind speed values greater than 18 m/s.

2. The Krasnopolosky, Breaker, Gemmill (NMC) Neural Network

In 1994, Kransnopolosky, Breaker and Gemmill of the National Meteorological Center published a single "all-weather" neural network algorithm for estimating ocean surface winds from the SSM/I. This neural network sought to improve upon the results achieved previously by Stogryn et al. by eliminating the necessity for partitioning wind speeds based on "clear" and "cloudy" atmospheric conditions, thereby avoiding the uncertainties that necessarily arise in the region that separates the two regimes. In addition, the NMC neural network was designed so that its application could be extended to atmospheric conditions where higher levels of moisture exist - regions where previous algorithms had performed poorly. As a result, the NMC neural networks were trained to

cover adverse atmospheric conditions considered by SBB to be beyond the region where useful retrievals could be obtained.

The data used by Krasnopolsky et al., to train and test their neural networks is the same data set used previously by GSW and SBB to formulate their algorithms. The brightness temperatures were acquired from the SSM/I flown aboard DMSP satellite F8. Again, matchups were produced only when the SSM/I retrievals were within 25 km of the buoy location and the time of satellite data acquisition was within 30 minutes of the buoy observation. As before, wind speeds were adjusted to a standard height of 19.5 m. Finally, as was the case in the SBB neural networks, neither the training nor the test data set included wind speeds greater than 18 m/s.

In an effort to reproduce the results of SBB and make their findings directly comparable with those of SBB, the NMC group adopted the same neural network design architecture. NMC constructed a feed-forward, fully-connected neural network that employed back propagation. The NMC neural network contains three layers, a four node input layer (layer 0), one two node hidden layer (layer 1), and a single node output layer (layer 2). At the nodes in layers 1 and 2, linear combinations of the outputs from the nodes in the previous layers (layers 0 and 1) are formed. The combined input to node j in layer 1 can be expressed:

$$(21) \quad y_i = \sum_{j=1}^n \Omega_{ij} t_j + B_i$$

where the t_j are the four input brightness temperatures, Ω_{ij} are the weights, B_i are biases, and $j = 1, 2$ (nodes of hidden layer). Combining this input into an output at each node requires a nonlinear transfer or "squashing" function. Thus, the output for the i -th node is expressed:

$$(22) \quad x_i = f(y_i)$$

where f is the squashing function:

$$(23) \quad f(x) = \tanh(x)$$

The bias term, B_i , serves to center the squashing function about the ordinate which makes the training process more efficient. The output of hidden node x_i provides the input to the output node, which in turn produces the neural network output:

$$(24) \quad Net = b + \alpha f \left(\sum_{i=1}^m \omega_i x_i + \beta \right)$$

where the ω_i are the weights, β is the bias, and α and b are scaling factors. (Krasnopolksy et al., 1994)

Once the training is complete and weights have been determined, the desired wind speed, W (m/sec), is calculated as:

$$(25) \quad W = Net(T)$$

where T is the input vector of brightness temperatures (Krasnopolksy et al., 1994).

Prior to training the network, initial weights for each of the connections within the network are specified. Next, the brightness temperature inputs are applied to the neural network and the output wind speed is calculated. This output is then compared to the observed wind speed contained in the matchup. The difference between the calculated wind speed and the target wind speed is fed back (backpropagation) through the network and the weights at each node are changed until an acceptably small error is realized. (Krasnopolksy et al., 1994)

Training takes place as the network is repeatedly exposed to matched pairs of SSM/I brightness temperatures and buoy wind speed. After exposure, the weights and biases are adjusted according to the backpropagational algorithm until convergence is achieved. During training several hundred thousand iterations were required to achieve convergence. (Krasnopolksy et al., 1994)

III. STUDY PROCEDURES

The linear regression algorithms and neural networks used to retrieve ocean wind speeds from SSM/I data have all been developed and tested using the same SSM/I - NOAA buoy pair data base used to validate the original D-matrix algorithm. That data is for spacecraft F8 during the period 10 July 1987 through 31 March 1988 and consists of NOAA buoys that lie predominately in the mid-latitude ocean region. The lack of algorithm validation against buoys in equatorial regions, where lower wind speeds dominate, was discussed at the SSM/I Algorithm Symposium, held in June 1993, as was the need for an expanded data set that would encompass regions varied enough for the SSM/I - NOAA buoy pair data set to be considered truly global. This study seeks to validate the performance of four wind speed retrieval methods over an expanded data set that represents, as closely as possible, the wind speed distribution found throughout the world.

For this study SSM/I wind speed retrievals from the DMSP F8, F10 and F11 space crafts were taken over a 6 month period from September 1991 to April 1992 and compared to in-situ buoy wind speed measurements for the same period. SSM/I wind speed retrievals were obtained using the CV and GSW linear regression algorithms and the SBB and NMC neural networks.

A. BUOY DATA SET

The in-situ buoy wind speed data were obtained from two sources - TOGA buoys and NDBC buoys. TOGA buoy data were provided by the Pacific Marine Environmental Laboratory (PMEL) while NDBC data were provided by the National Oceanic Atmospheric Administration (NOAA). Not all of the TOGA buoys that comprise the TOGA array were used in this study. Those that were used are listed in Appendix B Table 1. Nineteen NDBC buoys were used. To prevent land contamination of ocean brightness temperatures and to insure that the land did not restrict the wind speed fetch distance necessary for creating fully developed seas, only NDBC buoys further than 100 km from land were chosen (Appendix B Table 2) (Ulaby et al., 1986).

The meteorological parameters collected from the buoys include: wind speed, air temperature, sea surface temperature, relative humidity and barometric pressure. TOGA buoy wind speed measurements were made at a height of 3.8 meters above the ocean surface. NDBC buoy wind speed measurements were taken at a height of either 5 or 10 meters depending on the model of buoy. In the case of both buoys, the recorded wind speeds were converted to an equivalent wind speed at 19.5 meters above the ocean surface, the height at which SSM/I wind speeds are calculated, using Smith's (1988) open ocean drag coefficient.

B. SSM/I-BUOY MATCHUP CRITERIA

The matchup of SSM/I retrieved winds with in-situ buoy winds was conducted along the lines of the original D-matrix calibration/validation. For this study, SSM/I wind speeds for each of the four wind retrieval methods were matched with buoy wind speeds. The SSM/I wind speeds and buoy wind speeds were paired by the Naval Research Laboratory when the SSM/I retrieval was located within 25 km of the buoy position and the SSM/I overpass time was within 30 min of the buoy wind speed measurement. According to the work of Monaldo (1988), the average value of these spatial and temporal differences increases the total allowed standard deviation of 2 m/s by less than 10% (Goodberlet et al., 1989). SSM/I geolocation problems reported by Hollinger (1991) are insignificant at a spatial separation of 25 km. NDBC buoys make an 8.5-min. average of the wind once every hour with an accuracy of \pm 0.5 m/s for winds less than 10 m/s and 5% for winds greater than 10 m/s (Gilhousen, 1986). Additional sources of error include the uncertainties associated with the fact that the buoy winds are averaged over an 8.5 min. period whereas the SSM/I measurements are instantaneous. Finally, the paired SSM/I and buoy measurements may differ, of course, by up to 25 km and 30 min.

Because the SSM/I field of view is a swath of 1400 km, a single SSM/I overflight may produce several wind speed retrievals that meet the spatial and temporal criteria. Such a set of retrievals are highly correlated with each other (Goodberlet et. al, 1989). To overcome this, three different methods of generating a single SSM/I wind speed retrieval

from an overpass were employed. The first involves finding the SSM/I retrieval that is spatially nearest to the buoy; this measurement is termed the "nearest neighbor". The second method is to take a straight average of all of the SSM/I retrievals that meet the matchup criteria and generate a single SSM/I wind speed. Third, an inverse distance weighted average of the brightness temperatures was computed.

For the six month period of this study, a total of 127,524 SSM/I measurements were generated by the SSM/I that met the spatial and temporal matchup criteria - an average of 18 correlated SSM/I measurements for each buoy wind speed measurement. Of this total, 93,125 SSM/I measurements are matched with NDBC buoys, while 34,399 SSM/I measurements are coincident with TOGA buoys. There are a greater number of NDBC matchups because there are more NDBC buoys than TOGA buoys included in the study.

From the total 127,524 data points, 7085 independent, uncorrelated observations were distilled - 5427 NDBC buoy matchups and 1658 TOGA buoy matchups. There are, therefore, 7085 nearest neighbor data points that comprise the global data set upon which most of the data analysis contained herein is conducted.

C. WIND SPEED DISTRIBUTION

Figure 15 shows the distribution of wind speeds measured by in-situ TOGA and NDBC buoys for the sixth month period examined in this study, September 1991- April 1992. The term "global" refers to the combined data set comprised of both TOGA and NDBC buoy measurements. Figure 16 displays roughly 500,000 wind speed measurements obtained from TOGA and NDBC buoys over a full two year period. A comparison of Figures 15 and 16 clearly demonstrates that the distribution of wind speeds comprising the study data set are representative of the global winds likely to be found in the sampled regions over an extended period of time.

Importantly, the study data set includes significant numbers of data representing wind speeds in excess of 20 m/s and less than 3 m/s, permitting the validation of wind speed retrieval methods in these regions. The locations of the buoys used in this study are shown in Figure 17. The objective, then, is to evaluate the four wind speed retrieval methods over

a range of wind speeds that are reasonably representative of a known distribution of global wind speeds.

IV. OBSERVATIONS

A. SSM/I WIND SPEED VS IN-SITU BUOY WIND SPEED

1. All SSM/I -Buoy Matchups

The first comparisons made to determine the efficacy of each of the four wind speed retrieval methods employed the full 127,524 data points meeting the spatial and temporal matchup requirements. None of the "rain flags" developed for use by the respective wind retrieval methods were applied to the data. Figures 18-22 give a first cut estimation of how well each method performs. A least squares fit is calculated and displayed against a diagonal reference line that represents a perfect match between SSM/I retrieved wind speed and the measured buoy wind speed. Figure 18 shows that the CV algorithm overestimates wind speeds by roughly 2.7 m/s. Figure 19 displays only the CV algorithm measurements that are coincident with the lower wind speed regions associated with TOGA buoys. In the lower wind speed regime, the CV algorithm overestimates wind speeds by 3.9 m/s. This problem was recognized by the authors of the CV algorithm and led, in part, to the formulation of the improved Goodberlet, Swift, Wilkerson (GSW) algorithm.

Figure 20 demonstrates the improved performance of the GSW algorithm over the CV algorithm for the same data set. The GSW algorithm overestimates total wind speeds by only 1 m/s - a marked improvement. Figure 21 shows that the GSW performs better than the CV algorithm largely because of increased performance in the low wind speed regions. The improvement in performance achieved by the GSW algorithm over the CV algorithm is discussed in greater detail later.

Figures 22 and 23 examine the performance of the SBB and NMC neural networks, respectively, over the same, non-rainflagged 127,524 point data set. At the lower wind speeds, the two neural networks overestimate buoy wind speed by up to 3 m/s. Agreement with buoy wind speed measurements is achieved, in both neural networks, at approximately 7 m/s - the global wind speed average. As wind speed increases beyond 7 m/s, the neural networks display a tendency to increasingly underestimate buoy wind speed.

Underestimates of buoy wind speed range from 8-12 m/s at wind speeds of 20-22 m/s. These characteristics are similar to those reported by Sayward (1994) based on his three month TOGA buoy analysis.

2. Nearest Neighbor, Average or Weighted Average SSM/I Data

The remainder of the data analysis conducted in this study focuses on the performance of the four wind retrieval methods upon the smaller, uncorrelated data set comprised of the single nearest neighbor, average, or weighted average value retrieved for each buoy wind speed measurement. Furthermore, the rain flags developed for each of the wind retrieval methods (with the exception of the "all weather" NMC neural network") are included. Recall, however, that the term "rain flag" is somewhat of a misnomer. Rain flag tags indicate any condition (including rain) which leads to reduced retrieval accuracy. Therefore, wind retrieval methods are examined under the conditions their authors intended. Table 3 shows the number of data points included in each rainflagged subset of the 7085 point uncorrelated data set for each of the three wind speed retrieval methods that employ rain flags.

The first set of plots applied to the uncorrelated data set examines the performance of each wind retrieval method under "clear" conditions which vary depending upon the retrieval method. Because the original D-matrix algorithm was required to meet the DMSP specification of ± 2 m/s, the standard deviations achieved by the four wind speed retrieval methods are a primary measure of achievement. Furthermore, it is assumed that the DMSP requirement refers to the standard deviation, in an average sense, of the difference between all coincident buoy and SSM/I wind speed measurements. Admittedly, this interpretation can disguise the fact that over certain wind speed subintervals the accuracy of a given wind speed retrieval method may exceed 2 m/s. This is often true for regression-type algorithms, like the CV and GSW algorithms, which tend to make especially good predictions near the overall average wind speed and predictions of less accuracy for wind speeds which are removed from the average wind speed (Goodberlet et al., 1989).

Figures 24-27 are scatter plots which illustrate the effectiveness of the four wind

speed retrieval methods in clear conditions. In these figures, the horizontal axis represents the range of buoy wind speed measurements and the vertical axis represents the SSM/I nearest neighbor wind speeds retrieved using a particular method. For each method a plot was generated using nearest neighbor (nn), average (avg) and weighted average (wavg). Tables 4-6 summarize the results for the TOGA, NDBC and combined (global) data sets, respectively.

Table 4 shows that all four wind speed retrieval methods possess acceptable standard deviations of less than 2 m/s. The standard deviation of the two neural networks is lower than the standard deviation achieved by the two linear regression algorithms. The smallest standard deviation is achieved by the NMC neural network. In addition to performing slightly better than the linear regression algorithms in terms of standard deviation, the neural network retrievals display significantly better correlation. The linear regression algorithms, however, possess far better slopes to their linear least squares fit lines and display less bias. The GSW algorithm clear weather data bias, in particular, is superlative.

In every measure of performance, the GSW algorithm performs better than the CV algorithm it was designed to improve upon. This improvement, however, is due in large part to the far more restrictive clear day brightness temperature criteria imposed by the GSW algorithm. Of the total 7085 data points in this set, only 63% of GSW data appears as clear day while 81% of CV data appears as clear day.

Using a single SSM/I average or weighted average data point to coincide with buoy measured wind speed, as opposed to the nearest neighbor, degrades the slope and bias of each of the wind speed retrieval methods. At the same time, an average or weighted average value slightly increases each method's performance in terms of correlation and, most importantly, standard deviation.

The next series of figures (Figures 28-33) display the error in SSM/I retrieved wind speeds plotted against buoy wind speeds. For these plots the 7085 nearest neighbor SSM/I values were plotted against their coincident buoy values. In Figure 28, CV rain flags 0, 1, 2 and 3 are represented by circles, diamonds, squares and crosses respectively. The symbols

are the same for the GSW algorithm shown in Figure 29 excepting rain flag 3, which the GSW algorithm does not possess. The SBB neural networks' two rain flags representing clear and cloudy conditions are represented by circles and diamonds (Figure 30). The NMC neural network does not contain rain flags since Krasnopolsky et al. developed the NMC neural network without partitioning the data based on atmospheric moisture conditions. The NMC data was, however, filtered through the CV rain flag algorithm so that values of $\Delta 37$ greater than 165 - 5 % of the data set - are not included (Figure 31).

In Figure 28, for rain flag 0, the CV algorithm generates a distribution of wind speeds that correlate reasonably well with buoy wind speeds within the 5-14 m/s wind speed range. Rain flag 0 wind speed retrievals for very low wind speeds are biased slightly high while those greater than 14 m/s are biased slightly low. The algorithm performs increasingly poorly as atmospheric conditions deteriorate, as evidenced by the appearance of rain flagged data. Values retrieved under rain flag conditions significantly overestimate wind speeds throughout the range of observed wind speeds - severely at low wind speeds and less severely at higher wind speeds. Figure 32 clearly demonstrates the high wind speed bias exhibited by CV wind speeds retrieved under rain flag conditions in equatorial regions.

Figure 29 shows how the GSW algorithm performs over the full range of wind speeds when its more discriminating rain flags are applied. In contrast to the CV algorithm, the GSW rain flag 0 data tend to underestimate winds overall, including the 5-10 m/s range where most wind speed values are registered. At lower wind speeds, the GSW rain flag 0 retrievals agree fairly well with measured values. As wind speed increases, however, the GSW rain flag 0 retrievals increasingly underestimate wind speed. The GSW algorithm achieves some success in attenuating the high wind speed bias displayed by CV rain flagged retrievals in equatorial regions (Figure 33). These GSW values remain biased high, however. In contrast to the CV algorithm, rain flagged GSW retrievals at higher wind speeds (>15 m/s) increasingly *underestimate* measured wind speed. GSW rain flag 2 data, in particular, is prone to sizeable error.

The SBB neural network is shown (Figure 30) with only clear and cloudy conditions

plotted. Although SBB acknowledge a third "very cloudy" condition, a neural network was not developed for this case; very cloudy points are therefore excluded. SBB rain flag 0 data displays a distinct inclination to underestimate wind speed as measured wind speed increases. For winds in the 0-5 m/s range, SBB exhibits a slightly high bias. From 5-10 m/s, SBB underestimates measured wind by up to 4 m/s. Beyond 10 m/s SBB accuracy falls off steadily so that low bias errors up to 8 m/s are observed. The pattern is the same for SBB retrievals under cloudy conditions, except that in the cloudy case the high bias at low wind speeds and the low bias at high wind speeds are more pronounced.

The NMC neural network does not employ rain flags. Yet, the NMC neural network, too, exhibits increasingly low bias as measured wind speed increases (Figure 31). NMC retrieved wind speeds overestimate wind speed in the 0-5 m/s range, increasingly underestimate wind speed in the 5-10 m/s range, and significantly underestimate wind speeds greater than 10 m/s. At very high winds (>20 m/s), NMC retrieved winds underestimate measured wind speed by up to 10 m/s.

B. BRIGHTNESS TEMPERATURE-BASED DATA PARTITIONING

Due to existing shortcomings in the theoretical models used to describe radiometric emission from the ocean as a function of wind speed, most retrieval algorithms are necessarily empirical. Moreover, until the development of the GSW algorithm they were usually linear (e.g., D-matrix, CV). Each algorithm has been developed for specific atmospheric conditions. Three of the four algorithms (excepting NMC) used in this study employ brightness temperature as the primary basis for discriminating between various levels of atmospheric moisture and to establish rain flags and retrieval criteria. Because of its overriding importance in the development of wind speed retrieval algorithms, the next group of figures in this study examines more closely the performance of algorithms in regions partitioned according to brightness temperature.

Figure 34 illustrates the CV error (SSM/I wind speed - buoy wind speed) plotted against the difference of brightness temperature, Δ_{37} (37 GHz (V) - 37 GHz (H)), prior to the application of rain flags. Figure 35 shows the same plot after the CV rain flags have

been applied. Figure 35 shows that the algorithm performs quite well in the region above $\Delta_{37} = 50$. Below $\Delta_{37} = 50$, the algorithm performs increasingly poorly, tending to overestimate the buoy wind speed. Below $\Delta_{37} = 30$, the algorithm frequently overestimates winds by up to 20 m/s. Indeed, in high moisture region several data points (not shown) exceed 20 m/s.

Figure 36 illustrates the GSW error (SSM/I wind speed - buoy wind speed) plotted against the difference in brightness temperature, Δ_{37} , prior to assigning rain flags. Of note in this figure is the extreme low bias evident below $\Delta_{37} = 35$. This shows that in an attempt to rectify the high bias exhibited by the CV algorithm in high moisture regions, the GSW algorithm coefficients provide a low bias counterweight. Recognizing that a bias, albeit in different form, still exists in the high moisture regions, GSW applies a strict rain flag to prohibit the use of the GSW algorithm in this region (Figure 37). In Figure 37, points below $\Delta_{37} = 32$ are not plotted as recommended by the algorithm's authors. Above $\Delta_{37} = 45$, the algorithm wind speed is biased slightly low, although the vast majority of the bias lies within the region ± 5 m/s. Below $\Delta_{37} = 45$ down to $\Delta_{37} = 32$, the algorithm performs increasingly poorly, with both high and low wind speed bias error escalating.

Figures 38 and 39 illustrate that, although the error associated with $\Delta_{37} < 50$ is slightly higher than that for $\Delta_{37} > 50$, in general, the performance of the SBB neural network does not significantly depend upon the Δ_{37} parameter. Similarly, the NMC neural network, which is based only in part on brightness temperature, appears to operate equally effectively in all moisture regions (Figure 40).

C. PHYSICAL PARAMETER-BASED DATA PARTITIONING

More recently, a number of SSM/I algorithms have been developed to estimate various moisture-related quantities such as liquid water path (LWP), water vapor path (WVP) and rain rate (RR). Other algorithms use a combination of brightness temperature data and physical parameters to retrieve a wind speed. The NMC algorithm, for example, uses LWP, WP and RR algorithms, in addition to brightness temperature information, to classify its data (Krasnopolsky et al., 1994). Schlussel and Luthardt (1991) estimate wind

speeds from the SSM/I using *simulated* brightness temperatures obtained by calculating the radiative transfer from the ocean surface through the atmosphere for five of the seven SSM/I channels. These results are applied to a global set of vertical profiles of temperature and humidity (Krasnopolsky et al., 1994). The next set of figures examines, in greater detail, the role that the physical parameters water vapor, cloud water, relative humidity and barometric pressure play in the effective retrieval of SSM/I winds.

For this comparison, water vapor (WV) and cloud liquid water (CW) values are obtained from SSM/I channels 22.2 GHz and 85.5 GHz. Water vapor is the gaseous atmospheric water constituent whereas cloud liquid water is that portion of the liquid atmospheric water consisting of water droplets too small to precipitate - generally having radii less than 100 microns. Figure 41 and 42 further reinforce earlier findings regarding the performance of the CV algorithm in high moisture conditions. The algorithm displays a nominally high wind speed bias under low moisture conditions but increasingly overestimates wind speed as the atmospheric moisture content increases. Overestimation of in-situ wind speeds by 10 m/s or more occurs when water vapor content exceeds 50 kg/m^2 and when cloud water values exceed 0.35 kg/m^2 . As expected, the rain flagged values associated with lower Δ_{37} values and corresponding to higher water vapor content, exhibit the greatest error.

Figure 43 shows that, for the GSW algorithm, wind speed bias is slightly high for water vapor content values ranging from $5-12 \text{ kg/m}^2$, is generally low for values ranging from $13-50 \text{ kg/m}^2$. Above 50 kg/m^2 exhibits significant low and high wind speed error. Rain flag 1 data above 50 kg/m^2 is clearly biased low, providing further evidence of the effect the refined GSW coefficients have on the performance of the algorithm in regions of high moisture content. Similar tendencies are evident in the cloud liquid water plot (Figure 44). Again, the severe low wind speed bias is exhibited in high moisture regions.

Figures 45 and 46 illustrate the performance of the SBB neural network over the range of water vapor and cloud liquid water values. The SBB neural network performs nearly uniformly, exhibiting a marginally low wind speed bias over the entire range. In

addition, it is clear from Figure 45 that the neural network performs worse under rain flag 1 (cloudy) conditions than in rain flag 0 (clear) conditions - irrespective of the amount of water vapor present. Similarly, the NMC neural network is biased low over the range of water vapor and cloud liquid water values (Figures 47 and 48).

V. ANALYSIS

This chapter examines more closely the performance results described in the previous chapter, and endeavors to explain where and why the performance of any given wind speed retrieval method is degraded.

A. CV ALGORITHM

The CV algorithm represents the first effort undertaken to improve the original D-matrix algorithm. Subsequent to its development, the authors, Goodberlet, et. al., validated its performance. The buoys used to validate the CV algorithm, however, were NOAA buoys concentrated largely in mid-latitude regions. Many of the deficiencies uncovered by the algorithm's authors are reinforced by this study, despite its broader, more inclusive data set.

The CV algorithm's performance over the entire range of wind speeds in clear weather (rain flag 0) conditions is actually quite good ($SD < 2$ m/s). The algorithm possesses a very low overall bias (1.246) while retaining an impressive 81% of original data points to achieve clear day conditions. This is due, in large part, to the wind speed density weighting distribution developed by Goodberlet, et. al. (1989) which served to make all wind speed ranges equally important. Yet, in very low (< 3 m/s) and very high wind speed regions (> 15 m/s) the algorithm does not perform well.

That the CV algorithm performs poorly in both high and low wind speed regions is due in part to the fact that the data set upon which the coefficients for the CV algorithm is based was very nearly bereft of winds in these ranges. Furthermore, the CV algorithm performs poorly in regions of high moisture content. As a result, the accuracy of low wind speed retrievals from moist, equatorial regions is further degraded. Retrievals under conditions where water vapor content exceeds 50 kg/m² are especially poor.

B. GSW ALGORITHM

Attempts by Goodberlet et. al., to refine the CV algorithm resulted in the GSW algorithm - the first non-linear treatment of SSM/I data. In this study, each and every trial data set used to evaluate the performance of the different algorithms indicates that the GSW

algorithm performs better, overall, than the CV algorithm. However, the price paid to achieve this level of performance is steep. The CV algorithm employs 81% of all data for use in generating wind speed retrievals in clear day conditions - GSW uses only 63%.

The more restrictive rain flags employed by GSW effectively mitigate the high wind speed bias found at low wind speeds for CV. It accomplishes this task, however, largely by eliminating high moisture data points from the data set. Despite the very fine filter applied by the GSW algorithm to achieve improved accuracy, errors remain. Because GSW eliminates the data points which are the source of the high bias exhibited by CV, the majority of GSW retrievals are biased low, including those within the global average wind speed range. The mitigation of CV high bias due to elevated atmospheric moisture content is accomplished, in part, by replacing the strictly high bias values found in CV retrievals above 50 kg/m^2 and replacing them with errors biased both low and high.

C. SBB AND NMC NEURAL NETWORKS

The SBB and NMC neural networks perform very similarly. Both overestimate low wind speeds ($< 3 \text{ m/s}$) and underestimate higher wind speeds ($> 11 \text{ m/s}$). Middle wind speeds are biased slightly low. These errors are almost certainly due to the absence of low and high speeds in the training set used to develop the neural networks. Because the original training data set possessed few points in the low and high wind speed regions, the neural networks perform poorly there. Moreover, SBB and NMC neural networks do not currently take into consideration the density of buoy wind speed measurements and assign an appropriate wind speed density distribution weighting factor to the training set.

Both the SBB and NMC neural networks exhibit little variation in performance based upon the amount of atmospheric moisture. The absence of atmospheric moisture-based "crosstalk" of the kind that plagues the regression algorithms provides the neural networks with a significant advantage. Lastly, the NMC neural network, although ostensibly an "all weather network, performed markedly better when filtered through the clear day rain flags established for the CV algorithm, indicating that some form of rain flag is useful even when neural networks are applied.

VI. CONCLUSIONS AND RECOMMENDATIONS

Applied over the global wind speed distribution represented by the combined TOGA and NDBC buoy data set, all four of the wind speed retrieval algorithms examined in this study meet the DMSP requirement that the standard deviation be no greater than ± 2 m/s. Empirically derived regression algorithms, while straightforward and easy to maintain, are significantly affected by the presence of atmospheric moisture. Strictly linear regression algorithms, like CV, fail to accurately model the non-linear dependence of wind speed on brightness temperatures at high moisture levels.

Validation of the CV algorithm over the global wind distribution confirms the problems with performance described by its authors following the validation of the algorithm against predominately mid-latitude buoys. The GSW algorithm mitigates the high bias exhibited by the CV algorithm in high moisture regimes. It does so, however, by eliminating Δ_{37} brightness temperature values less than 31. Data retrieved through a water laden atmosphere, however, are equally as important as data retrieved under cloudy conditions. The variation in performance between the CV and GSW algorithms highlights the central problem with algorithms that are significantly affected by atmospheric moisture. Namely, that attempts to improve algorithm performance are necessarily dependent upon excluding or modifying values retrieved under high moisture conditions. For this reason, among others, neural network-based algorithms appear to hold greater promise for broad-based effectiveness than do regression algorithms.

Both the SBB and NMC neural network perform equally well across the full range of water vapor values. Neural network values retrieved under lower Δ_{37} values are less accurate than those retrieved under "clear" conditions. The error generated by the SBB neural network during cloudy conditions is greater than that retrieved during clear conditions by up to 3 m/s. Though designed as an "all weather" algorithm, the NMC neural network performance is enhanced when its data are filtered through the CV rain flag used to segregate clear weather conditions. Neural networks perform best where the wind speed

density distribution is the greatest.

To achieve the greatest wind speed retrieval accuracy across the broadest possible wind speed range, it is recommended that the authors of the respective neural networks develop revised training data sets that represent the full distribution of global winds. Increased representation of low and high speed winds in the training data set will help eliminate the bias generated by the neural networks in those regions. Alternatively, it should be possible to accurately retrieve winds in all regions by employing a combination of regression and artificial intelligence techniques. Neural networks may be used when regression algorithms begin to fail due to high atmospheric moisture content.

APPENDIX A: FIGURES

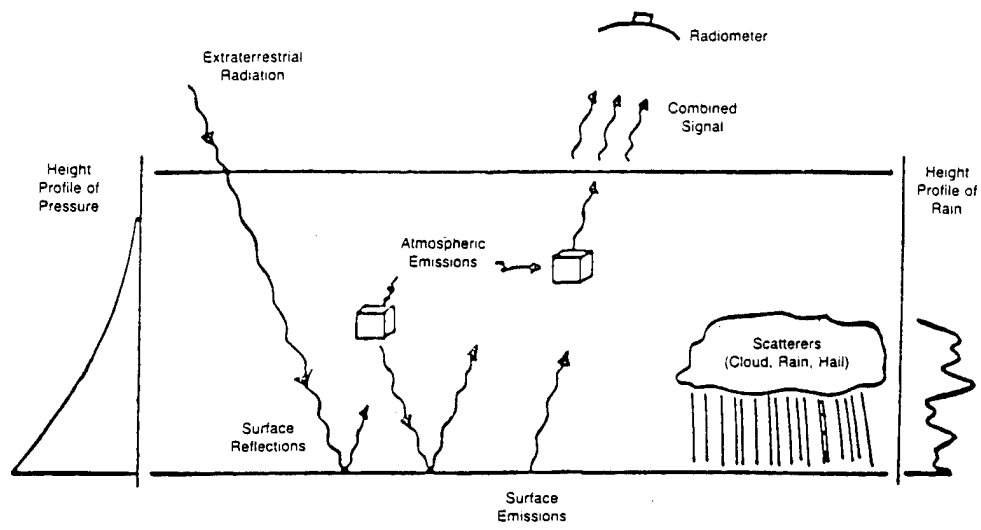


Figure 1: Sources of Thermal Radiation, From [Swift, 1990]

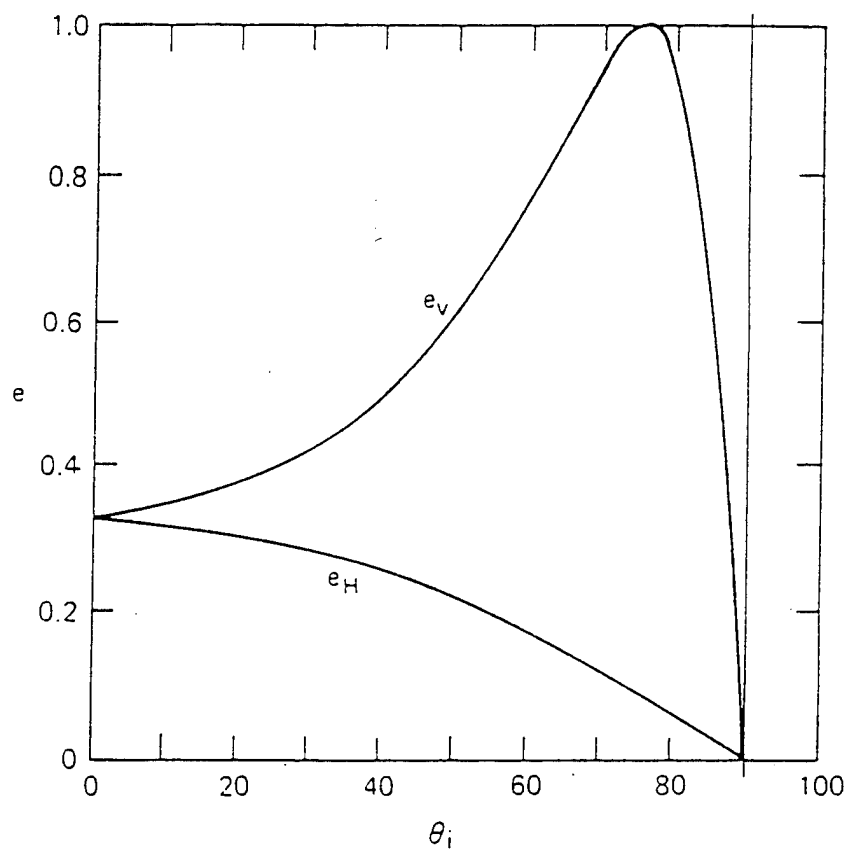


Figure 2: Incidence Angle Polarization Effects, From [Swift, 1990]

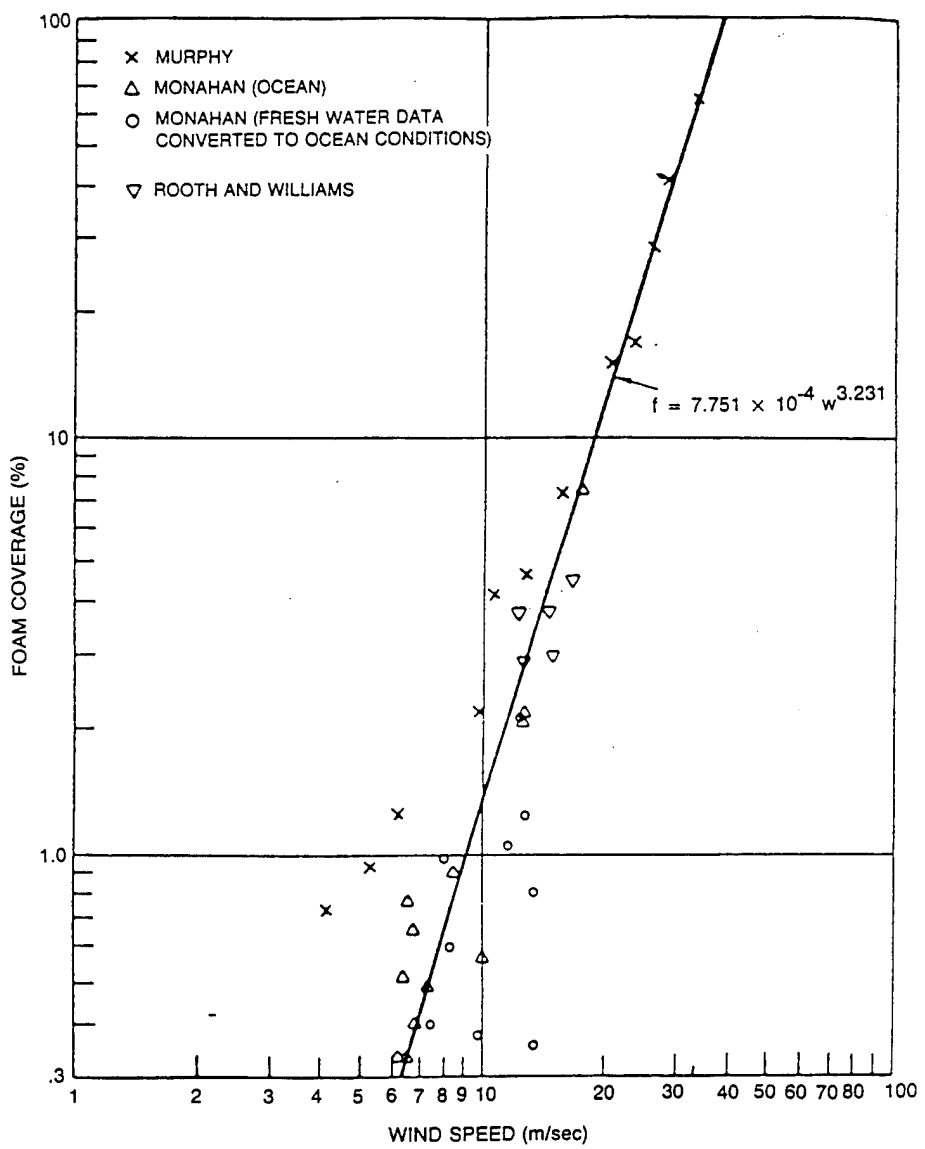


Figure 3: Foam Coverage, From [Swift, 1990]

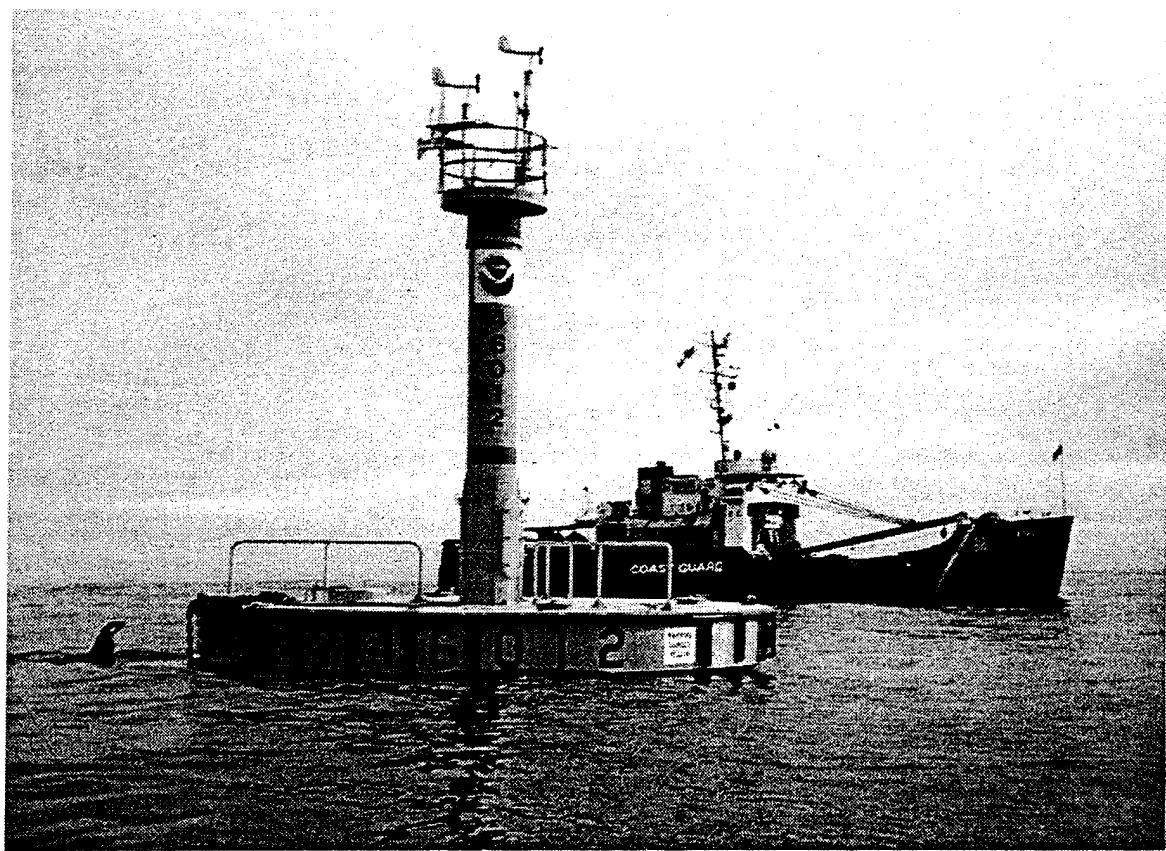


Figure 4: NDBC 10-meter Discus Buoy, From [NOAA, 1995]

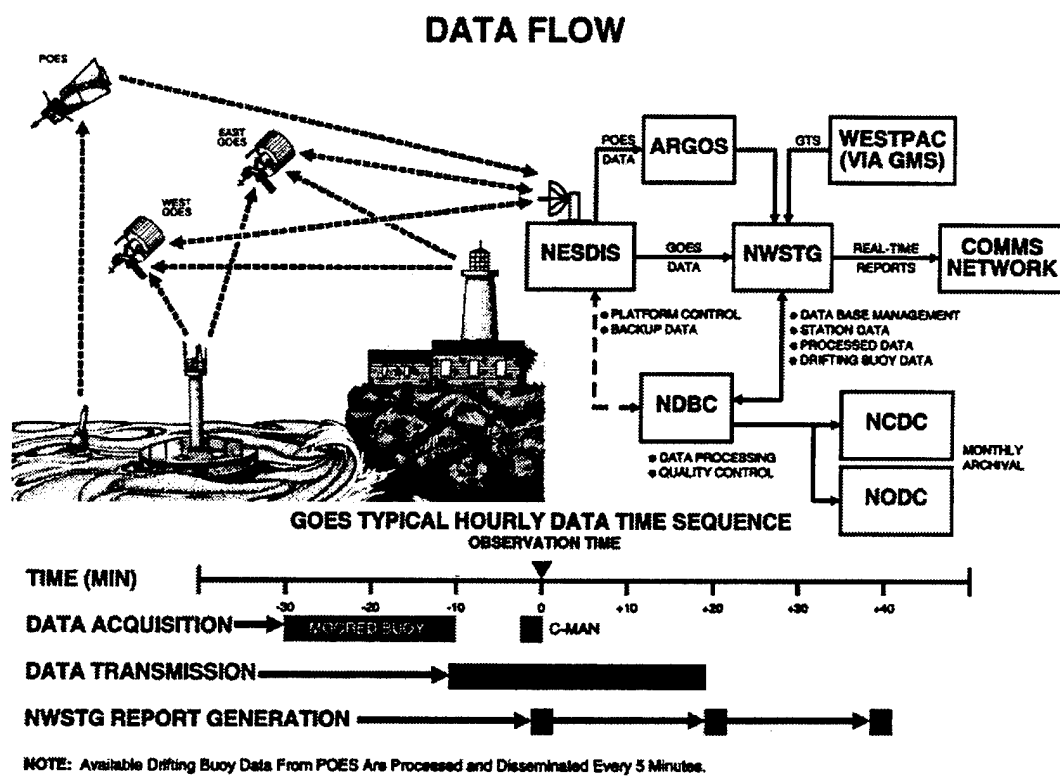


Figure 5: NDBC Buoy Data Flow Path, From [NOAA, 1995]

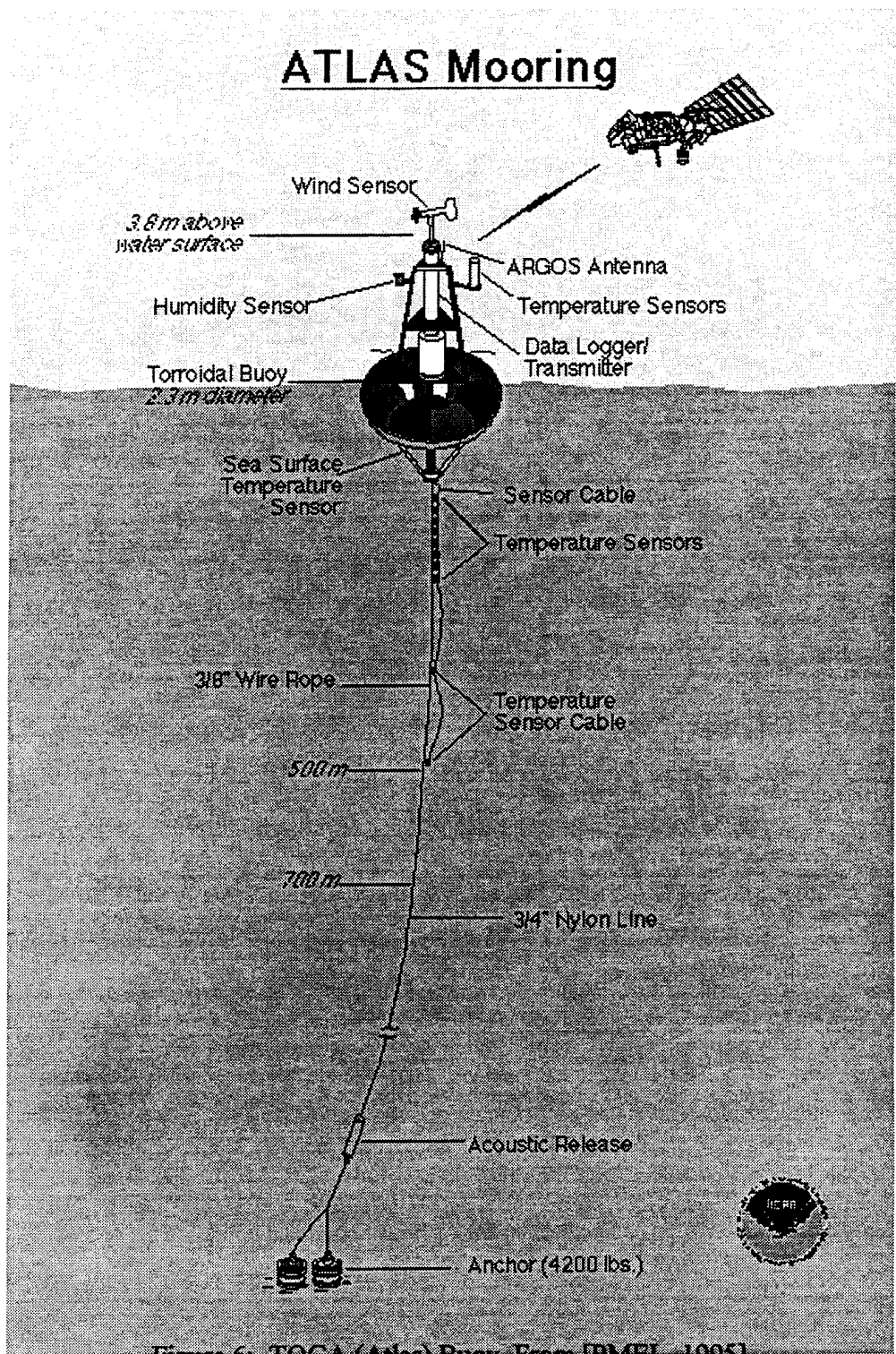


Figure 6: TOGA (Atlas) Buoy, From [PMEL, 1995]

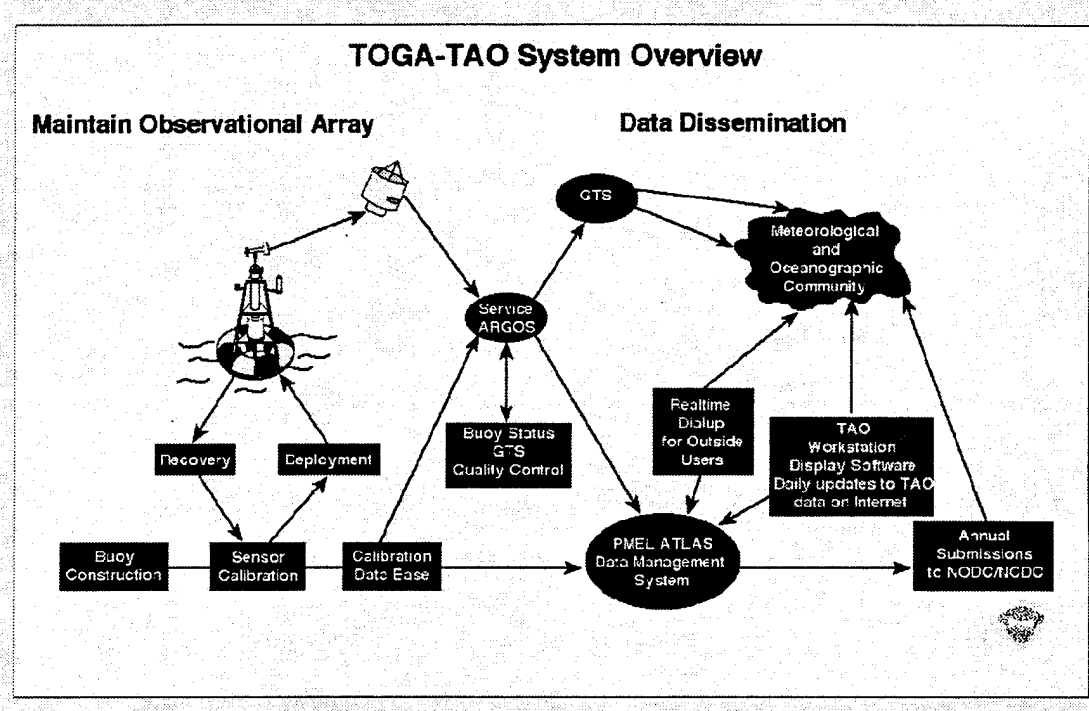


Figure 7: TOGA Buoy Data Flow Path, From [PMEL, 1995]

SSM/I SENSOR

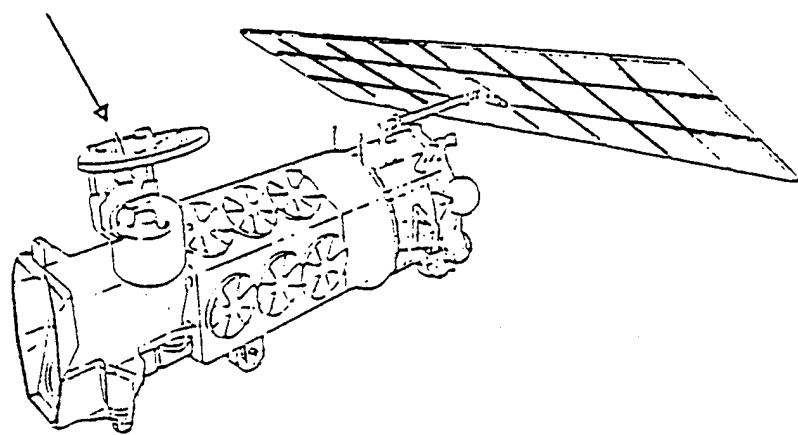


Figure 8: SSM/I on DMSP Satellite (Deployed Position), From [Hollinger et al., 1987]

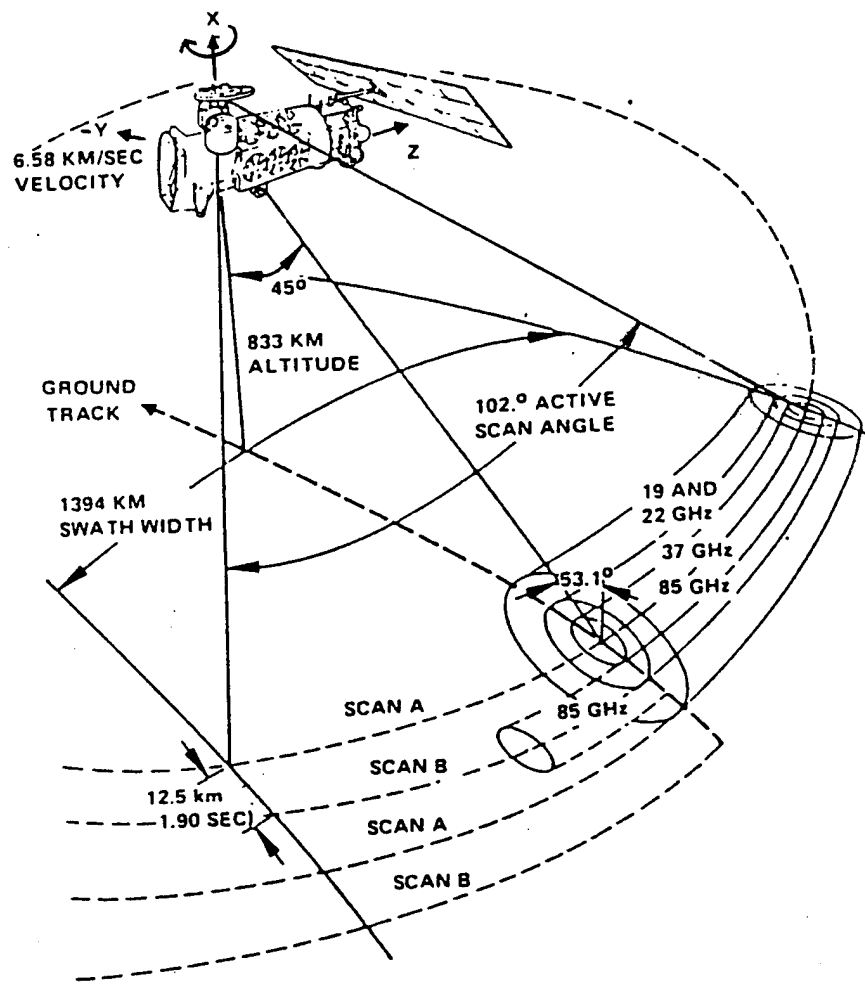


Figure 9: Instantaneous Field of View, From [Hollinger et al., 1987]

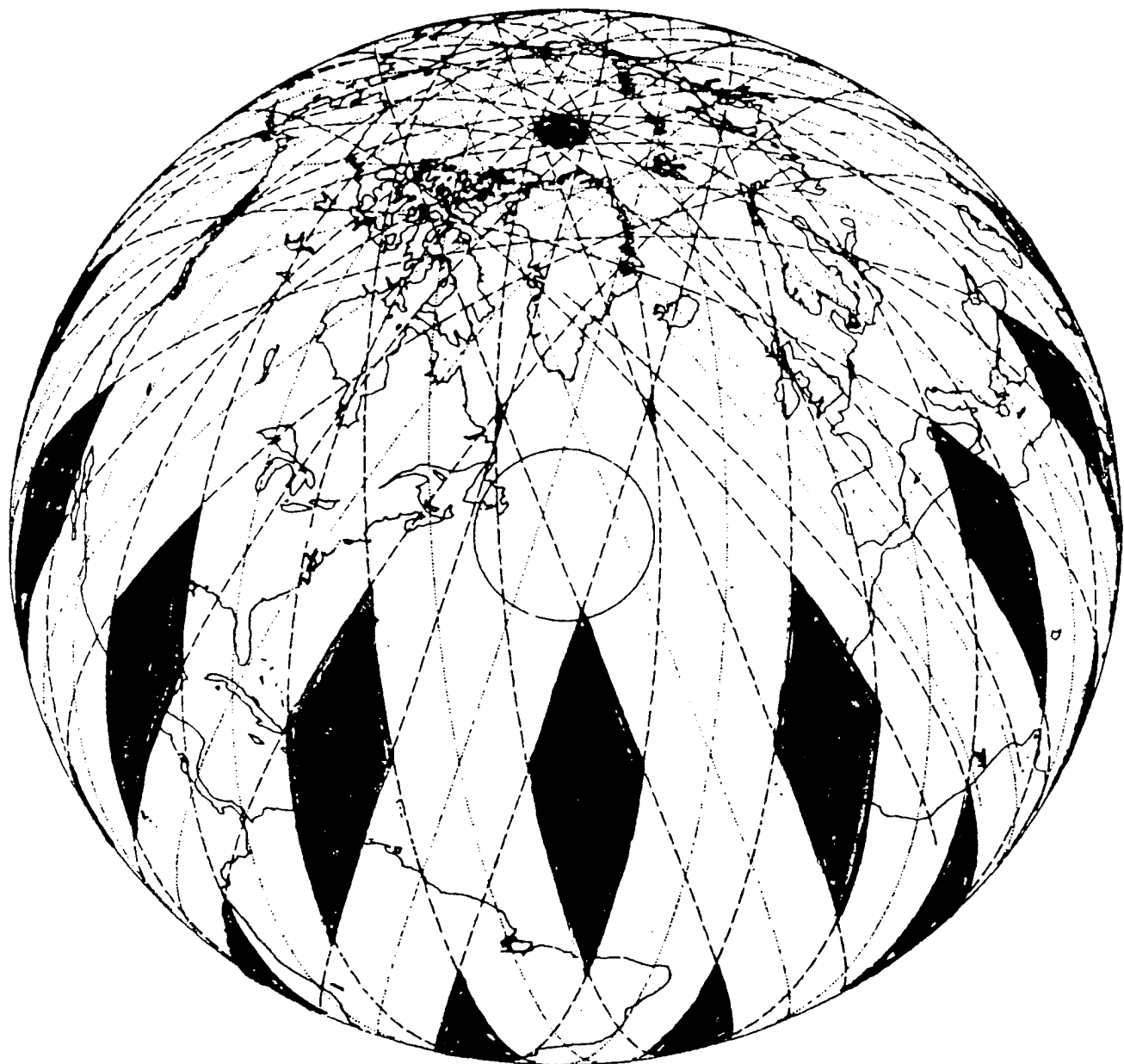


Figure 10: SSM/I Successive Orbits, From [Hollinger, 1987]

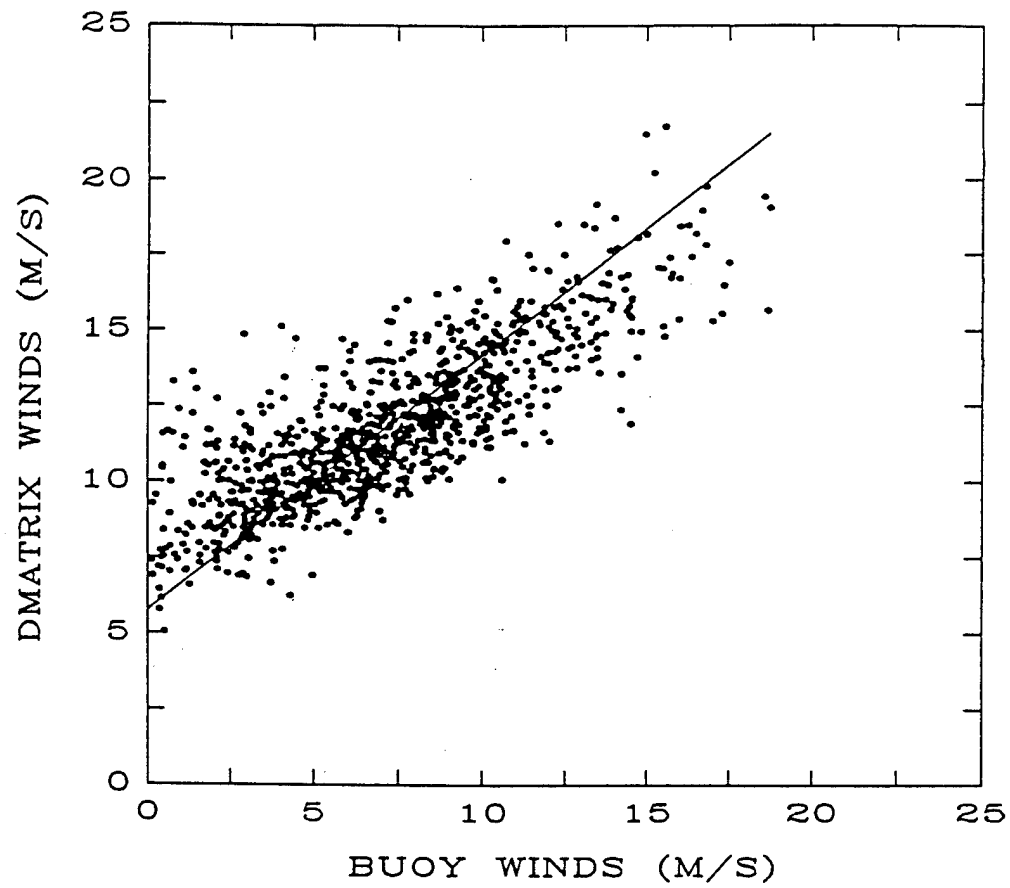


Figure 11: D-matrix Wind Speeds, From [Hollinger, 1991]

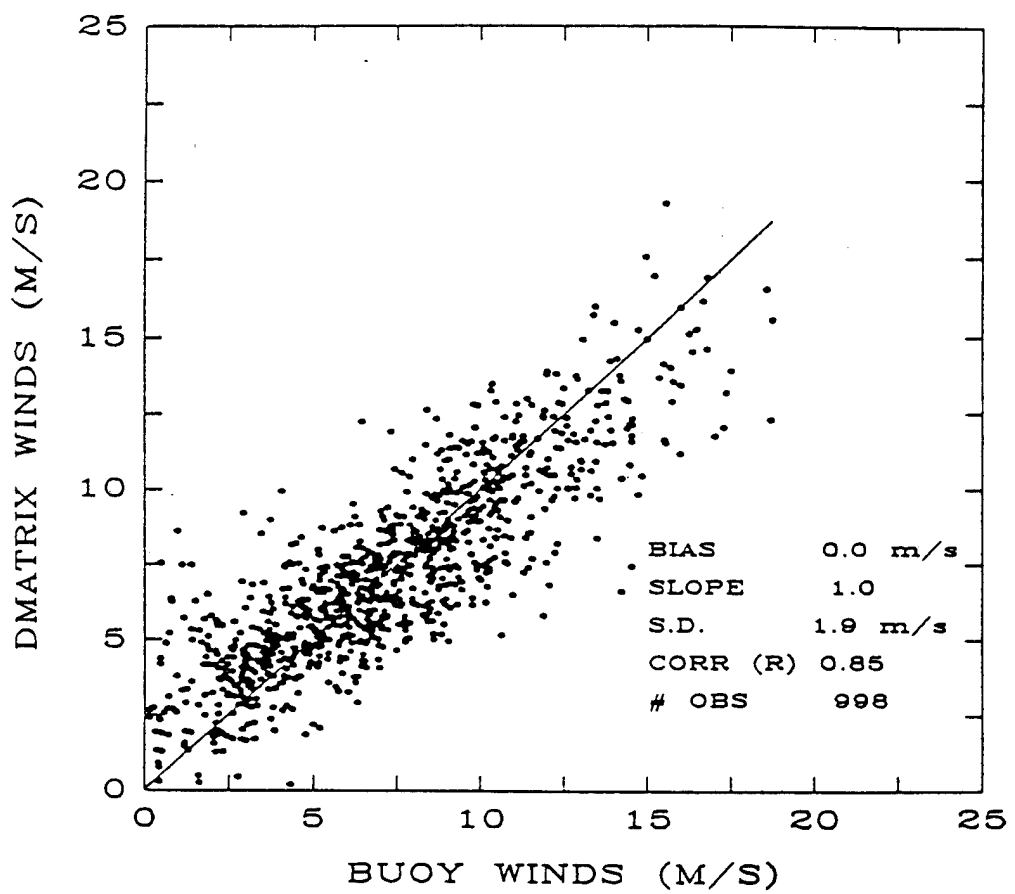


Figure 12: D-matrix Wind Speeds, From [Hollinger, 1991]

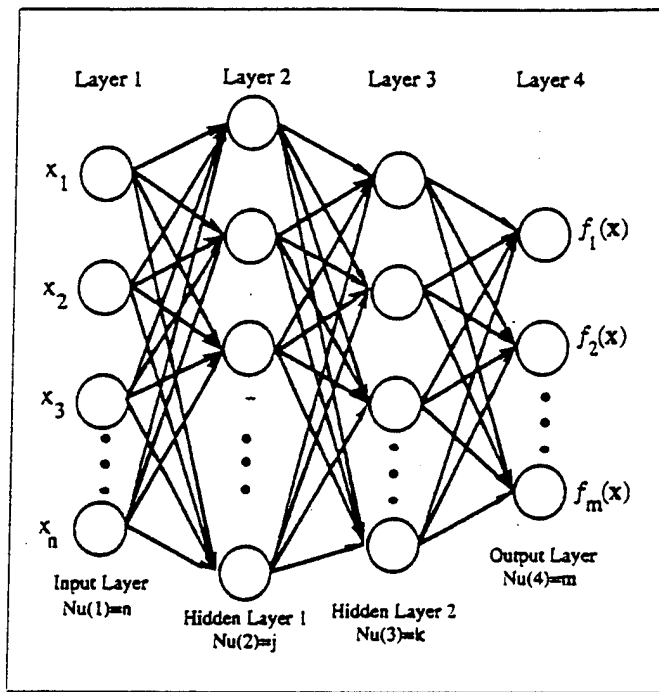


Figure 13: Topology of a Multi-Layer Feed-Forward Neural Network, From [Dawson, 1993]

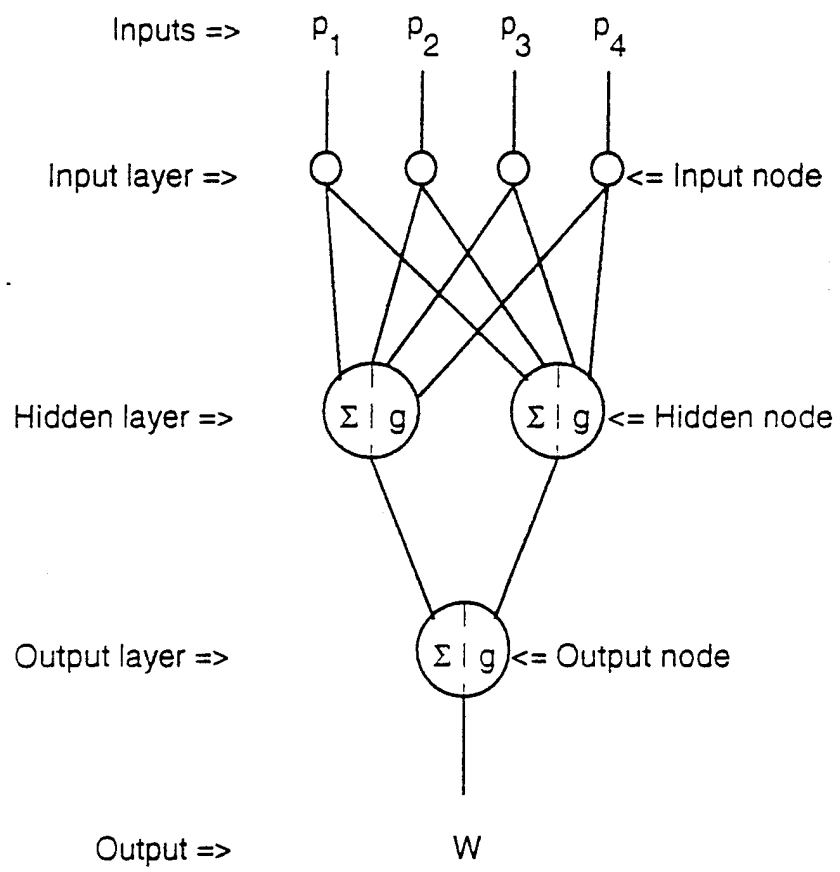
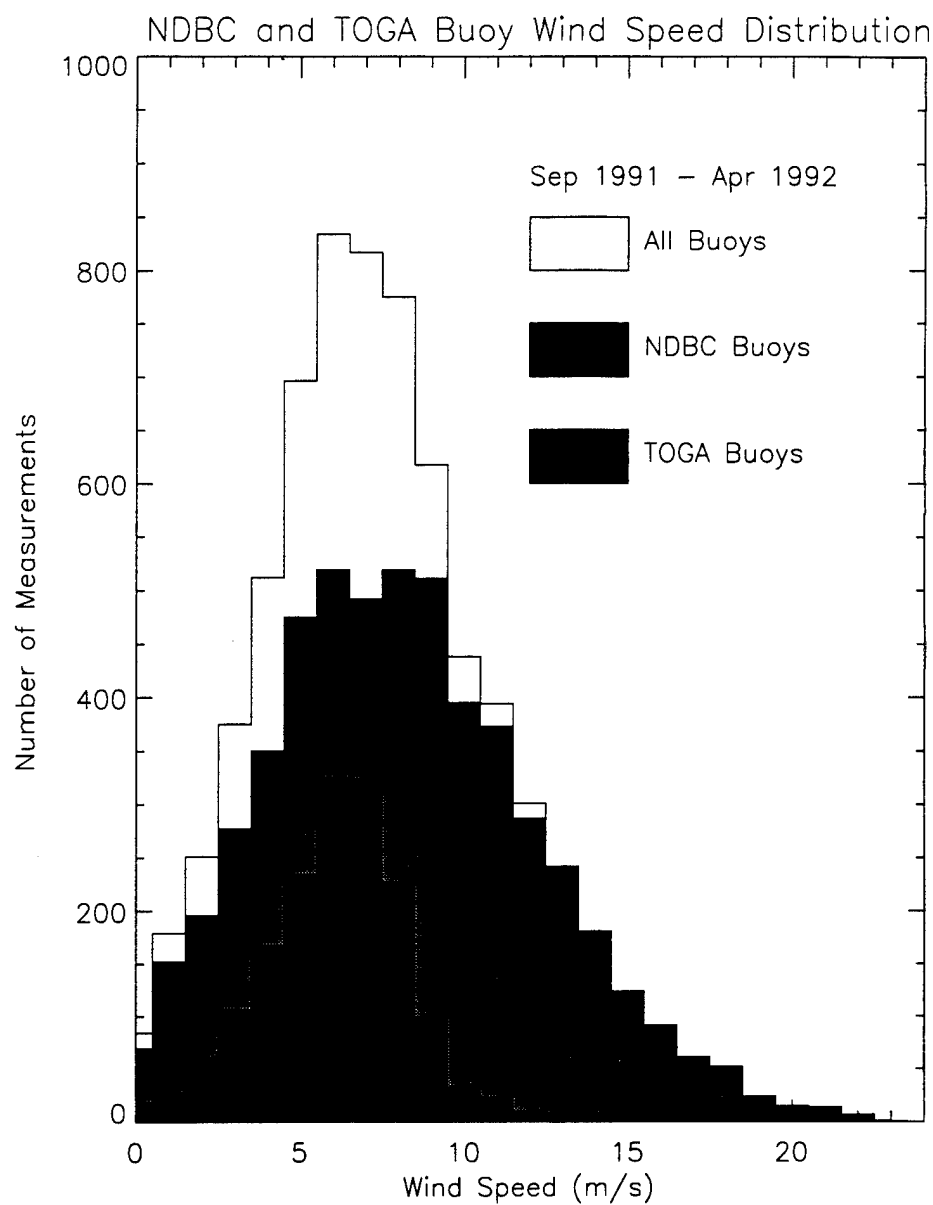
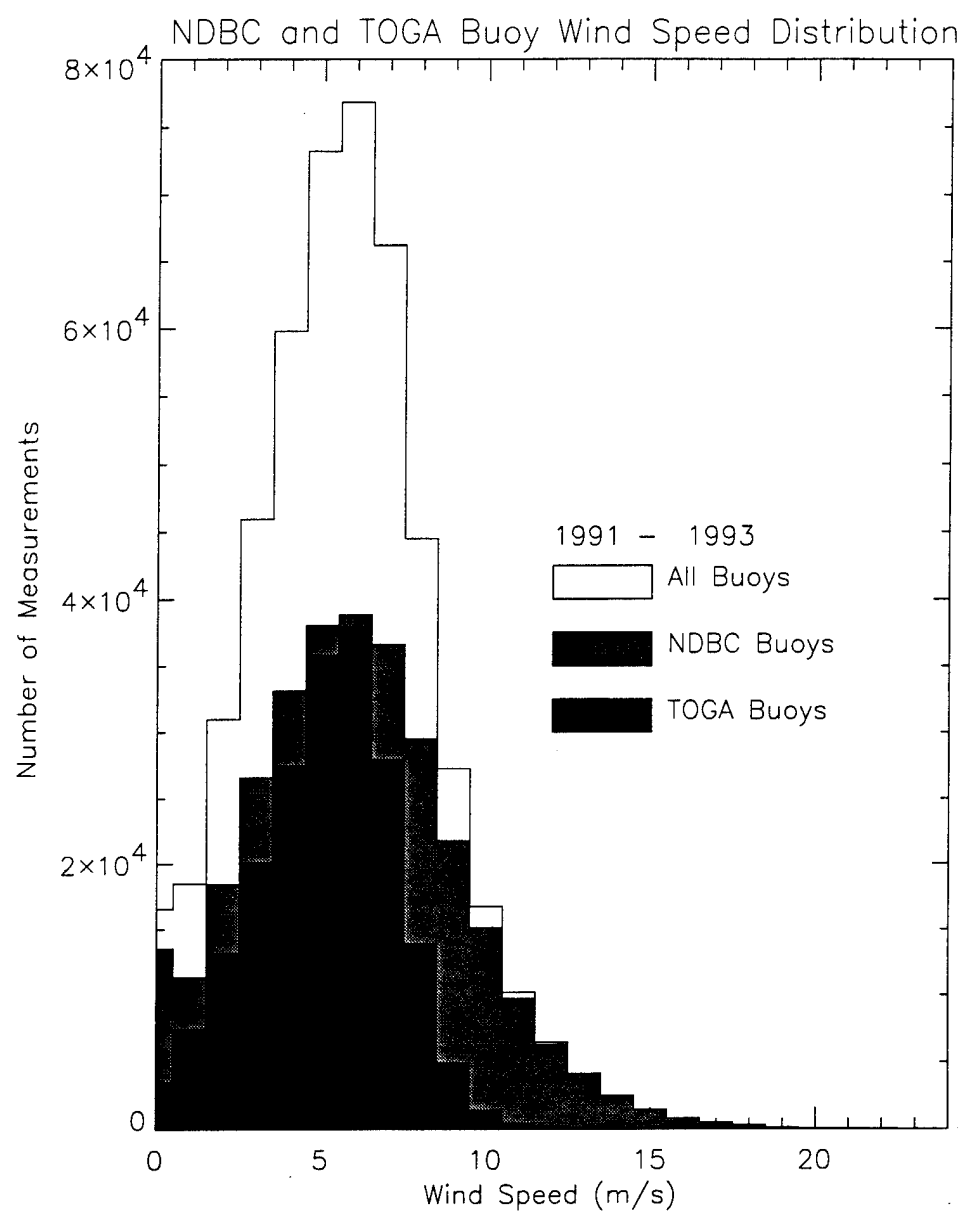


Figure 14: Neural Network Architecture used by SBB and NMC, From [Krasnopolksy, 1994]



Naval Postgraduate School – Run on: 4-Mar-1995

Figure 15: NDBC and TOGA Wind Speed Distribution



Naval Postgraduate School – Run on: 25-May-1995

Figure 16: NDBC and TOGA Wind Speed Distribution (2-Year Period)

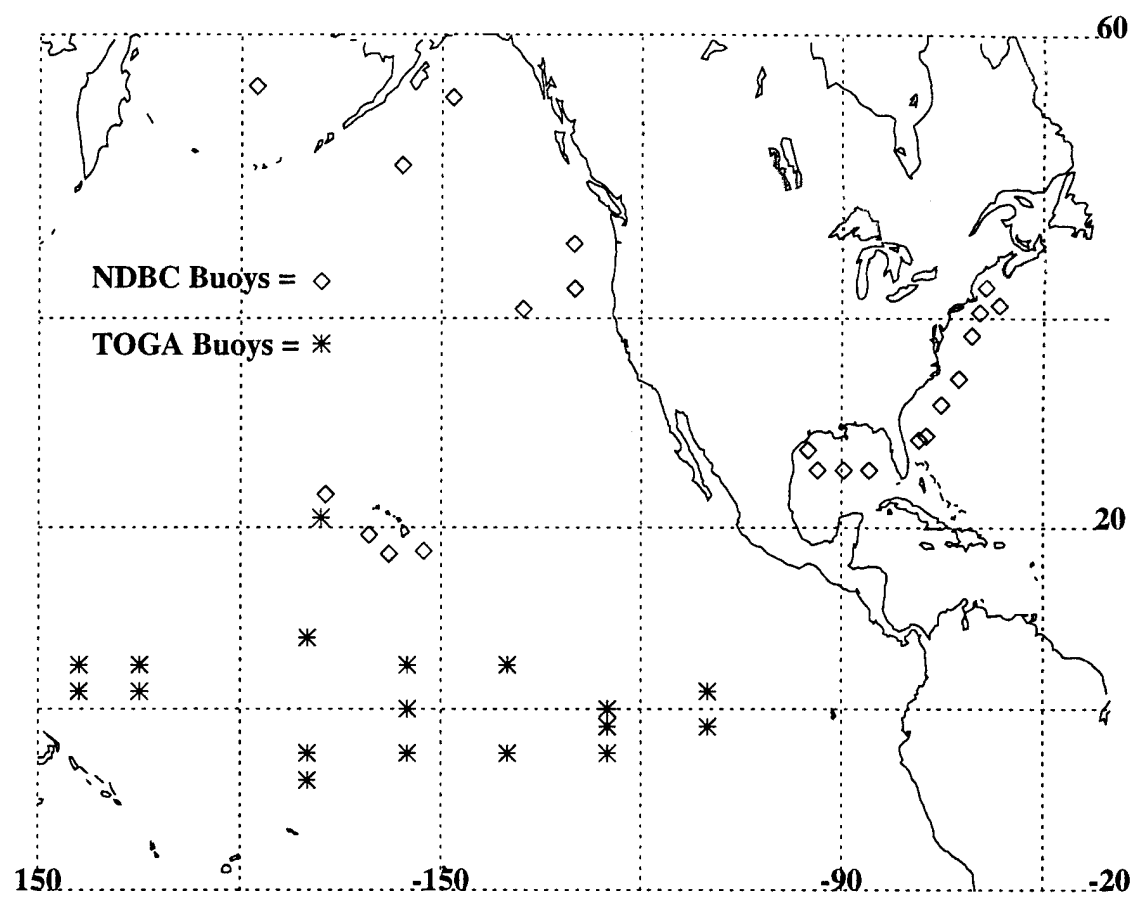
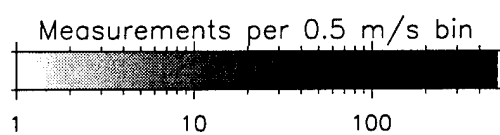
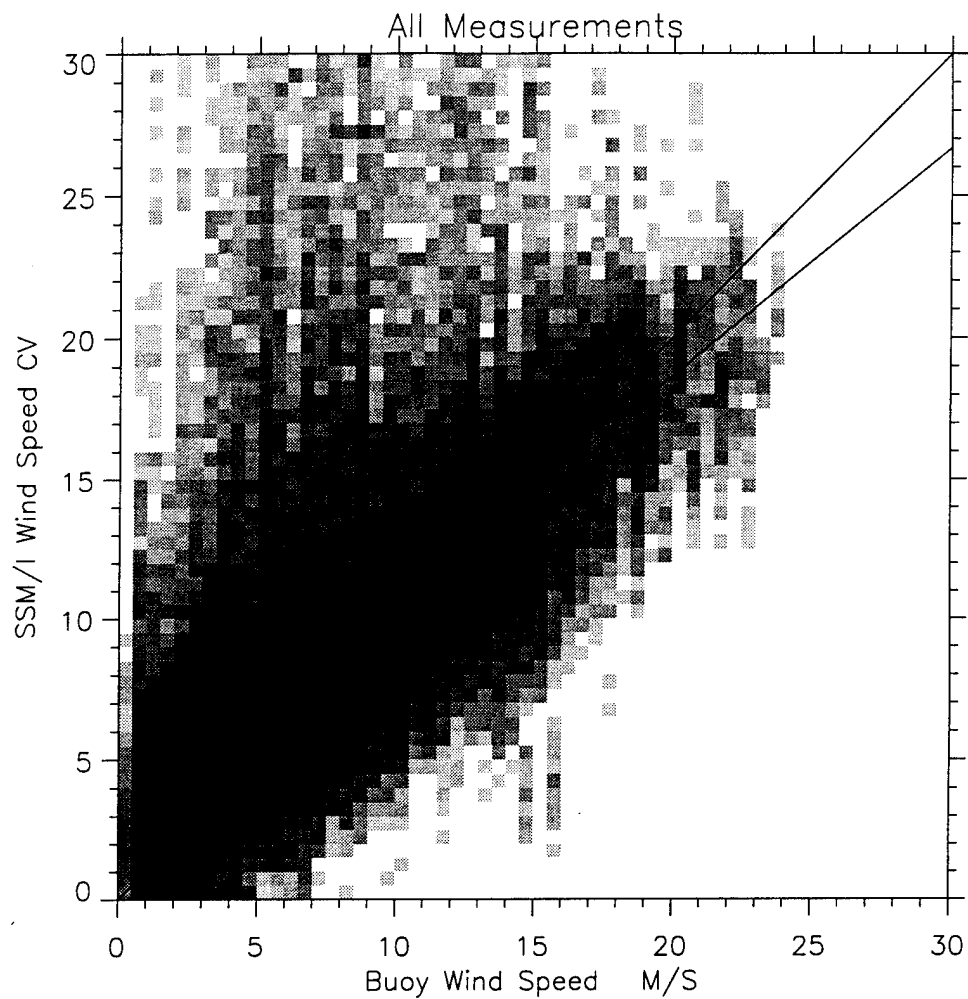
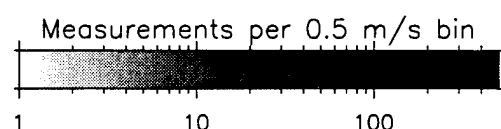
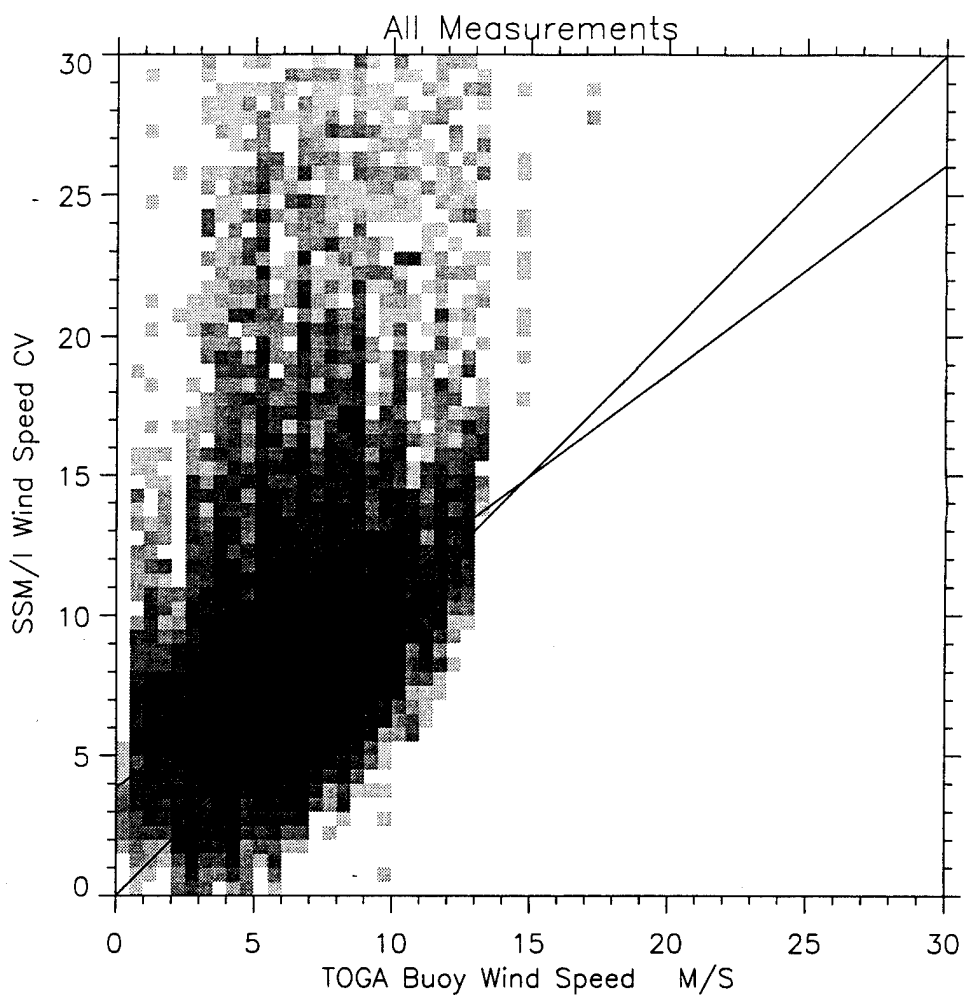


Figure 17: Location of TOGA and NDBC Buoys



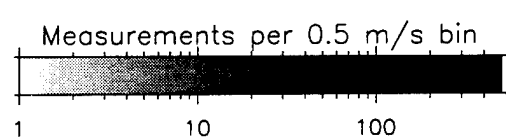
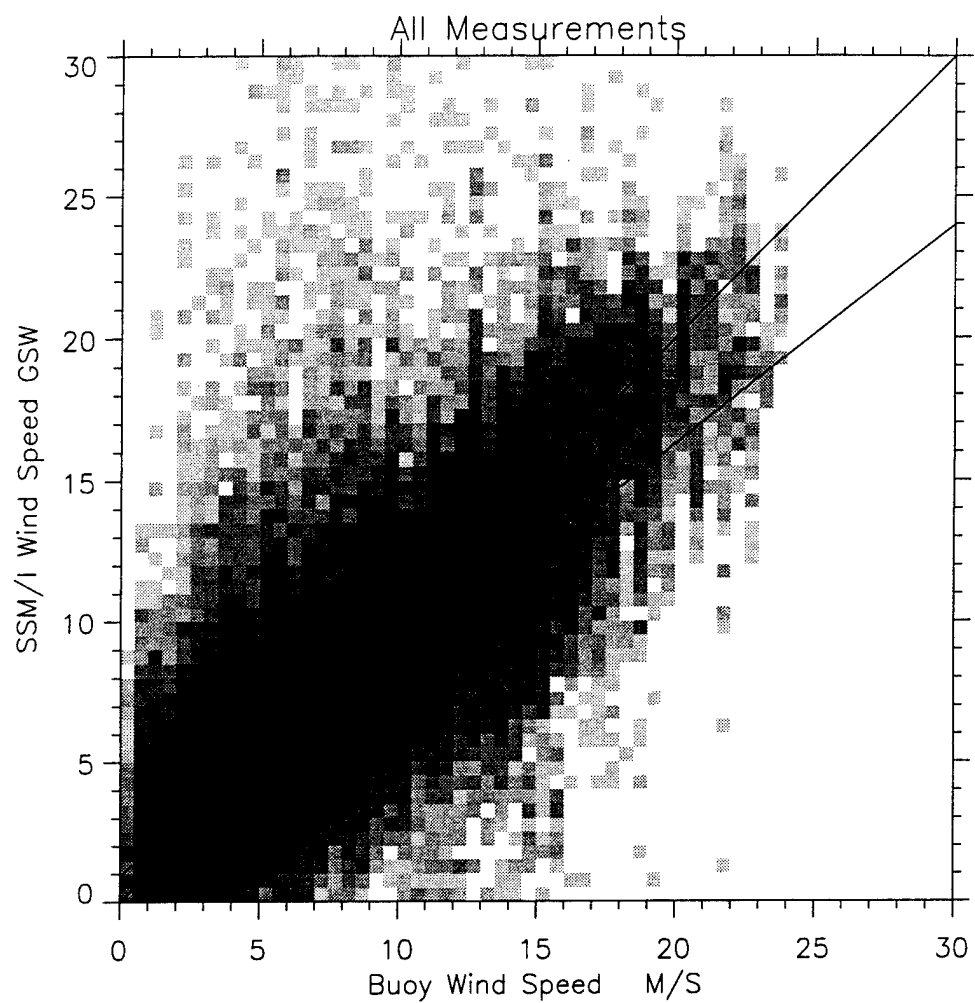
Naval Postgraduate School - Run /Global/gscall_unf run on tall.unf and null.unf - 30-Mar-1995

Figure 18: All CV Wind Speed Data vs Buoy Wind Speed



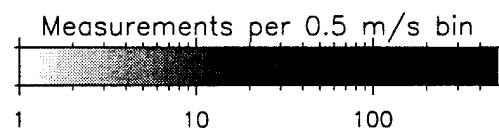
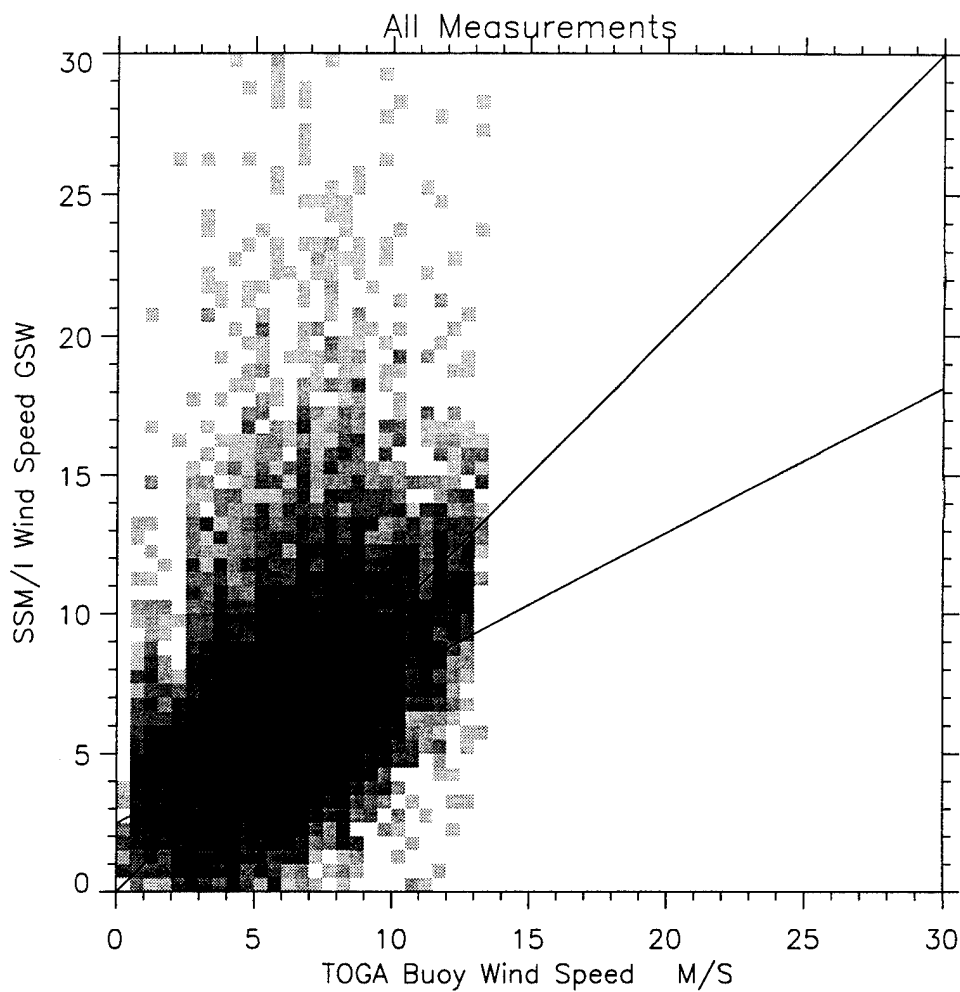
Naval Postgraduate School - Run /Toga/tscall.unf run on tall.unf - 30-Mar-1995

Figure 19: CV Wind Speed vs TOGA Buoy Wind Speed



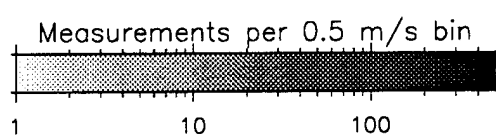
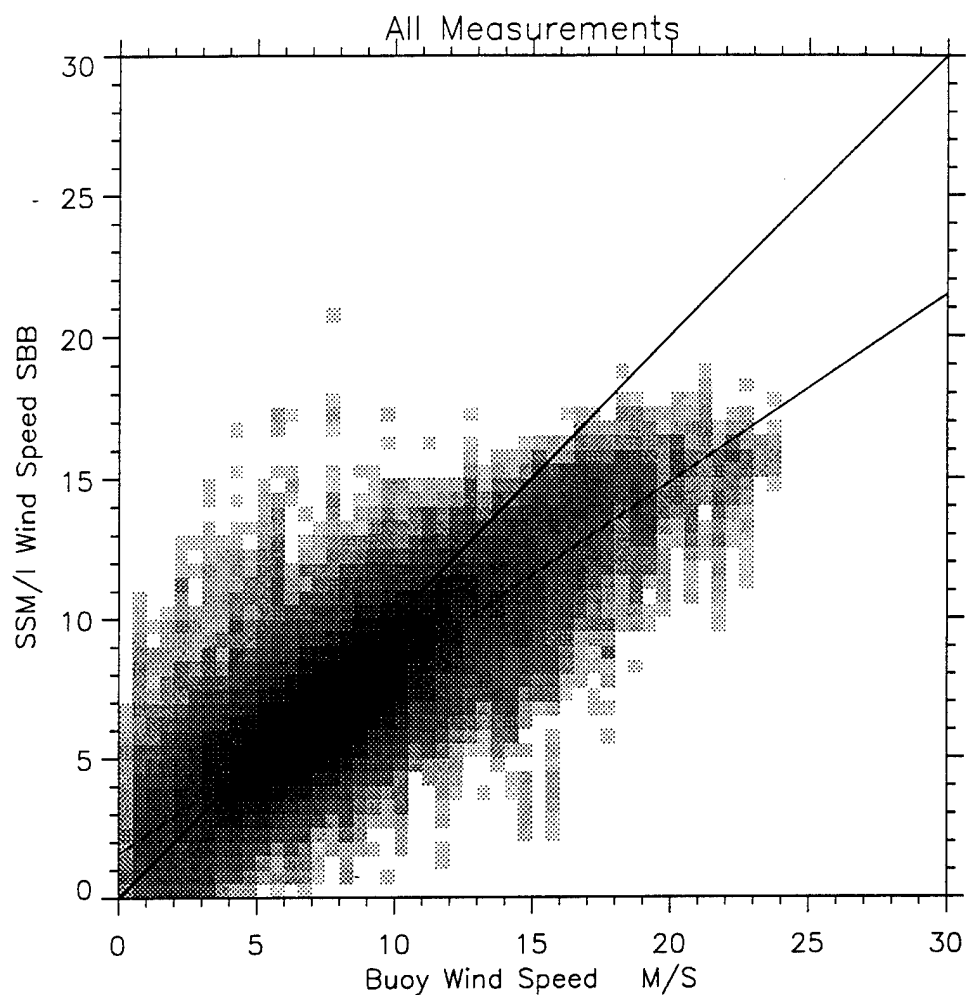
Naval Postgraduate School - Run /Global/gscall.unf run on tall.unf and null.unf - 29-Mar-1995

Figure 20: All GSW Wind Speed Data vs Buoy Wind Speed



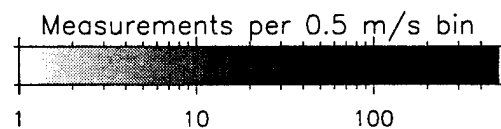
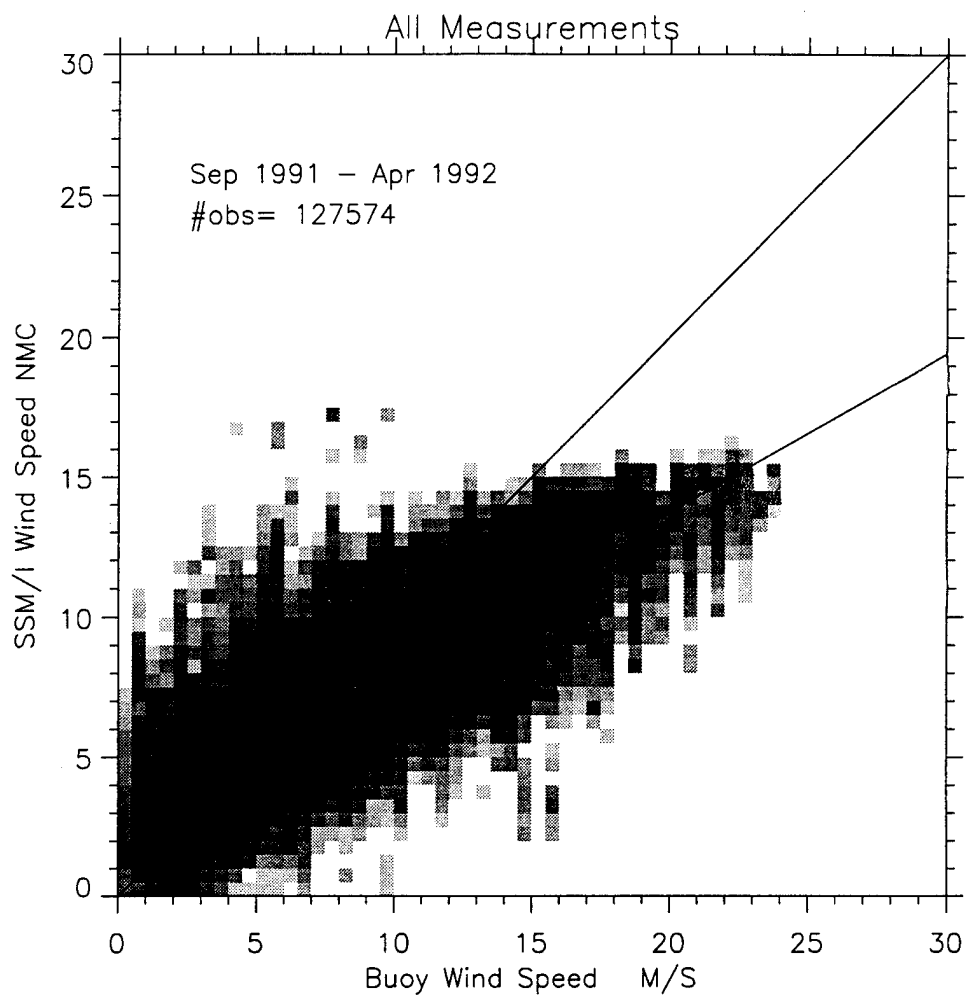
Naval Postgraduate School ~ Run /Toga/tscall_unf run on tall.unf ~ 30-Mar-1995

Figure 21: GSW Wind Speed vs TOGA Buoy Wind Speed



Naval Postgraduate School - Run /Global/gscall_unf run on tall.unf and null.unf - 31-May-1995

Figure 22: All SBB Wind Speed Data vs Buoy Wind Speed



Naval Postgraduate School – Run /Global/gsceil_unf run on tall.unf and nall.unf – 30-Mar-1995

Figure 23: All NMC Wind Speed Data vs Buoy Wind Speed

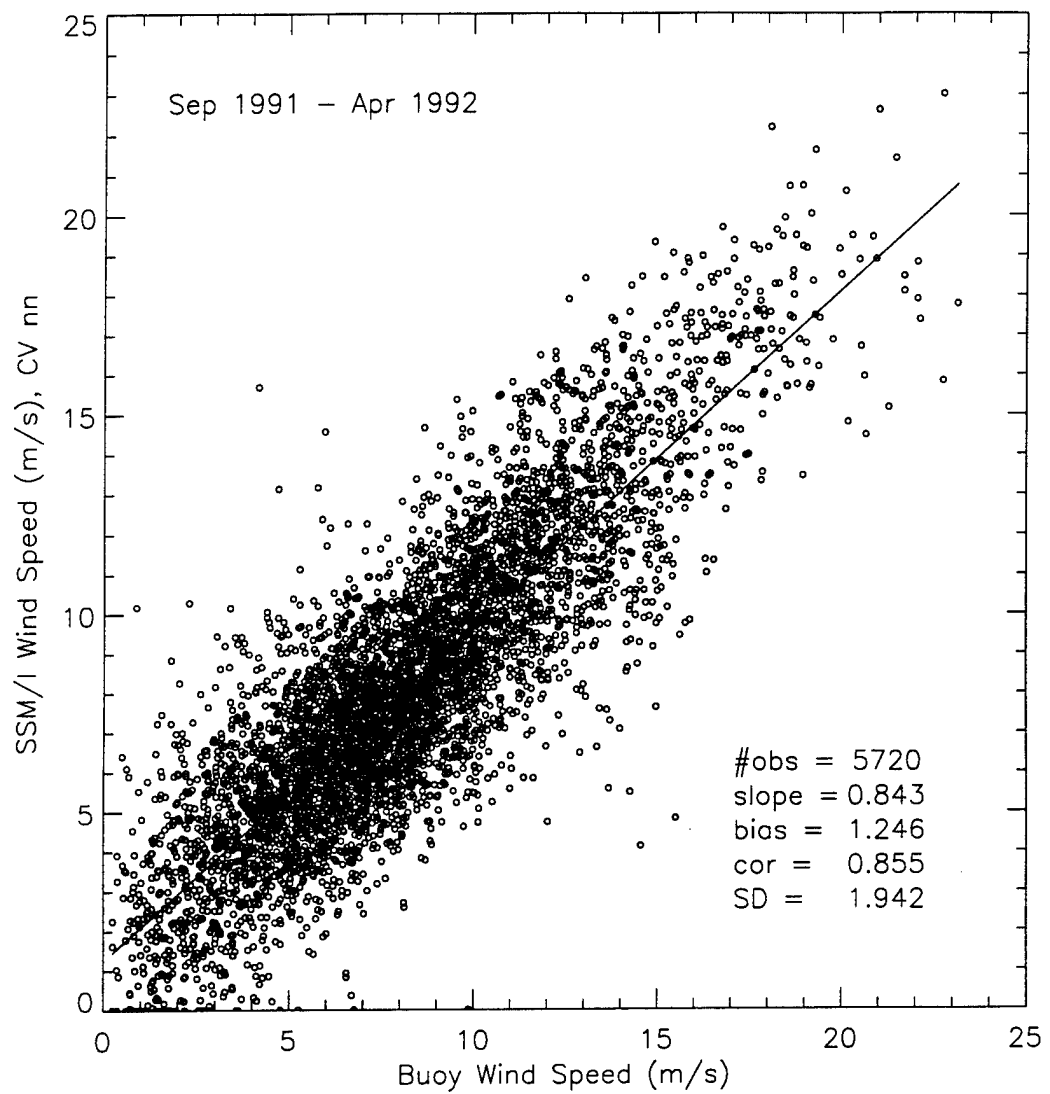


Figure 24: CV Nearest Neighbor Wind Speed vs Buoy Wind Speed, Rain Flag 0

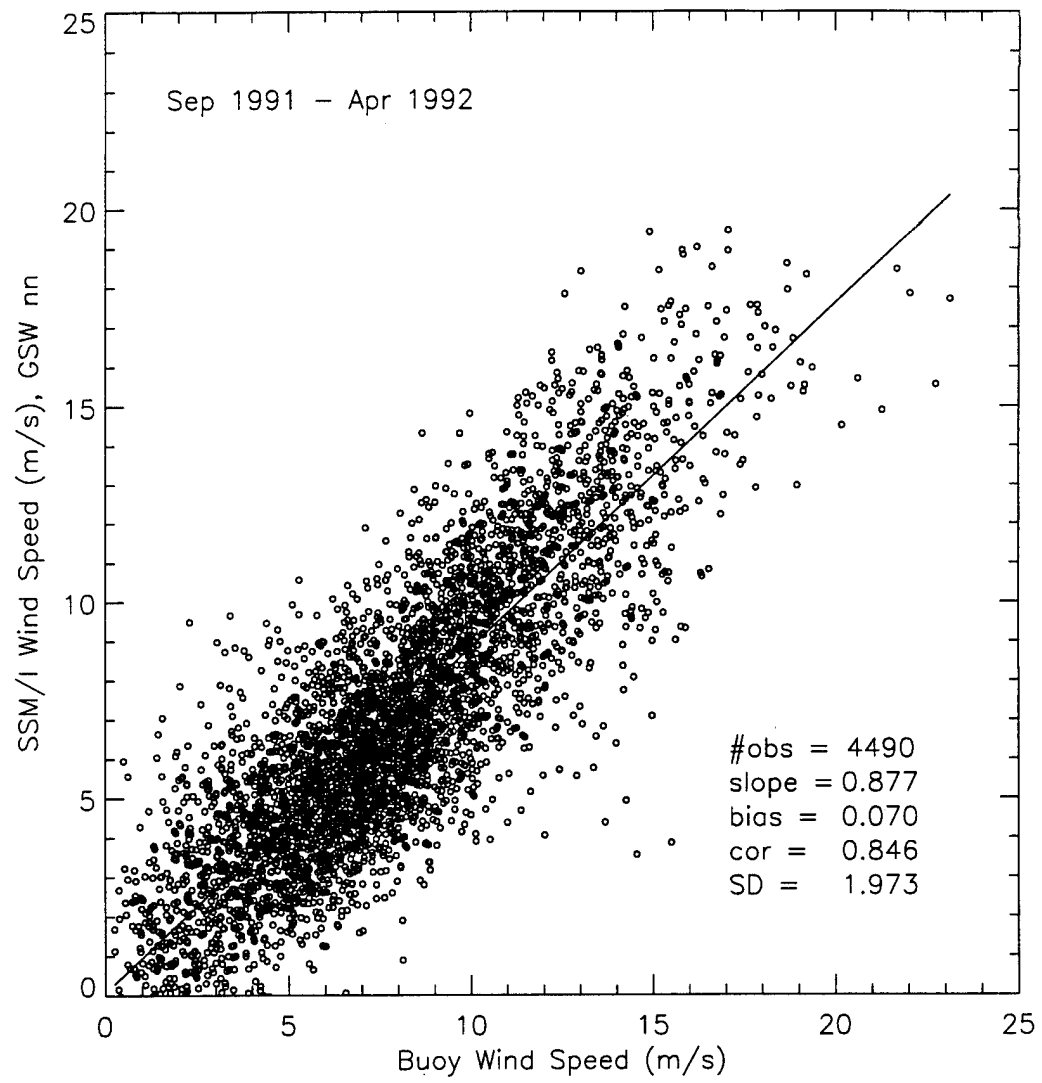


Figure 25: GSW Nearest Neighbor Wind Speed vs Buoy Wind Speed, Rain Flag 0

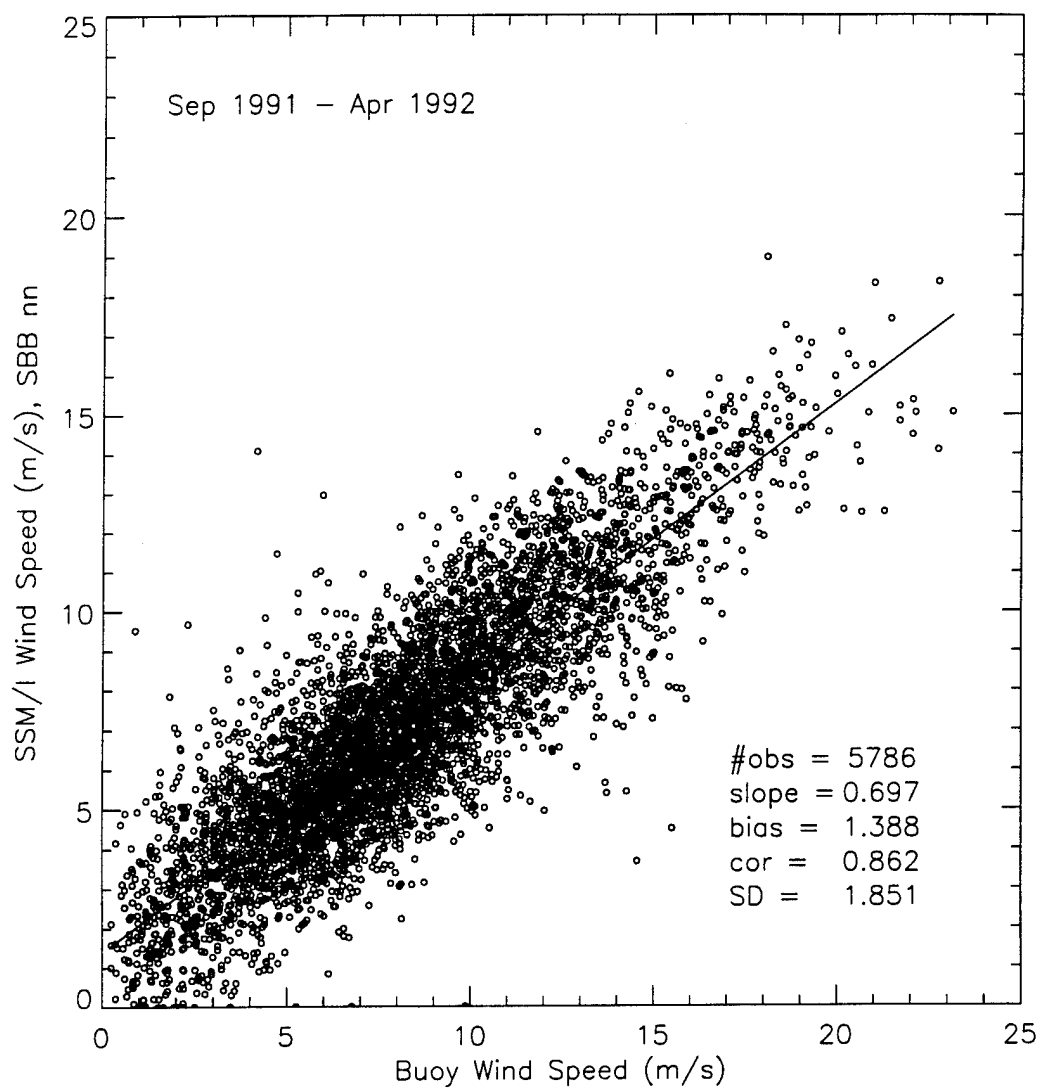


Figure 26: SBB Nearest Neighbor Wind Speed vs Buoy Wind Speed, Rain Flag 0

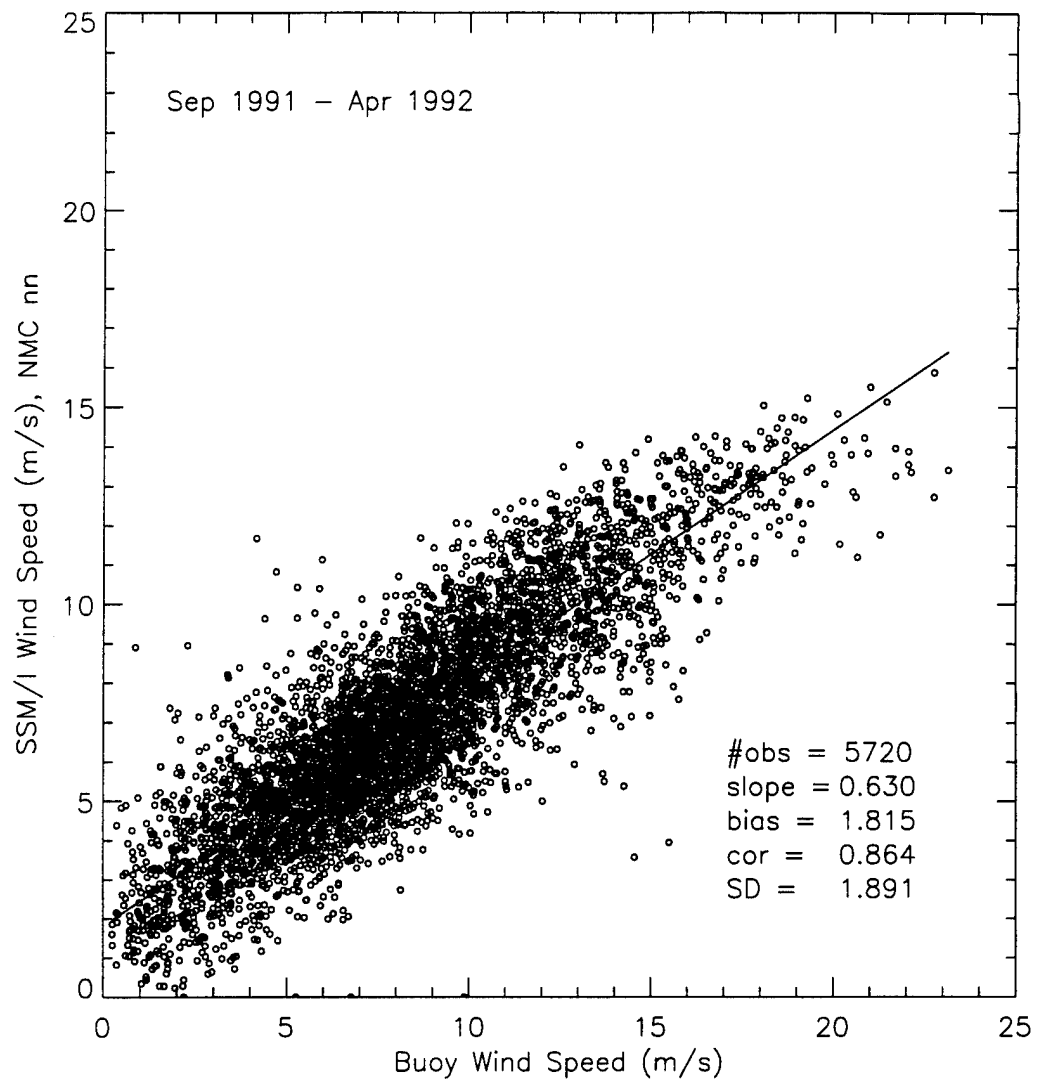
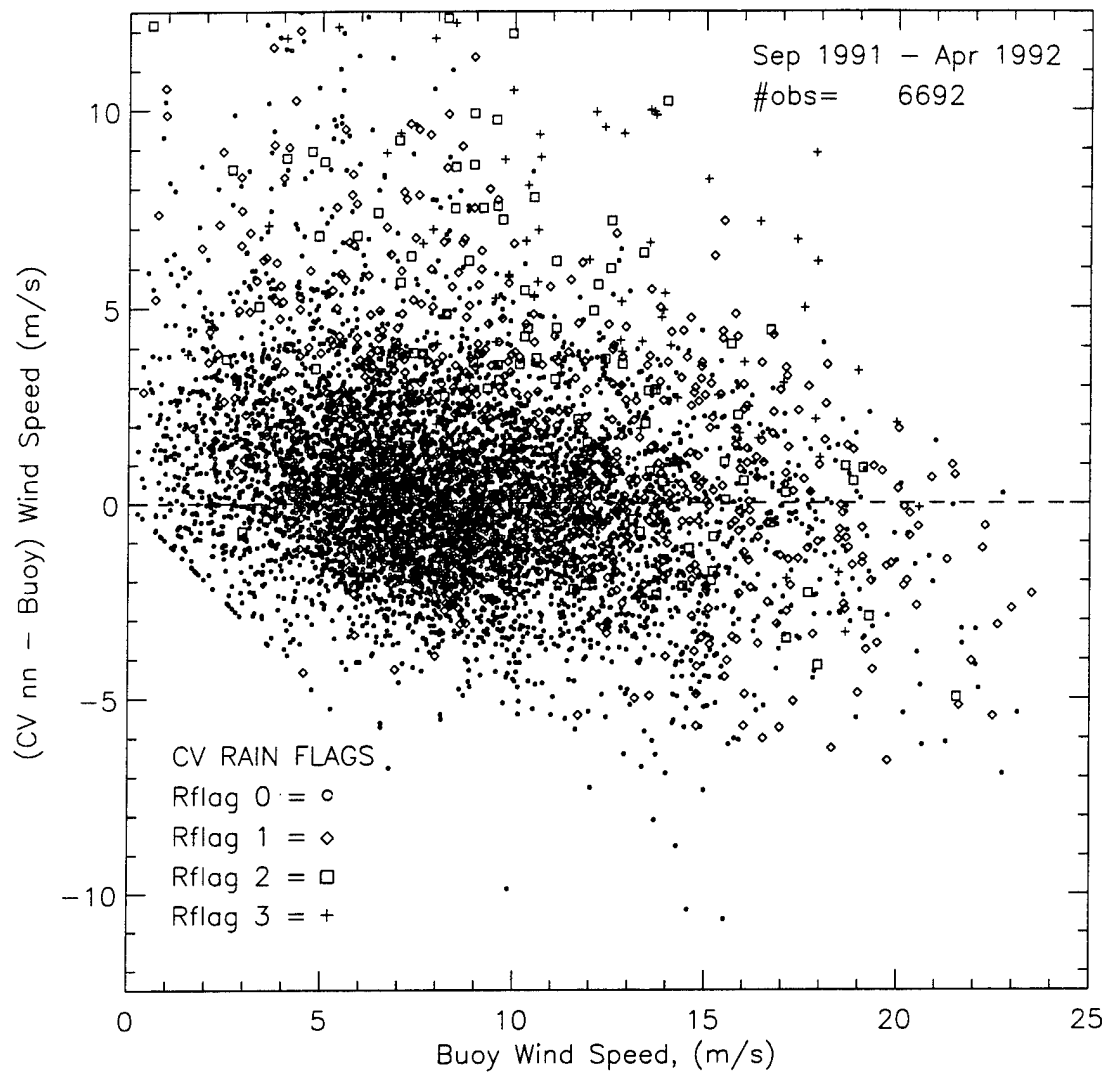
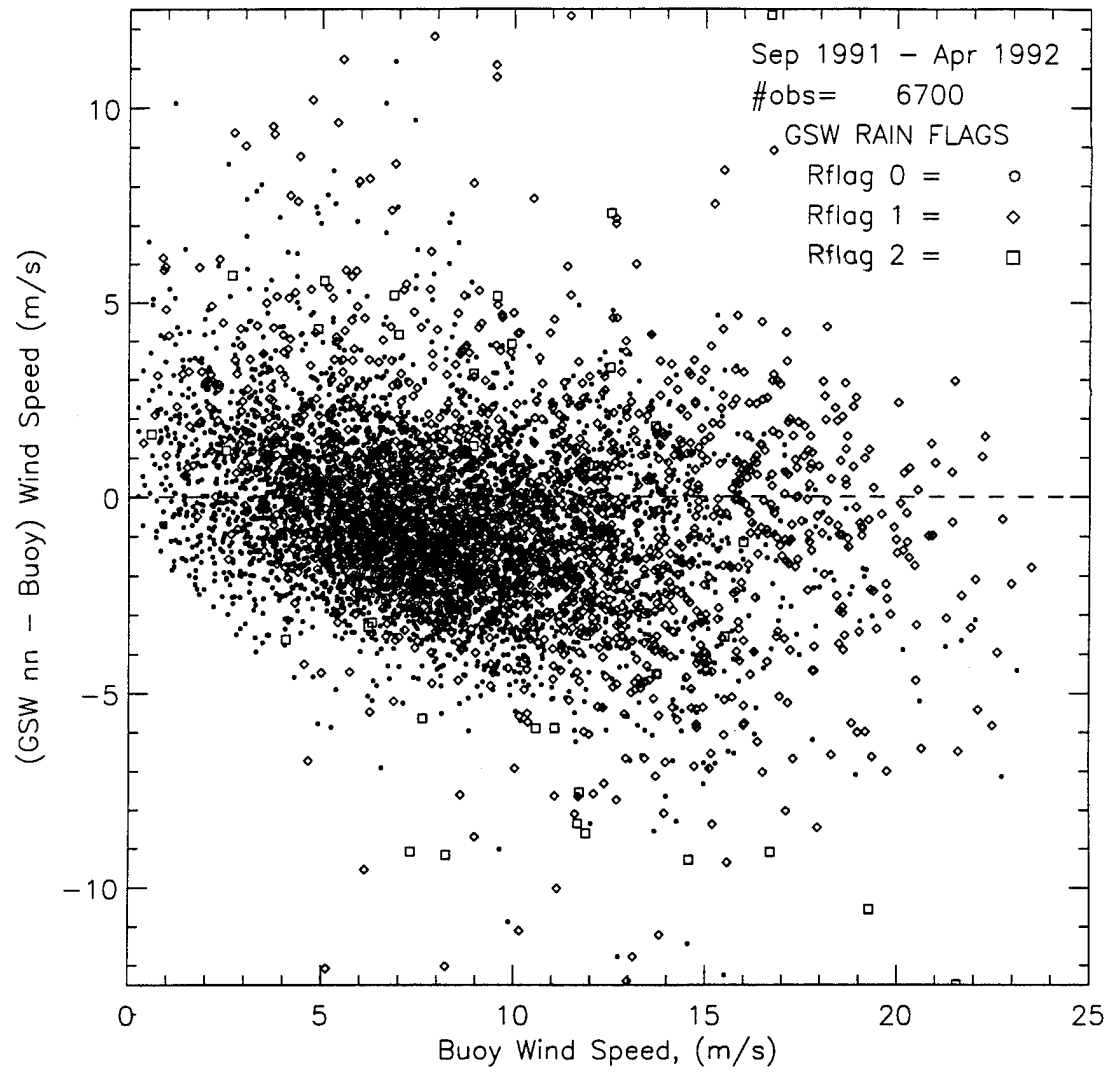


Figure 27: NMC Nearest Neighbor Wind Speed vs Buoy Wind Speed, CV Rain Flag 0



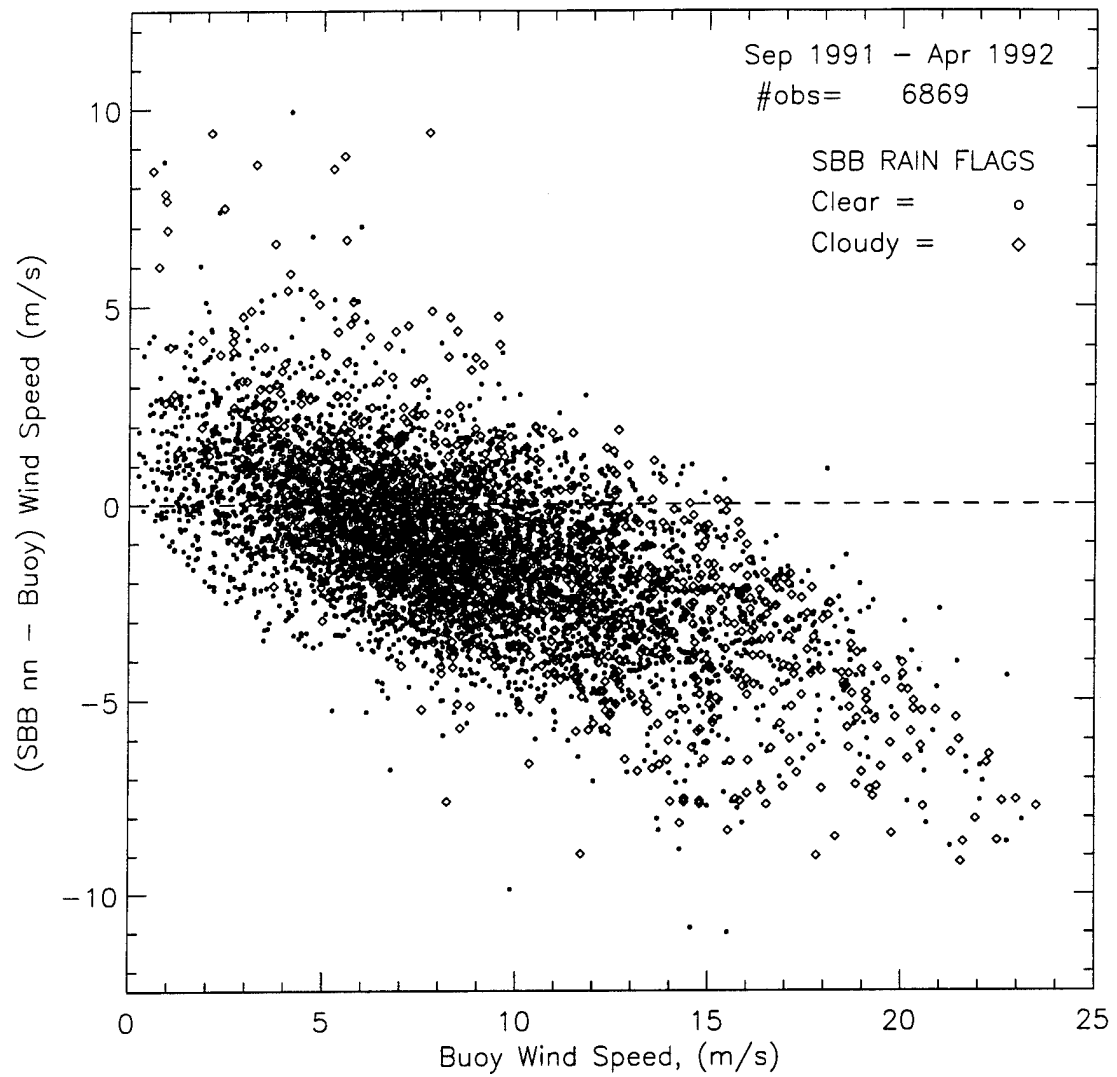
Naval Postgraduate School – Run on 5-Apr-1995

Figure 28: (CV Nearest Neighbor - Buoy) Wind Speed vs Buoy Wind Speed



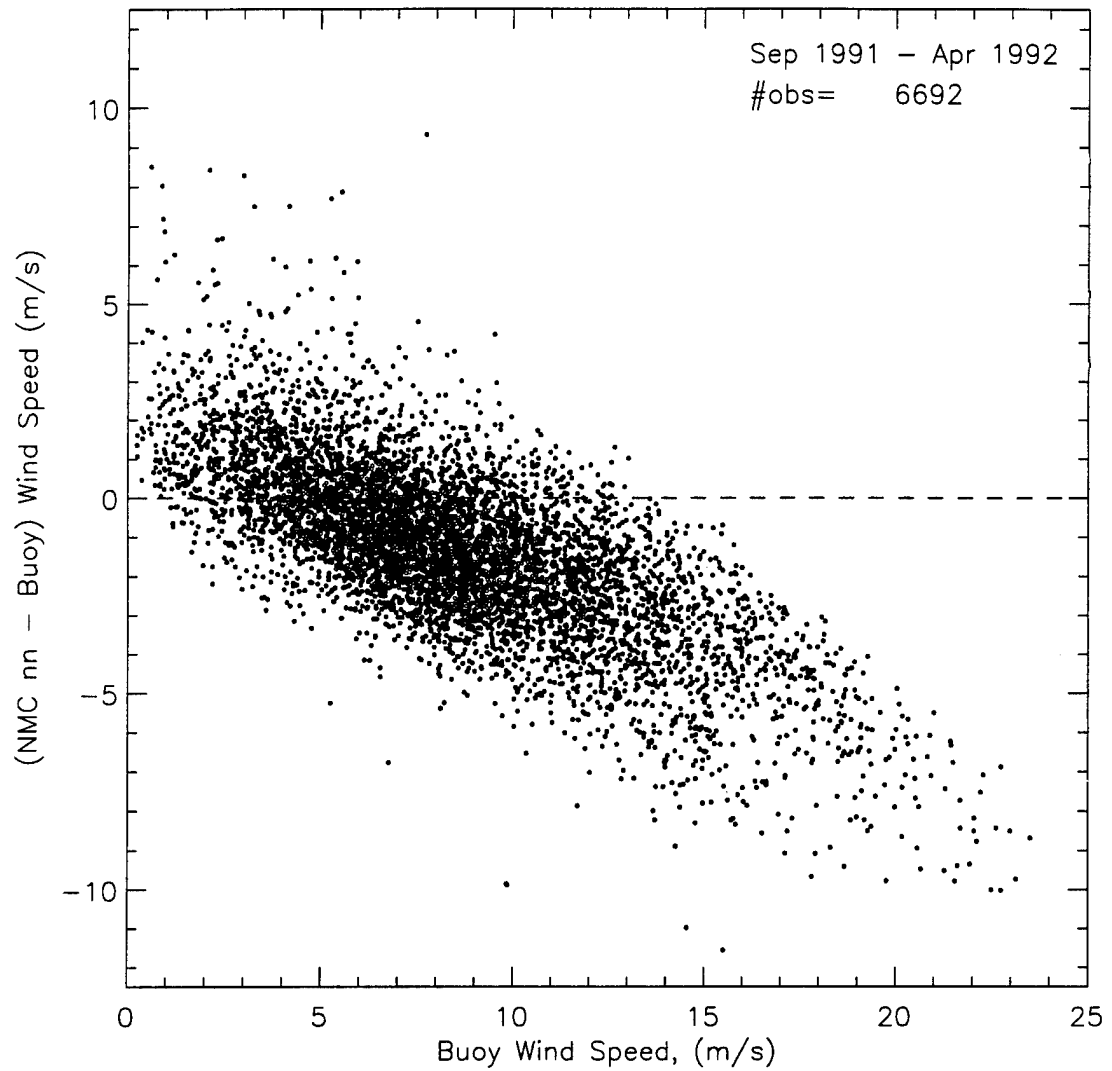
Naval Postgraduate School - Run on 5-Apr-1995

Figure 29: (GSW Nearest Neighbor - Buoy) Wind Speed vs Buoy Wind Speed



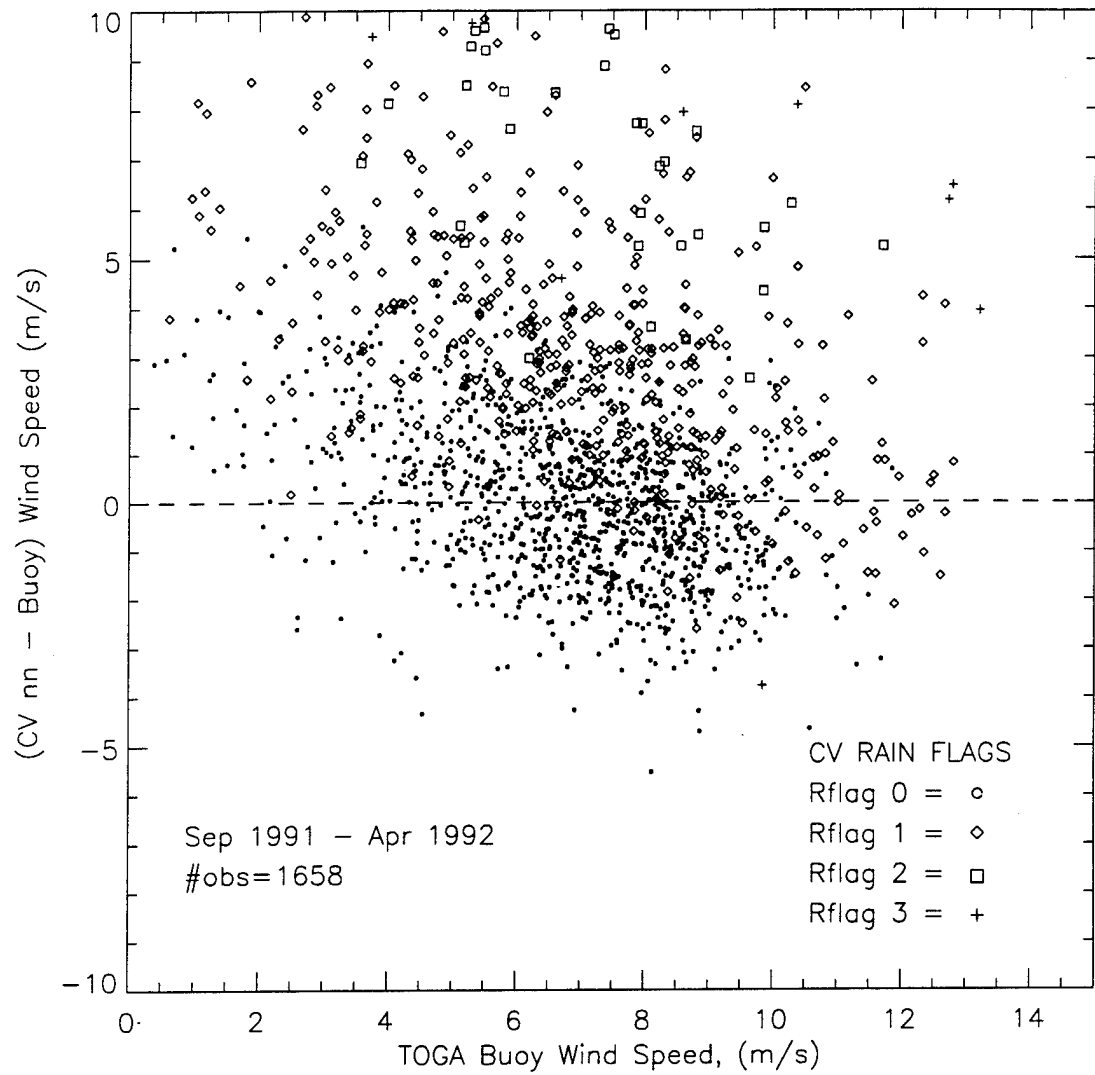
Naval Postgraduate School - Run on 27-Apr-1995

Figure 30: (SBB Nearest Neighbor - Buoy) Wind Speed vs Buoy Wind Speed



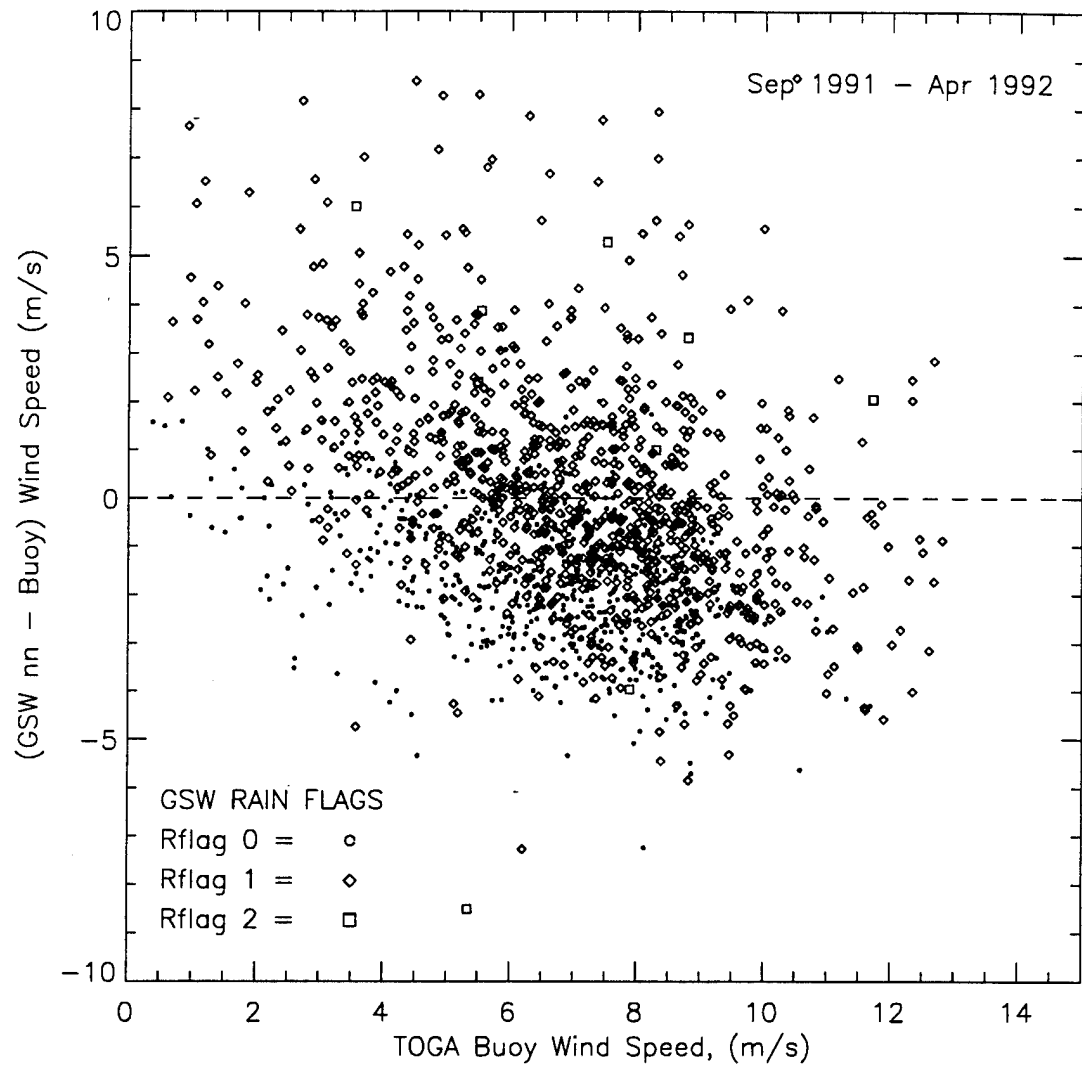
Naval Postgraduate School – Run on 5-Apr-1995

Figure 31: (NMC Nearest Neighbor - Buoy) Wind Speed vs Buoy Wind Speed



Naval Postgraduate School - Run on 11-Mar-1995

Figure 32: (CV Nearest Neighbor - TOGA Buoy) Wind Speed vs TOGA Buoy Wind Speed



Naval Postgraduate School – Run on 4-Apr-1995

Figure 33: (GSW Nearest Neighbor - TOGA Buoy) Wind Speed vs TOGA Buoy Wind Speed

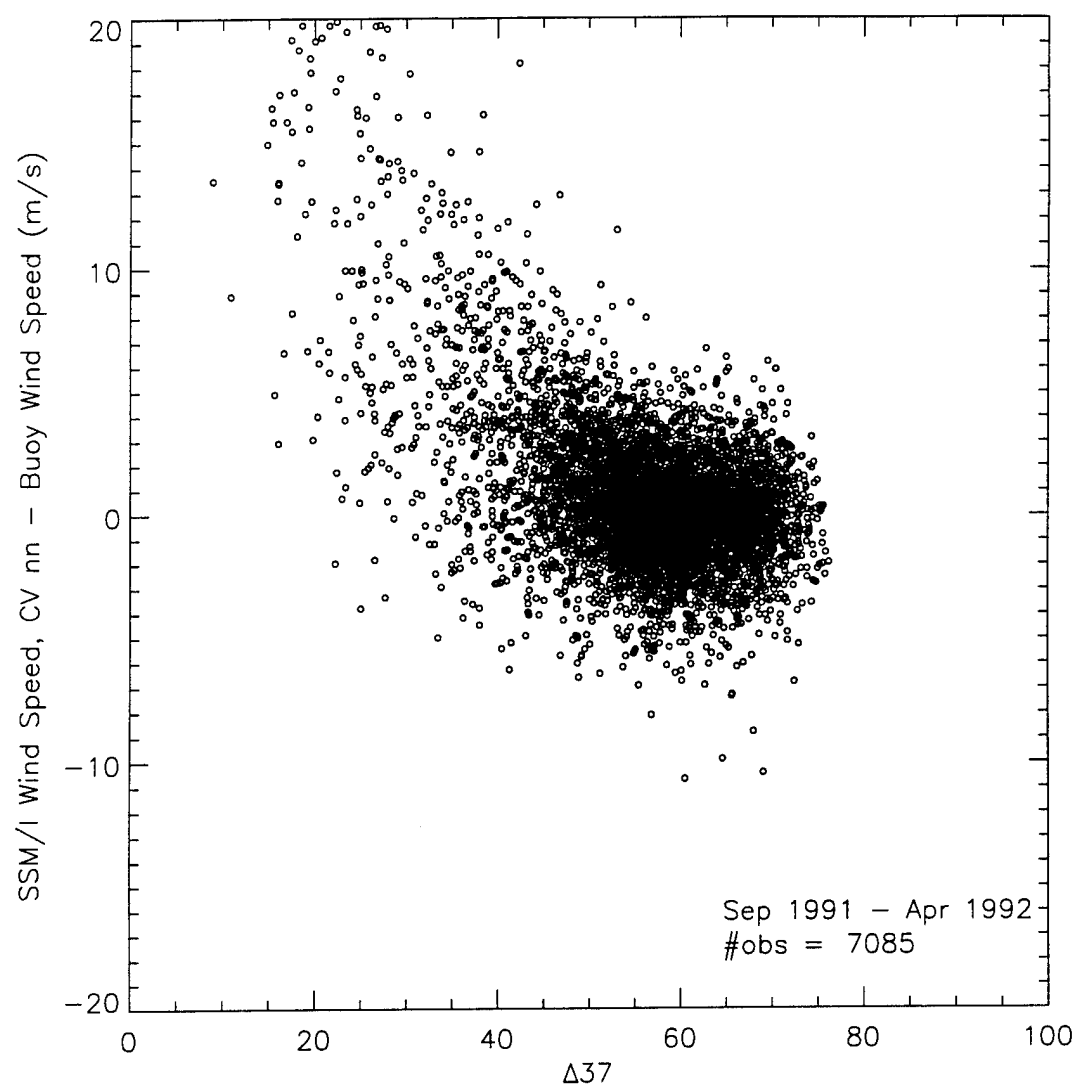
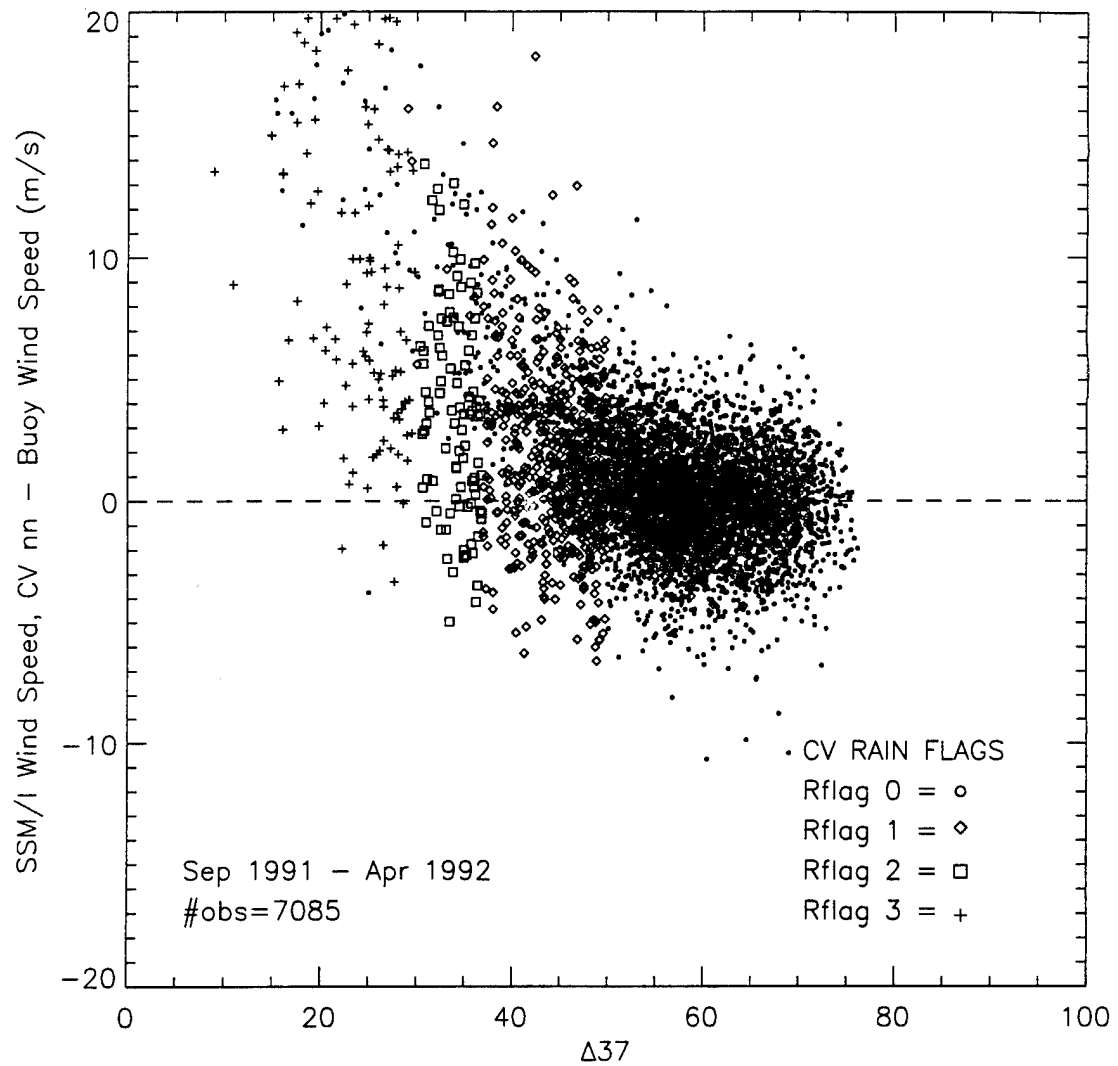


Figure 34: (CV Nearest Neighbor - Buoy) Wind Speed vs T_B 37



Naval Postgraduate School - Run on 26-Apr-1995

Figure 35: (CV Nearest Neighbor - Buoy) Wind Speed vs T_B 37

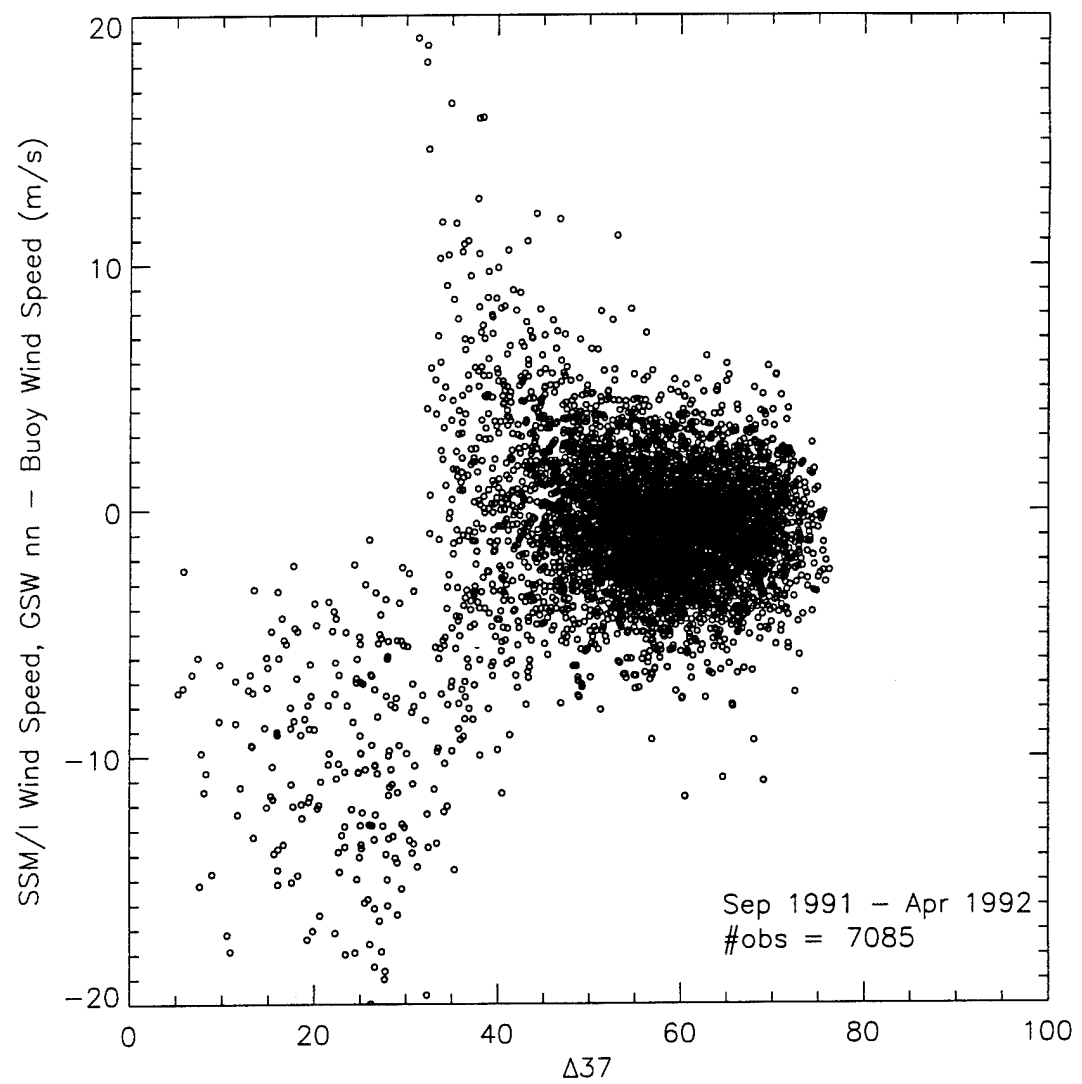
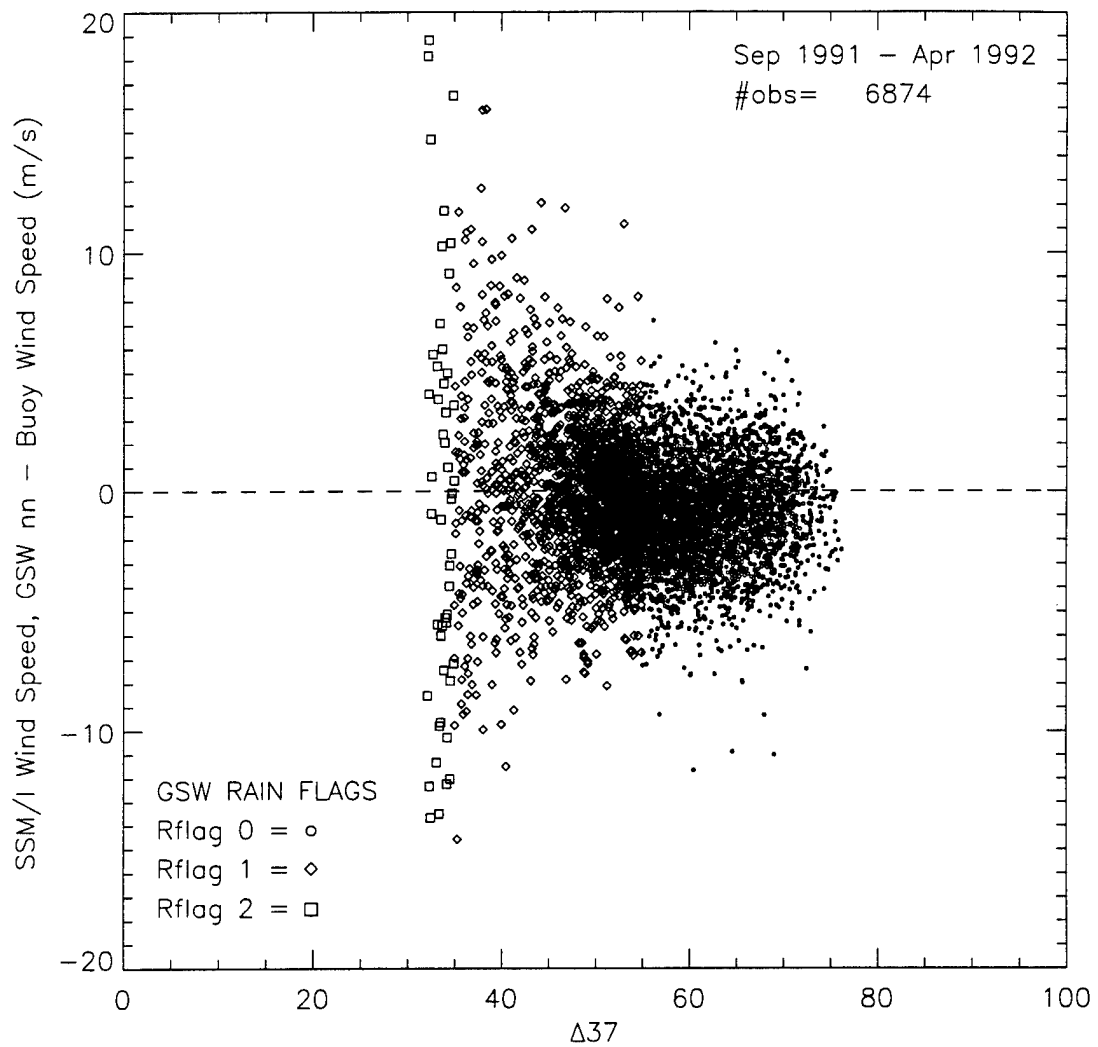


Figure 36: (GSW Nearest Neighbor - Buoy) Wind Speed vs T_B 37



Naval Postgraduate School - Run on 28-Apr-1995

Figure 37: (GSW Nearest Neighbor - Buoy) Wind Speed vs T_B 37

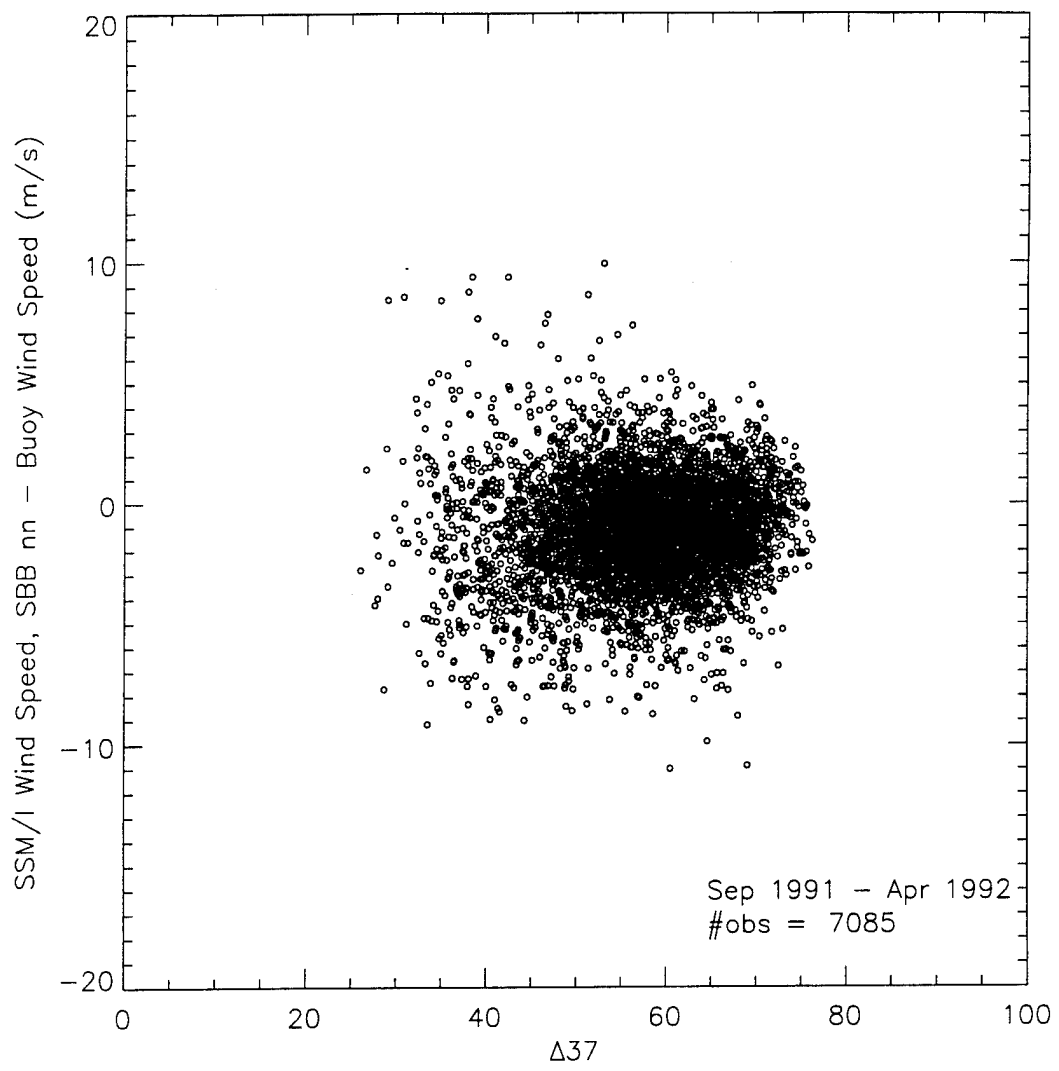
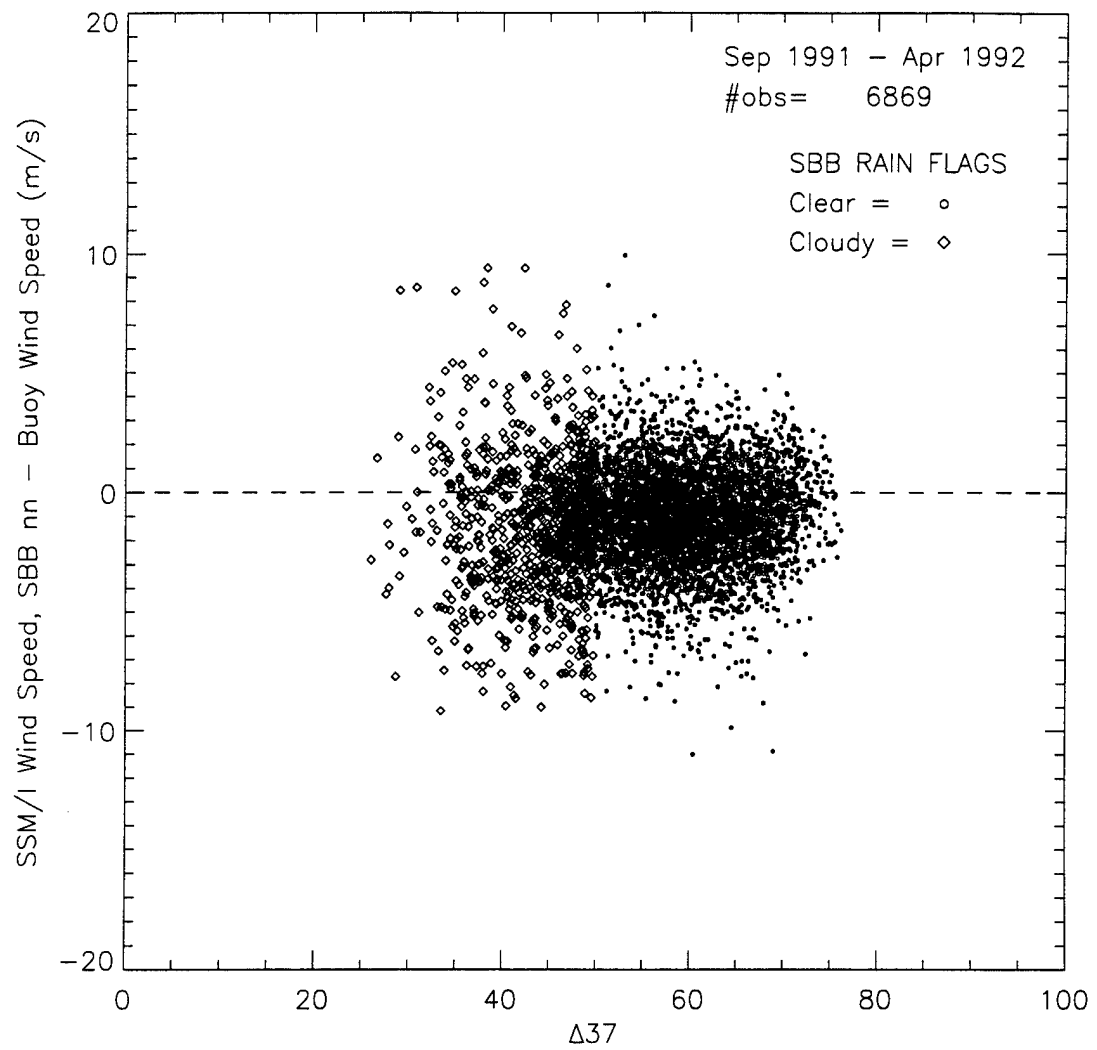


Figure 38: (SSB Nearest Neighbor - Buoy) Wind Speed vs T_B 37



Naval Postgraduate School - Run on 27-Apr-1995

Figure 39: (SBB Nearest Neighbor - Buoy) Wind Speed vs T_B 37

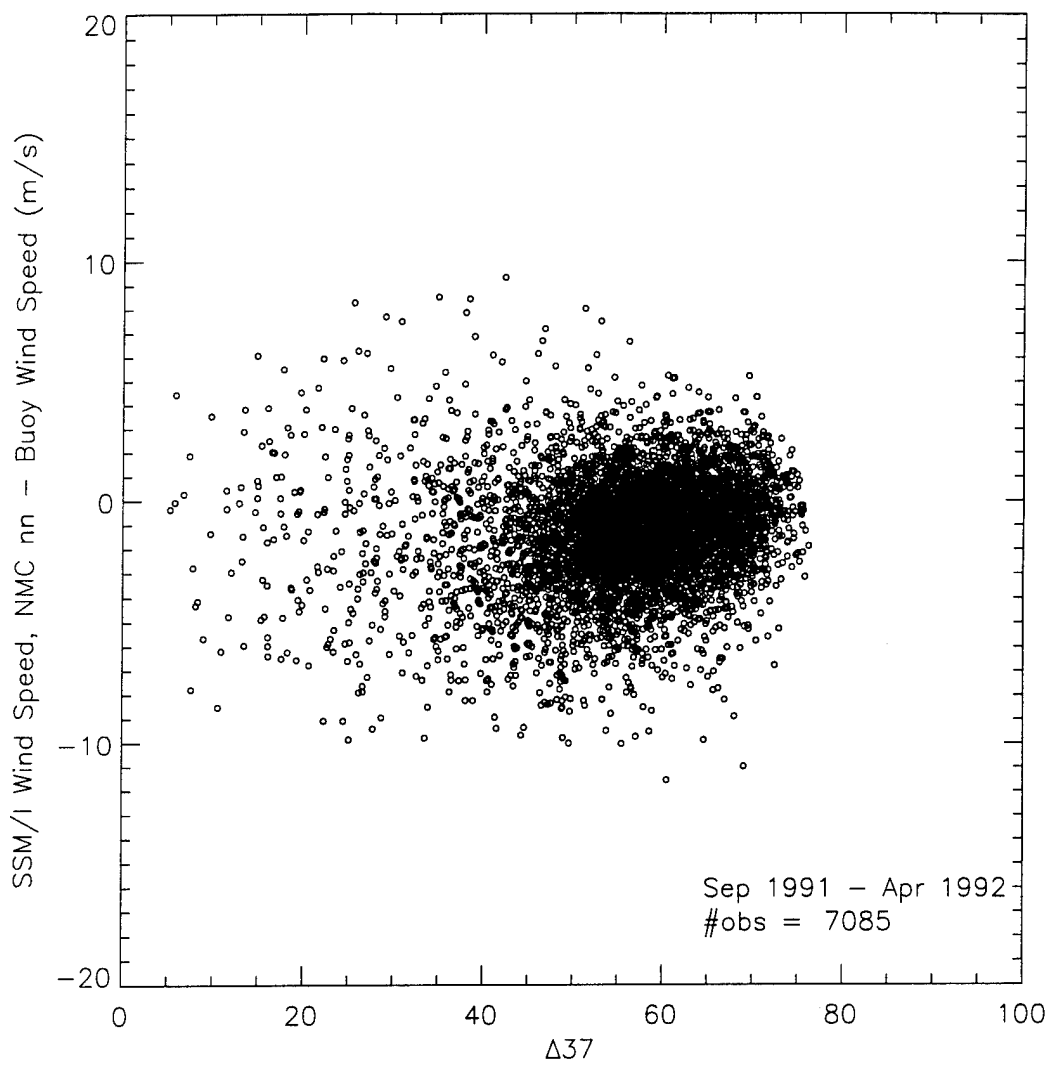
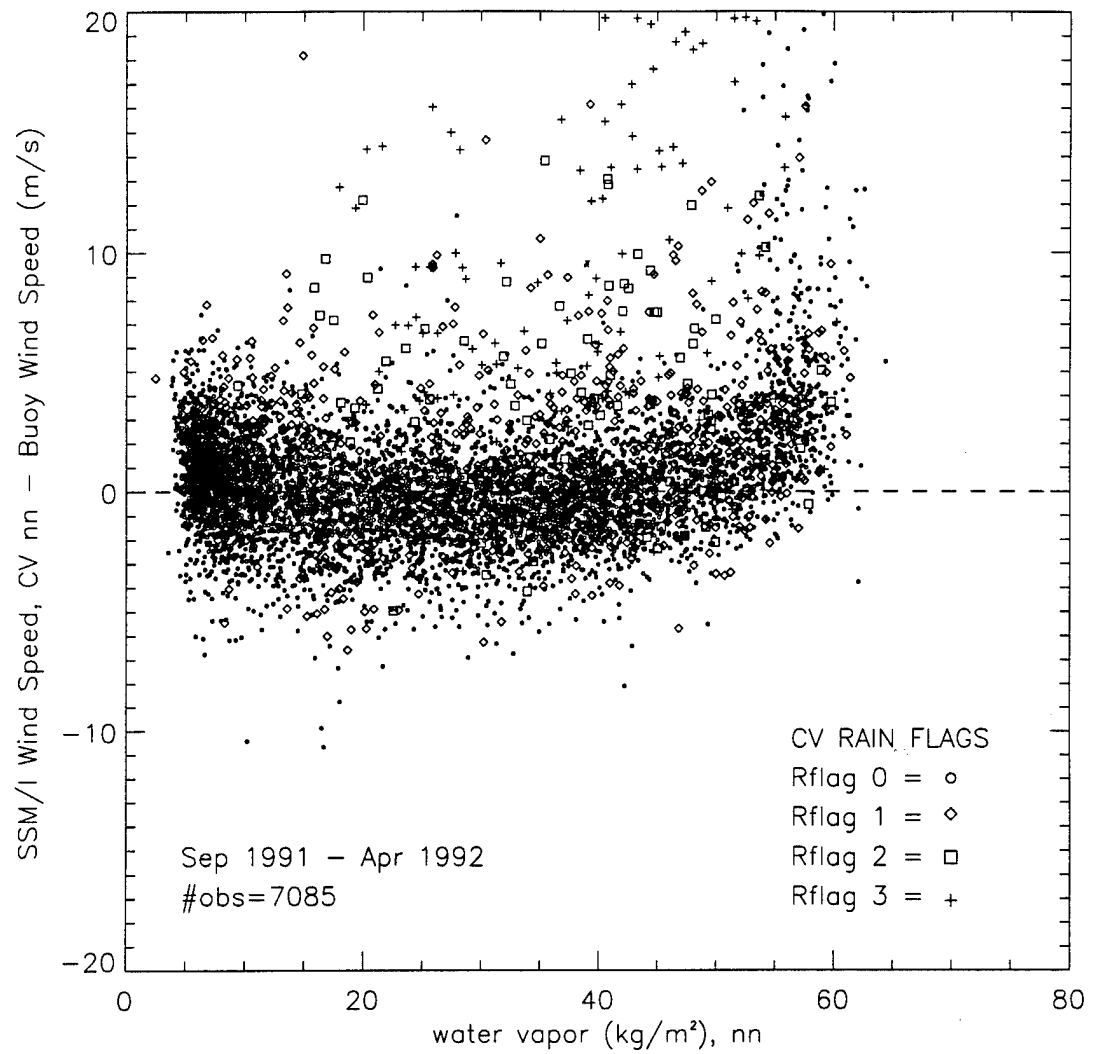


Figure 40: (NMC Nearest Neighbor - Buoy) Wind Speed vs T_B 37



Naval Postgraduate School - Run on 25-Apr-1995

Figure 41: (CV Nearest Neighbor - Buoy) Wind Speed vs Water Vapor

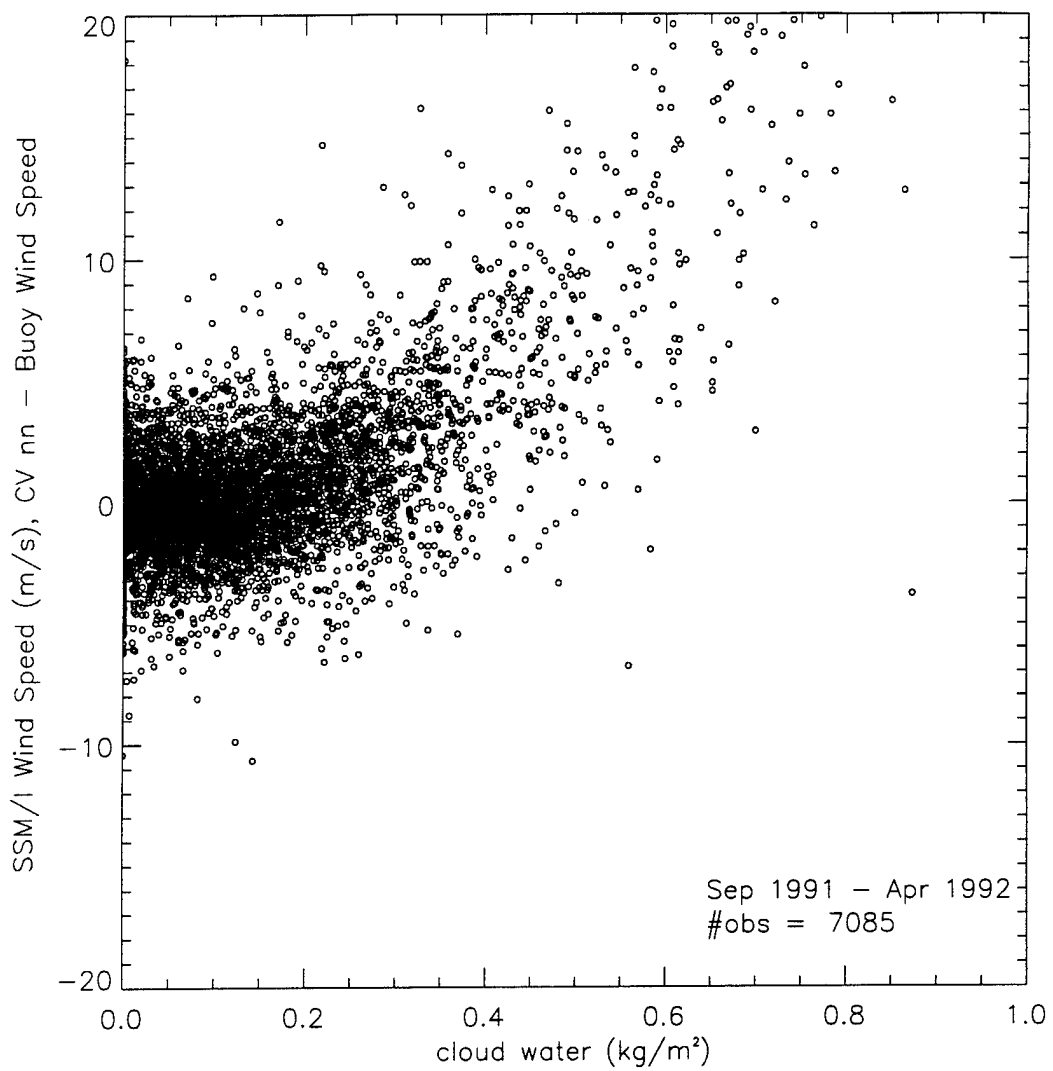
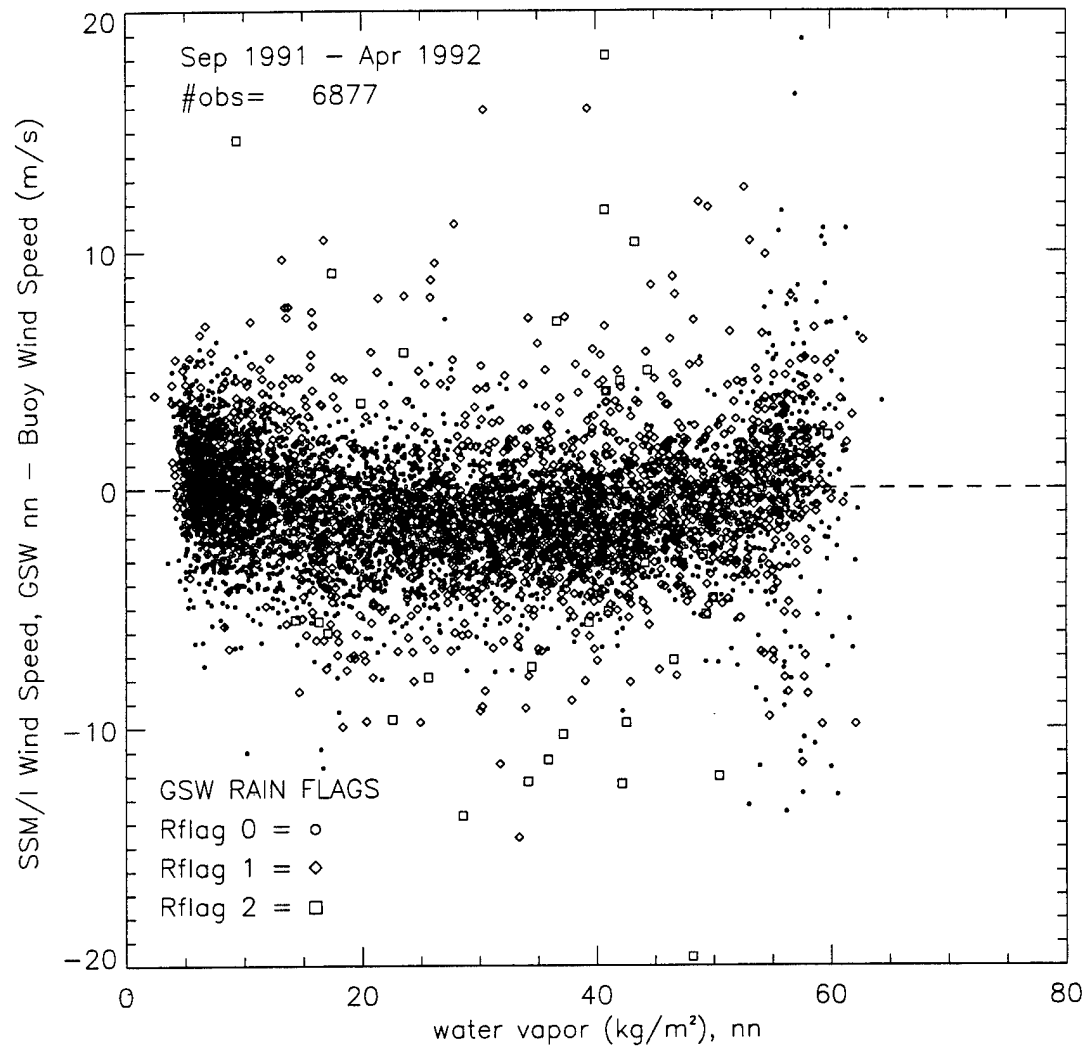


Figure 42: (CV Nearest Neighbor - Buoy) Wind Speed vs Cloud Water



Naval Postgraduate School - Run on 25-Apr-1995

Figure 43: (GSW Nearest Neighbor - Buoy) Wind Speed vs Water Vapor

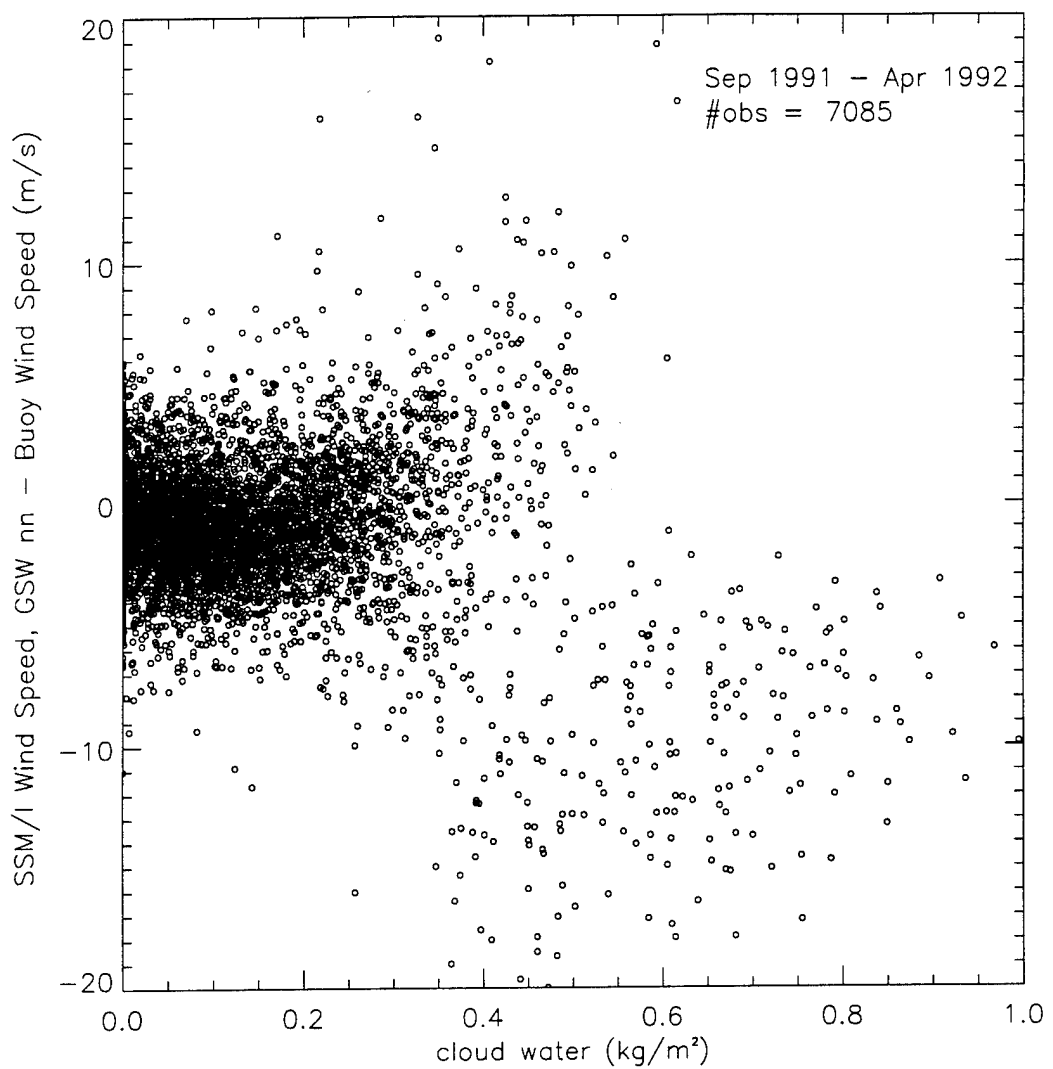
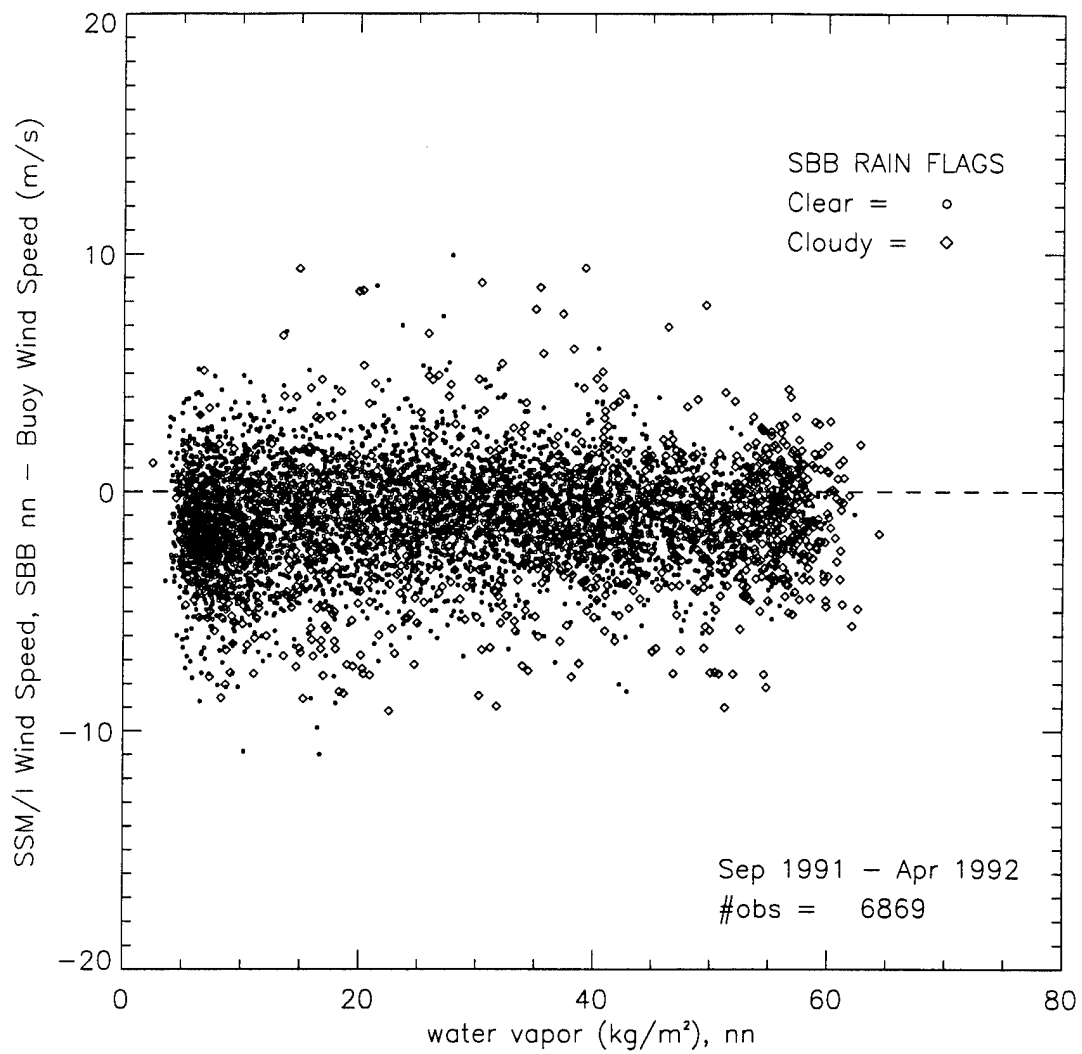


Figure 44: (GSW Nearest Neighbor - Buoy) Wind Speed vs Cloud Water



Naval Postgraduate School - Run on 28-Apr-1995

Figure 45: (SBB Nearest Neighbor - Buoy) Wind Speed vs Water Vapor

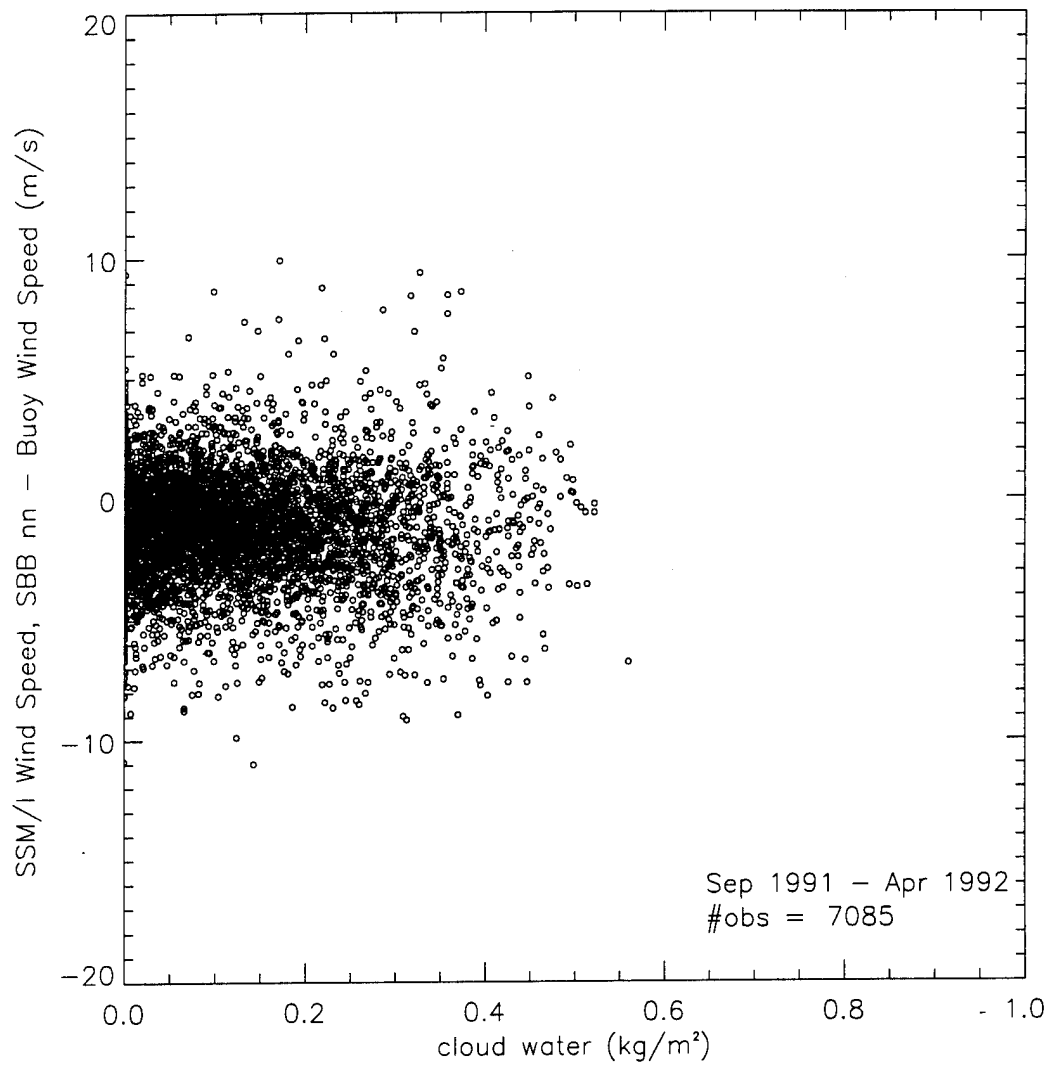
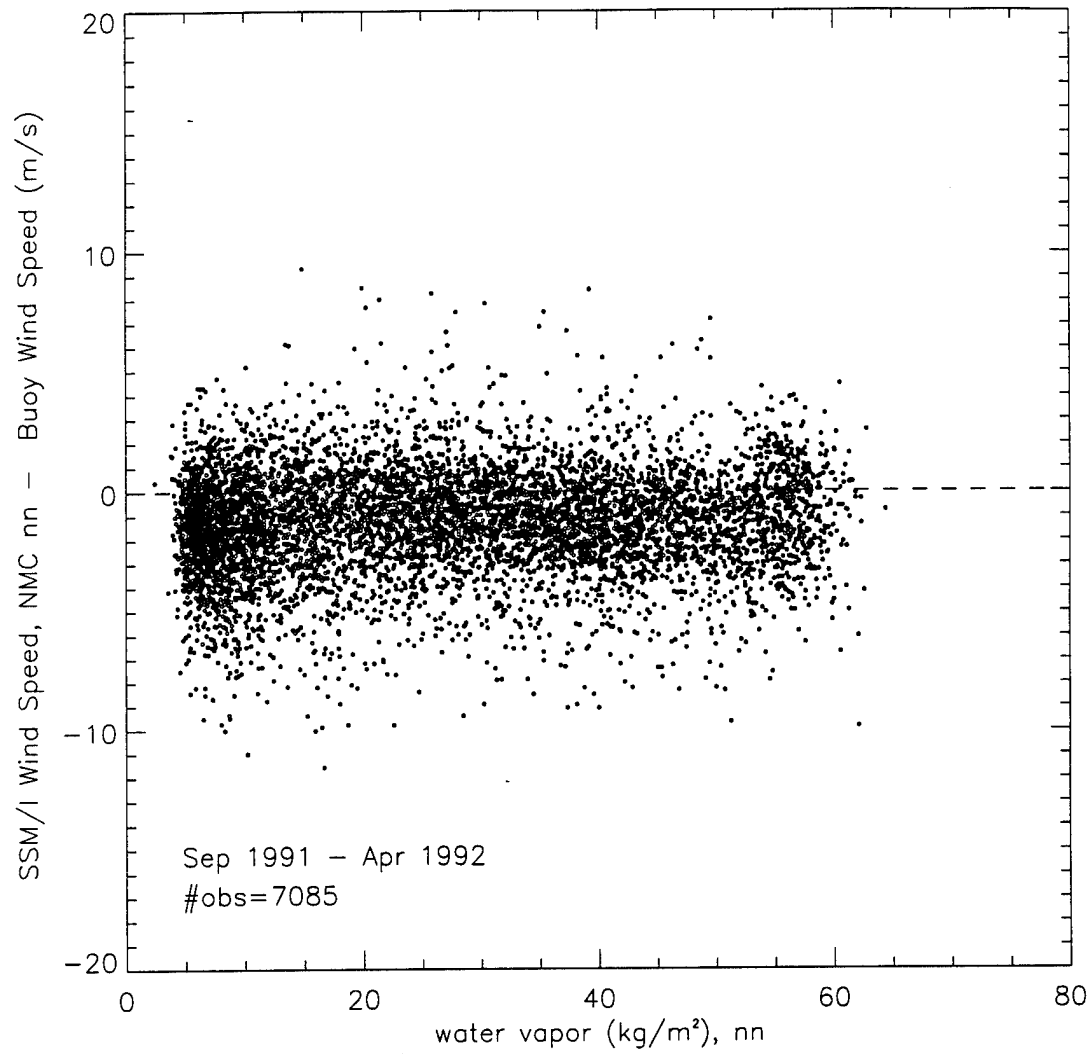


Figure 46: (SSB Nearest Neighbor - Buoy) Wind Speed vs Cloud Water



Naval Postgraduate School - Run on 25-Apr-1995

Figure 47: (NMC Nearest Neighbor - Buoy) Wind Speed vs Water Vapor

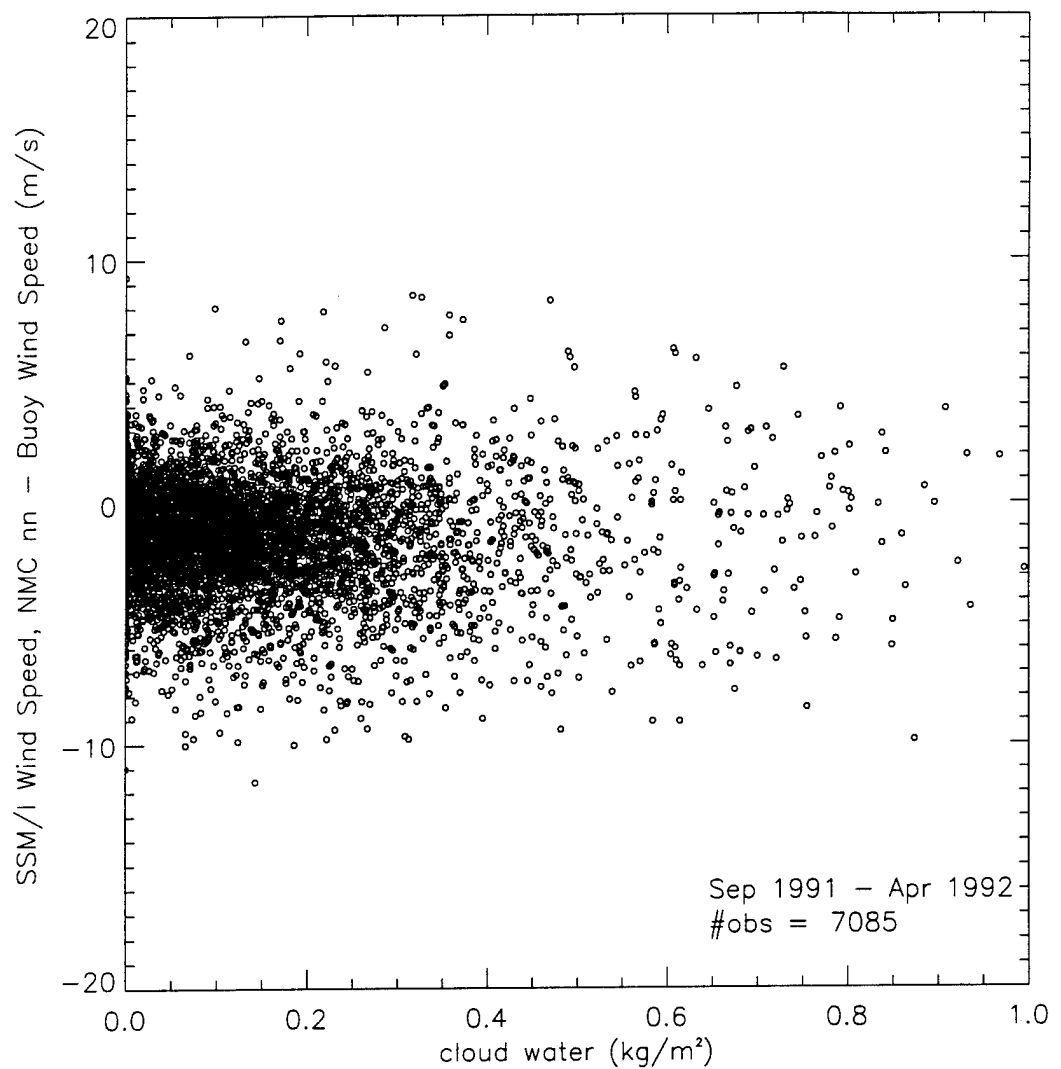


Figure 48: (NMC Nearest Neighbor - Buoy) Wind Speed vs Cloud Water

APPENDIX B: TABLES

TOGA BUOYS USED FOR SSM/I COMPARISONS			
BUOY ID.	LATITUDE	LONGITUDE (E)	ZONE
90001	02.0 N	250.0	Equatorial
90002	02.0 S	250.0	Equatorial
90003	00.0	235.0	Equatorial
90004	02.0 S	235.0	Equatorial
90005	05.0 S	235.0	Equatorial
90006	05.0 N	220.0	Equatorial
90008	05.0 S	220.0	Equatorial
90009	05.0 N	205.0	Equatorial
90010	00.0	205.0	Equatorial
90011	05.0 S	205.0	Equatorial
90012	08.0 N	190.0	Equatorial
90013	05.0 S	190.0	Equatorial
90014	08.0 S	190.0	Equatorial
90015	05.0 N	156.0	Equatorial
90016	02.0 N	156.0	Equatorial
90018	05.0 N	165.0	Equatorial
90019	02.0 N	165.0	Equatorial

Table 1: TOGA Buoys

NDBC BUOYS USED FOR SSM/I COMPARISONS			
BUOY ID.	LATITUDE (N)	LONGITUDE (E)	ZONE
51002	17.2	202.2	Tropics
51004	17.5	207.4	Tropics
51003	19.2	199.2	Tropics
51001	23.4	197.7	Low-latitude transition
42001	25.9	270.3	mid-latitude
42002	26.0	266.5	mid-latitude
42003	26.0	274.1	mid-latitude
41006	29.3	282.6	mid-latitude
41002	32.2	284.7	mid-latitude
44004	38.5	289.4	mid-latitude
46006	40.8	222.4	mid-latitude
44011	41.1	293.4	mid-latitude
46002	42.5	229.6	mid-latitude
44005	42.7	291.7	mid-latitude
46005	46.1	229.0	mid-latitude
46004	50.9	224.1	mid-latitude
46003	51.9	204.1	mid-latitude
46001	56.3	211.7	Arctic
46035	57.0	182.3	Arctic

Table 2: NDBC Buoys

DISTRIBUTION OF DATA POINTS WITHIN RAIN FLAG SUBSETS					
Wind Speed Retrieval Method	Total Data Points	Rain Flag 0 Points (%)	Rain Flag 1 Points (%)	Rain Flag 2 Points (%)	Rain Flag 3 Points (%)
CV TOGA	1658	1106 (67%)	453 (27%)	46 (3%)	53 (3%)
NDBC	5427	4614 (85%)	587 (11%)	94 (2%)	132 (2%)
Global	7085	5720 (80%)	1040 (15%)	140 (2%)	185 (3%)
GSW TOGA	1658	638 (38%)	944 (57%)	16 (1%)	N/A
NDBC	5427	3852 (71%)	1384 (26%)	43 (1%)	N/A
Global	7085	4490 (63%)	2328 (33%)	59 (1%)	N/A
SBB TOGA	1658	1166 (70%)	408 (25%)	84** (5%)	N/A
NDBC	5427	4620 (85%)	675 (12%)	132** (2%)	N/A
Global	7085	5786 (82%)	1083 (15%)	216** (3%)	N/A
NMC TOGA	1658	1106* (67%)	N/A	N/A	N/A
NDBC	5427	4614* (85%)	N/A	N/A	N/A
Global	7085	5720* (80%)	N/A	N/A	N/A

Table 3: Rain Flag Data

* Filtered through CV rain flag 0 criteria

** Not Employed in Study

GLOBAL WIND SPEED RETRIEVAL PERFORMANCE [CLEAR DAY (RAIN FLAG 0) DATA]						
	CV (nn)	CV (avg)	CV (wavg)	GSW (nn)	GSW (avg)	GSW (wavg)
SLOPE	0.843	0.822	0.828	0.877	0.856	0.862
BIAS	1.246	1.499	1.434	0.070	0.300	0.232
COR	0.855	0.866	0.869	0.846	0.862	0.864
SD	1.942	1.837	1.820	1.973	1.824	1.816
	SBB	SBB	SBB	NMC	NMC	NMC
SLOPE	0.697	0.677	0.683	0.630	0.615	0.619
BIAS	1.388	1.577	1.517	1.815	1.962	1.922
COR	0.862	0.884	0.885	0.864	0.884	0.885
SD	1.851	1.751	1.738	1.891	1.827	1.819

Table 4: Global Wind Speed Retrieval Performance

TOGA WIND SPEED RETRIEVAL PERFORMANCE [CLEAR DAY (RAIN FLAG 0) DATA]						
	CV (nn)	CV (avg)	CV (wavg)	GSW (nn)	GSW (avg)	GSW (wavg)
SLOPE	0.641	0.600	0.614	0.707	0.685	0.695
BIAS	2.416	2.775	2.664	0.252	0.529	0.444
COR	0.649	0.688	0.697	0.729	0.800	0.801
SD	1.628	1.464	1.449	1.394	1.154	1.153
	SBB	SBB	SBB	NMC	NMC	NMC
SLOPE	0.737	0.701	0.717	0.584	0.568	0.574
BIAS	0.698	0.990	0.872	1.763	1.881	1.838
COR	0.762	0.804	0.808	0.751	0.802	0.803
SD	1.366	1.205	1.196	1.295	1.184	1.180

Table 5: Wind Speed Retrieval Performance (TOGA Buoys)

NDBC WIND SPEED RETRIEVAL PERFORMANCE [CLEAR DAY (RAIN FLAG 0) DATA]						
	CV (nn)	CV (avg)	CV (wavg)	GSW (nn)	GSW (avg)	GSW (wavg)
SLOPE	0.850	0.829	0.835	0.869	0.849	0.855
BIAS	1.235	1.491	1.426	0.287	0.503	0.436
COR	0.862	0.872	0.874	0.850	0.864	0.866
SD	2.010	1.915	1.898	2.022	1.884	1.874
	SBB	SBB	SBB	NMC	NMC	NMC
SLOPE	0.682	0.662	0.668	0.623	0.607	0.612
BIAS	1.616	1.796	1.737	1.957	2.118	2.074
COR	0.866	0.887	0.888	0.867	0.886	0.850
SD	1.954	1.863	1.849	2.006	1.950	1.940

Table 6: Wind Speed Retrieval Performance (NDBC Buoys)

LIST OF REFERENCES

Dawson, M.S. and A.K Fung, "Neural Networks and the applications to parameter retrieval and classification to parameter retrieval and classification," *IEEE Geoscience and Remote Sensing Society News Letter*, pp. 6-14, 1993.

Fretag, H.P., M.J. McPhaden, and A.J. Shepard, "Comparison of equatorial winds measured by cup and propeller anemometers," *Journal of Atmospheric and Oceanic Technology*, vol 6, pp. 327-332, 1989.

Gloresen, P., D.J. Cavalie, T.C. Chang, T.T. Wilheit, W.J. Campell, O.M. Johannessen, K. B. Quizzers, K.F. Kunzi, D.B. Ross, D. Staelin, E.P. Windsor, F.T. Barath, P. Gudmansen, E. Langham and R.O. Ramsein, "A summary of results from the first Nimbus and SSMR observations," *Journal of Geophysics Research*, vol. 89, pp. 5335-5344, 1984.

Goodberlet, M.A., C.T. Swift, and J.C. Wilkerson, "Remote sensing of ocean surface winds with special sensor microwave imager," *Journal of Geophysics Research*, vol. 94, no. C10 pp 14, 574-14, 555, October 1989.

Goodberlet, M.A., C.T. Swift, "Improved retrievals from the DMSP wind speed algorithm under adverse weather conditions," *IEEE Transactions on Geoscience and Remote Sensing*, vol. 30, pp. 1076-1077, September 1992.

Grody, N.C., "Remote sensing of the atmosphere from satellites using microwave radiometry," edited by M, A. Jansenn, John Wiley and Sons, Inc., New York, NY, 1993.

Hayes, S.P., L.J. Magnum, J. Picacut, and K. Takeuchi, "TOGA-TAO; A moored array for real time measurements in the tropical Pacific Ocean," *Bulletin of American Meteorological Society*, vol 72, pp. 339-347, 1991.

Hollinger, J.P., "Passive microwave measurements of the sea surface," *IEEE Transactions on Geoscience and Remote Sensing*, vol. 91, pp. 165-169, 1971.

Hollinger, J.P., R. Lo, G. Poe, R. Savage, and J. Pierce, *Special Sensor Microwave Imager User's Guide*, Naval Research Laboratory, Washington, D.C. September 1987.

Jansenn, M.A., *Atmosphere Remote Sensing by Microwave Radiometry*, John Wiley and Sons, Inc., New York, NY, 1993.

Krasnopolksky, V.M., L.C. Breaker, and W.H. Gemmill, "Development of a single all-weather neural network algorithm for estimating ocean surface winds from the special sensor microwave imager," *Technical Note*, National Meteorological Center, Washington, D.C., June 1994.

Lo, R.C., "A comprehensive description of the mission sensor microwave imager (SSM/I) environmental parameter parameter extraction algorithm," *NRL Memo Rep.*, 5199, 1983.

Monaldo, F.M., "Expected differences between buoy and radar altimeter estimates of wind speed and significant wave height and their implications on buoy-altimeter comparisons," *Journal of Geophysics Research*, vol. 93, no. C3, pp. 2285-2302, March 1988.

Schlüssel, P., and H. Lüthardt, 'Surface wind speeds over the North Sea from special sensor microwave imager observations," *Journal of Geophysics Research*, vol 96, no. C3, pp. 4845-4853, March 1991.

Smith, S.D., "Coefficients for sea surface wind speeds, heat flux, and wind profiles as a function of wind speed and temperature," *Journal of Geophysics Research*, vol 93, pp. 15467-15472, 1988.

Stevens, G.L., *Remote Sensing of the Atmosphere: An Introduction*, Oxford University Press, New York, NY, 1994.

Stogryn, A.P., "Radiometric emission from a rough sea surface," *Aerojet General Corporation Report*, no. 3000 R-1, 1972.

Stogryn, A.P., C.T. Butler, and T.J. Bartolac. "Ocean surface wind retrievals from special sensor microwave imager data with neural networks," *Journal of Geophysics Research*, vol. 90, no C1, pp. 981-984, January 1994.

Swift, C.T., "Special Joint Issue on Radio Oceanography," *IEEE Journal of Oceanic Engineering*, vol OE-2, no. 1, pp. 1-4, January 1977.

Swift, C.T., "Passive microwave remote sensing of ocean surface wind speeds in surface waves and fluxes," edited by G.L. Geernaert and W.L. Plant, Kluwer Academic Publishers, Dordrecht, 1990.

Ulaby, F.T., R.T. Moore, and A.K. Flung, *Microwave Remote Sensing Active and Passive*, Vol. 3, Artech House, Norwood, MA, 1986.

Wentz, F.J., "Measurement of oceanic wind vector using satellite microwave radiometers," *IEEE Transactions on Geoscience and Remote Sensing*, vol. 30, no. 5, pp. 960-972, September 1992.

INITIAL DISTRIBUTION LIST

	No. Copies
1. Defense Technical Information Center Cameron Station Alexandria, VA 22304-6145	2
2. Library, Code 52 Naval Postgraduate School Monterey, CA 93943-5101	2
3. Combat Systems Academic Group, Code 33 Naval Postgraduate School Monterey, CA 93943-5000	1
4. Department of Physics Attn: Professor R. C. Olsen, Code PH/OS Naval Postgraduate School Monterey, CA 93943-5000	3
5. FNMOC/Code 73 Attn: Dr. M.C. Colton 7 Grace Hopper Ave, Stop 1 Monterey, CA 93943	2
6. NRL, Code 7211 Attn: Gene Poe 4555 Overlook Ave Washington, D.C. 20375-5320	1
7. University of Massachusetts Attn: Mark Goodberlet Amherst, MA 01003	1
8. AFGWC, Code DOA Attn: Charles Holiday Offut AFB, NE 68113-500033	1